NEUROTECHNOLOGY

Human brain mapping with multithousand-channel PtNRGrids resolves spatiotemporal dynamics

Youngbin Tchoe¹†, Andrew M. Bourhis¹†, Daniel R. Cleary^{1,2}†, Brittany Stedelin³, Jihwan Lee¹, Karen J. Tonsfeldt^{1,4}, Erik C. Brown³, Dominic A. Siler³, Angelique C. Paulk⁵, Jimmy C. Yang^{5,6}, Hongseok Oh¹, Yun Goo Ro¹, Keundong Lee¹, Samantha M. Russman¹, Mehran Ganji¹, Ian Galton¹, Sharona Ben-Haim^{1,2}, Ahmed M. Raslan³, Shadi A. Dayeh^{1,2,7}*

Electrophysiological devices are critical for mapping eloquent and diseased brain regions and for therapeutic neuromodulation in clinical settings and are extensively used for research in brain-machine interfaces. However, the existing clinical and experimental devices are often limited in either spatial resolution or cortical coverage. Here, we developed scalable manufacturing processes with a dense electrical connection scheme to achieve reconfigurable thin-film, multithousand-channel neurophysiological recording grids using platinum nanorods (PtNRGrids). With PtNRGrids, we have achieved a multithousand-channel array of small (30 μm) contacts with low impedance, providing high spatial and temporal resolution over a large cortical area. We demonstrated that PtNRGrids can resolve submillimeter functional organization of the barrel cortex in anesthetized rats that captured the tissue structure. In the clinical setting, PtNRGrids resolved fine, complex temporal dynamics from the cortical surface in an awake human patient performing grasping tasks. In addition, the PtNRGrids identified the spatial spread and dynamics of epileptic discharges in a patient undergoing epilepsy surgery at 1-mm spatial resolution, including activity induced by direct electrical stimulation. Collectively, these findings demonstrated the power of the PtNRGrids to transform clinical mapping and research with brain-machine interfaces.

Copyright © 2022 The Authors, some rights reserved; exclusive licensee American Association for the Advancement of Science. No claim to original U.S.

INTRODUCTION

Functional mapping with direct electrical stimulation paired with neurophysiological recording is the gold standard for mapping the human brain and delineating the margins between functional and pathological tissue (1-4). Neurophysiological recording with nonpenetrating surface electrocorticography (ECoG) grids has been used for more than six decades to attain reliable clinical information and improve patient outcomes during surgical interventions (3, 4). ECoG grids can have cortical coverage of up to 8 cm by 8 cm and interelectrode pitch as small as 4 mm (2, 5-10). Higher-resolution grids such as the penetrating Utah arrays have less coverage (4 mm by 4 mm) and better pitch (0.4 mm) than ECoG grids but require invasive surgery to be implanted in deep brain areas (1, 11-14). These are the de facto standard for research on chronic neural prostheses for motor control and decoding language, as well as for providing sensory feedback in paraplegic individuals via closed-loop devices (5–10, 12, 15–23). Although great progress has been made using these devices, the next steps in neuroprostheses and neural decoding require higher spatial resolution (24-26) and expanded coverage of the cortex.

¹Integrated Electronics and Biointerfaces Laboratory, Department of Electrical and Computer Engineering, University of California San Diego, La Jolla, CA 92093, USA. ²Department of Neurological Surgery, University of California San Diego, La Jolla, CA 92093, USA. ³Department of Neurological Surgery, Oregon Health and Science University, Portland, OR 97239, USA. ⁴Department of Obstetrics, Gynecology, and Reproductive Science and Medicine, University of California San Diego, La Jolla, CA 92093, USA. ⁵Department of Neurology, Massachusetts General Hospital, Boston, MA 02114, USA. ⁶Department of Neurosurgery, Massachusetts General Hospital, Boston, MA 02114, USA. ⁷Graduate Program of Materials Science and Engineering, University of California San Diego, La Jolla, CA 92093, USA. We used advanced thin-film microfabrication techniques and a biocompatible platinum nanorod (PtNR) (27) microelectrode material to develop large–surface area ECoG grids with both high resolution and broad spatial coverage. Our PtNRGrids are built on thin, conformal parylene C substrates, and the distribution of contacts is reconfigurable for different pitches and area coverage. We used compact one-touch connectors to enable a simple and reliable interface with thousands of channels that is amenable to the constraints of the operating room. Here, we demonstrated the use of these PtNRGrids to isolate submillimeter functional boundaries (FBs) of individual cortical columns in controlled animal experiments and neural mapping from both awake and anesthetized patients undergoing tumor or epileptogenic tissue resection.

RESULTS

Fabrication of multithousand-channel PtNRGrids and connectorization

PtNRGrids were composed of contacts embedded in flexible sheets of 6.6- μ m-thick parylene C, especially designed for recording neural activity on the cortical surface (Fig. 1). The layout, shape, and size of the PtNRGrids were generated with customizable designs by leveraging established microelectromechanical systems fabrication techniques on large 18 cm–by–18 cm glass wafers and a newly developed, biocompatible PtNR (27) microelectrode material. This process produced multiple 17-cm-long and up to 8 cm–by–8 cm large–area coverage electrodes ranging from 1024 to 2048 electrode contacts or channels with high uniformity and yield (Fig. 1). The 30- μ m-wide PtNR contacts were recessed by ~2 μ m below the surface of parylene C to prevent shear forces on PtNRs during implant (Fig. 1B) (27). Between the PtNR contacts and the bond pads, we routed gold traces that were 500 nm thick, 4 μ m wide, 6 μ m apart, more than 10 cm long, and fully encapsulated between two layers of

^{*}Corresponding author. Email: sdayeh@eng.ucsd.edu †These authors contributed equally to this work.

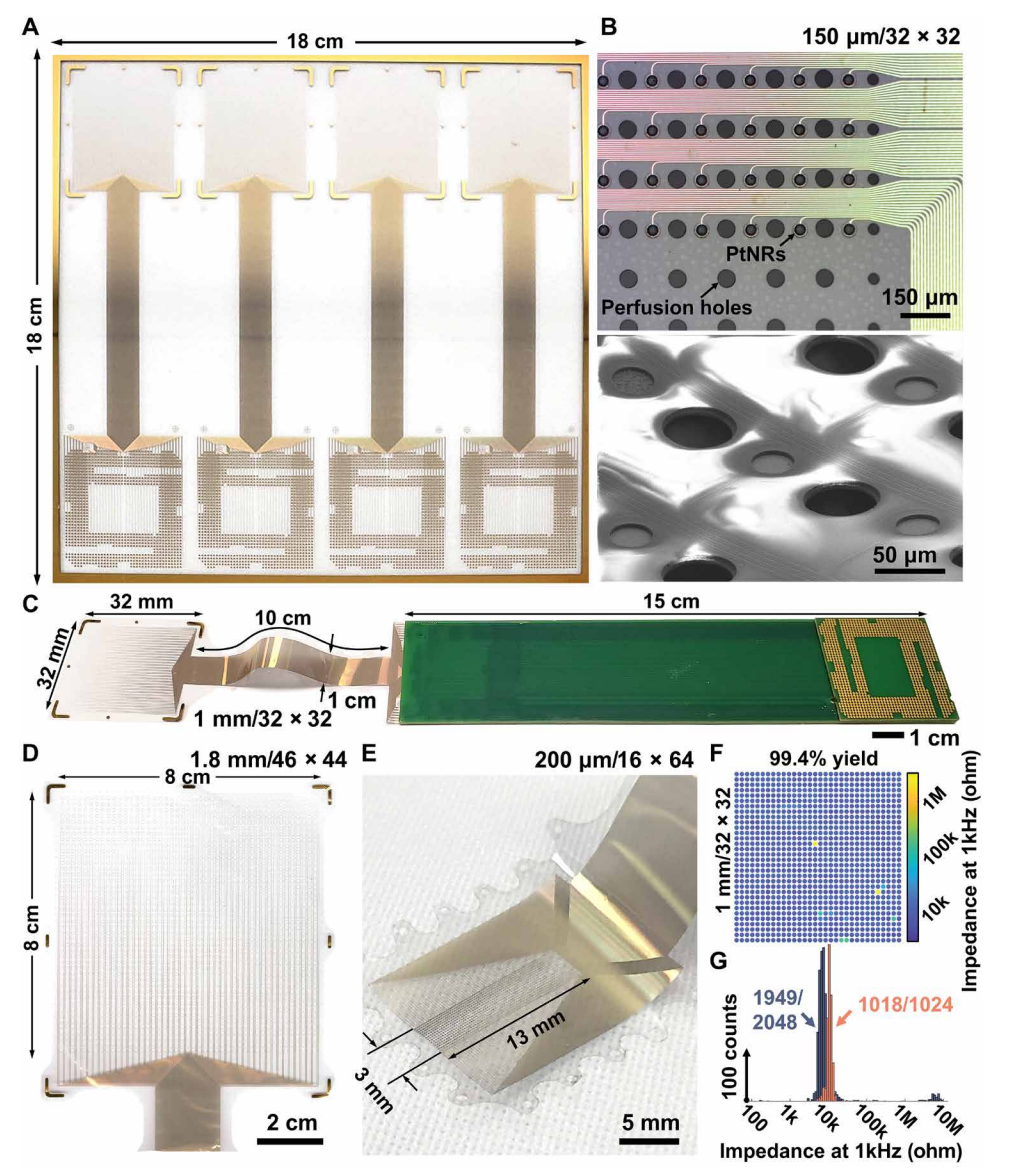


Fig. 1. Multithousand-channel PtNRGrid ECoG arrays. (**A**) Scalable and large-area fabrication of electrode arrays on 18 cm—by–18 cm glass substrates. Microscale features of PtNR contacts, metal leads, and perfusion holes shown by (**B**) optical (top) and electron microscope images (bottom). (**C**) A 1024-channel electrode bonded on the extender PCB that is compatible with CPU LGA sockets. Reconfigurable electrode designs depending on the target placement on the human brain with a sensing area of (**C**) 32 mm by 32 mm (1024 channels), (**D**) 8 cm by 8 cm (2048 channels), and (**E**) 3 mm by 13 mm (1024 channels). (**F**) Spatial mapping and (**G**) histogram of the impedance magnitude at 1 kHz for the 1024- and 2048-channel electrode. Electrodes (1024 and 2048 channels) had 1-kHz impedance magnitude of 11 ± 2 and 8 ± 4 kilohm with a yield of up to 99.4 and 95.2%, respectively.

parylene C (3.5 μ m at the bottom and 3.1 μ m at the top; figs. S1 and S2). We patterned perforation holes in the parylene C throughout the thin grid to perfuse saline and cerebrospinal fluid away from the electrode contacts. Therefore, an intimate interface between the PtNRGrids and the surface of the brain was maintained, and electrochemical shunting between nearby recording contacts was avoided (fig. S3). In addition, the large perfusion holes with diameters of 0.5 mm (Fig. 1C) and 0.9 mm (Fig. 1D) distributed across the grid provided access for probes of a handheld clinical stimulator to directly stimulate any point of the cortex through the grid. We varied

the pitch/coverage of the 30- μ m PtNR contacts from 150 μ m/5 mm by 5 mm for rodent brain mapping (Fig. 1B) to 200 μ m/3 mm by 13 mm (Fig. 1E), 1 mm/32 mm by 32 mm (Fig. 1C), and 1.8 mm/80 mm by 80 mm (Fig. 1D) for human brain mapping. The detailed fabrication process of the PtNRGrids can be found in the Supplementary Materials. The fabrication process of the multithousand-channel PtNRGrids is also compatible with poly(2,3-dihydrothieno-1,4-dioxin)-poly(styrenesulfonate) (PEDOT:PSS) (fig. S4).

A major bottleneck for scaling microelectrode arrays toward hundreds or thousands of channels was the connectorization of electrodes to acquisition circuits. Inspired by solutions used in the microelectronics industry, which can reliably route high-bandwidth connections to thousands of channels (28, 29), we used an off-the-shelf land grid array (LGA), LGA1155 CPU socket, that was originally designed for the Intel's Sandy Bridge computer processors. Manufacturing the grids on largearea substrates ensures sufficient space to bond the PtNRGrids to custom LGA-printed circuit boards (PCBs) that mate with the LGA1155 socket without compromising the large area coverage of PtNRGrids or their long thin-film metal leads (Fig. 1D). An additional extender board was used to further increase the separation between the surgical field and a custom acquisition board (fig. S5) and for improved intraoperative handling procedures. The acquisition board connects to a 1024-channel electrophysiology control system, provided by Intan Technologies LLC (fig. S6). The entire PtNRGrid and connector (Fig. 1C) were compatible with the conventional processes (30) used to sterilize surgical equipment, maintaining contact yields up to 99.4% with a narrow 1-kHz impedance distribution centered at 11 kilohm with an SD of 2 kilohm (Fig. 1, E and F),

achieved with manual bonding of the electrodes to the PCB (fig. S3). The 1-kHz impedance magnitude, averaged over seven different PtNRGrids used in successful human recording experiments, was 10 ± 2 kilohm. The scalable process allowed us to obtain up to 95.2% contact yield with impedances ≤ 100 kilohm even when the total channel count increased to 2048 (Fig. 1F). The simple, one-touch connector methodology enabled our neurosurgical and research team to swiftly and reliably connect thousands of channels to the acquisition board across the boundary between the sterile and non-sterile zones. As a result, sterilization was limited to the disposable

grid and its connector, eliminating the need to sterilize the acquisition electronics. The setup allowed us to record simultaneously from 1024 channels with a sampling rate of 20,000 samples/s, thereby capturing full-broadband neurophysiological activity.

The measured parasitic capacitance between neighboring channels on the PtNRGrids showed 10 million times higher impedance at 1 kHz than the electrochemical impedance, resulting in -60 dB cross-talk as estimated by our measurements and simulations (see figs. S7 to S12). The PtNRGrids also exhibited mechanical stability exceeding the American National Standards Institute/Association

for the Advancement of Medical Instrumentation ANSI/AAMI CI86:2019 recommendations (fig. S13).

PtNRGrids isolate functional cortical columns from the surface of the brain

To test the broadband and high-resolution recording capabilities of the PtNRGrids, we mapped the primary somatosensory cortex of anesthetized rats. The rat cortex has well-defined organization of the somatosensory cortical structures, especially around the barrel cortex, where a series of sensory cortical columns map one to one

with the whiskers. (31, 32) A squareshaped 1024-channel PtNRGrid with 150-µm pitch (Fig. 1B) was implanted to record from the entire right primary somatosensory barrel cortex (Fig. 2). To evoke sensory activity, air puffs were delivered through a microcapillary tube to individually stimulate the contralateralside whiskers (Fig. 2A and fig. S14). We consistently observed large-amplitude raw evoked responses (N = 50) for whisker (E4) stimulation (Fig. 2B). The raw waveforms exhibit localized, highamplitude responses as large as 500 μV with peak responses observed ~30 ms after the onset of the air puff (Fig. 2C). These responses propagated as traveling waves across the cortical surface (fig. S15). The cortical wave propagation was calculated by taking the spatial phase gradients of the beta band (13 to 30 Hz) following the methods described in the works of Rubino et al. (33) and Muller et al. (34). Vector fields express the propagating directions of beta waves, and blue and red colors in the background show amplitudes of beta and highgamma activities (HGAs), respectively (fig. S15). We observed well-differentiated regions for the sources of the beta waves and their destinations, as well as submillimeter-scale spiraling waves. The spatial localization of individual

stimuli is best represented in the gamma band (30 to 190 Hz), as expected, and observed in the root mean square (RMS) power of the measured responses when bandpass filtered (Fig. 2D). The HGA (70 to 190 Hz) is known to be highly correlated to the location and timing of cortical activation with a strong link to spiking activities (35), so we used HGA to map the FBs of the rat barrel cortex (Fig. 2E). We observed clearly distinguishable submillimeter sensory boundaries that classified the responses to different whisker rows and columns, revealing spatially organized barrels with high spatial resolution. The locations of

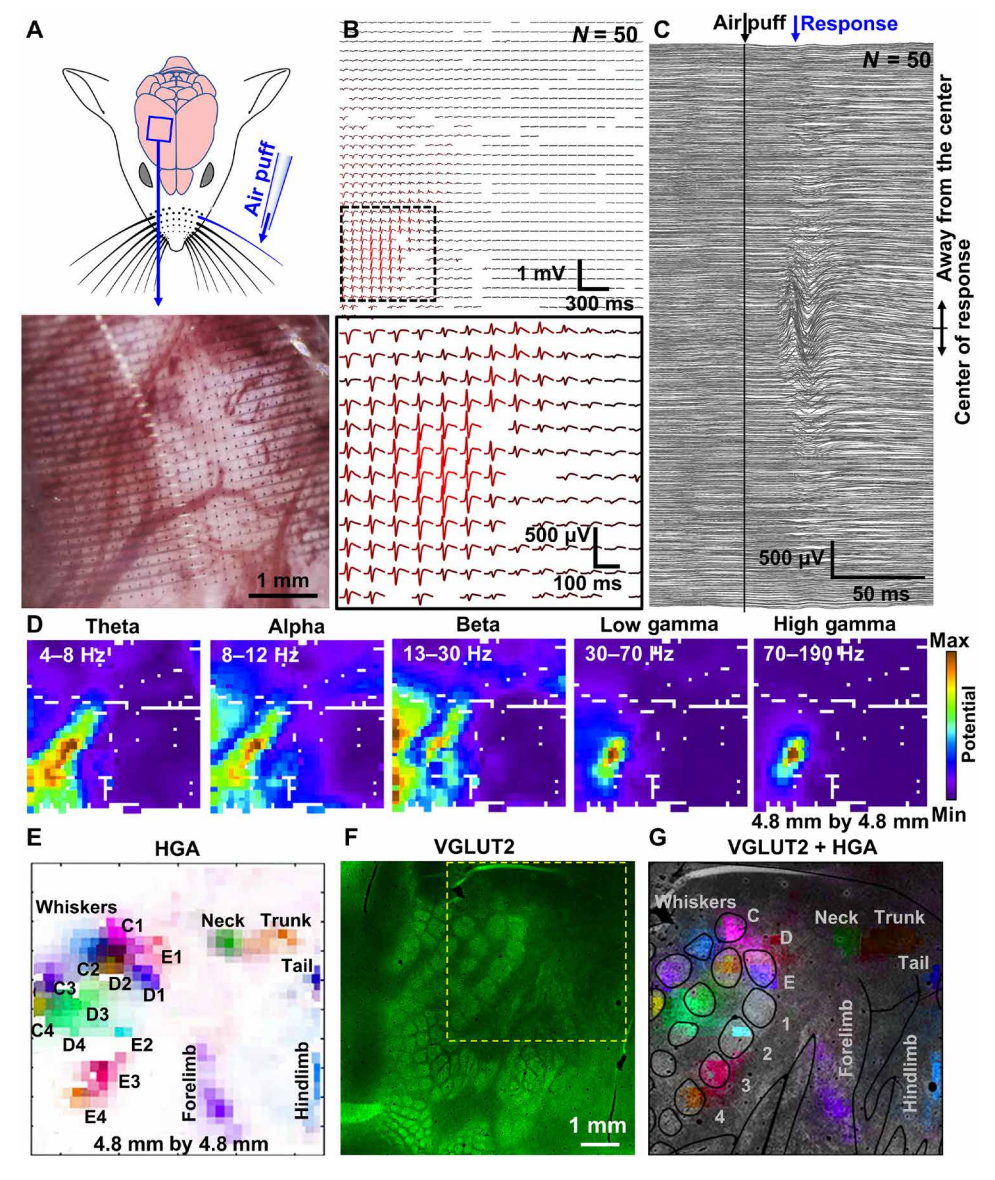


Fig. 2. PtNR multithousand-channel ECoG grids record somatotopic functional cortical columns with sub-millimeter resolution. (**A**) Schematic of the rat brain implanted with 1024 channels, 4.8 mm-by-4.8 mm array, and the air puff stimulation of individual whiskers. The bottom image shows the magnified microscope image of the electrode on the rat barrel cortex. (**B**) E4 whisker stimulation-evoked ECoG recordings (*N* = 50, raw). (**C**) Stimulation-locked response of all channels. (**D**) Spatial mapping of neural wave amplitude filtered at different frequency windows. (**E**) Spatial mapping of high-gamma activity (HGA) recorded by the high-density PtNRGrid. Each label indicates the positions stimulated with air puff. (**F**) VGLUT2 immunostaining of the rat barrel cortex. The electrode implantation location is marked with the yellow dotted box. (**G**) HGA superimposed on top of the histology image.

sensory-responsive areas were also identified by evoking cortical responses with air-puff stimulation of the neck, trunk, and tail and by electrical stimulation of the forepaw and hindpaw (Fig. 2E). The detailed signal processing procedures for HGA mapping (figs. S16 to S19) and the results across different rats (n = 4) could be found in the Supplementary Materials (fig. S20). After completion of functional mapping, the implanted area was marked, and histochemical analyses were used to examine the anatomy under the implant.

The anatomical and FBs were in agreement, as outlined using the vesicular glutamate transporter 2 (VGLUT2), a well-established marker of thalamocortical afferents that compose the homunculus, including the barrels (Fig. 2F) (36). The localized HGA responses to whisker stimuli agree remarkably well with the VGLUT2-labeled positions of the barrels and the homunculus-labeled positions of the forelimb, hindlimb, neck, trunk, and tail (Fig. 2G). Thus, this single-grid-based mapping provides a reliable, real-time high-resolution functional mapping of the rat brain, which contrasts with the traditional serial probing while recording evoked responses (37, 38).

PtNRGrids resolve the curvilinear nature of the human M1-S1 FB

Precise intraoperative localization of the central sulcus, the boundary between primary somatomotor (M1) and somatosensory (S1) cortices, is a necessary approach in several neurosurgical procedures, particularly in the resection of tumors. This anatomical boundary is identified by a functional phase reversal of somatosensory evoked potentials (SSEPs) at the boundary between M1 and S1 (39, 40), an a priori assumed anatomico-functional relationship. Most commonly, these SSEPs, recorded in response to electrical stimulation pulses to the peripheral nerves, are evoked 20 ms after stimulus and demonstrate opposite polarity in their potentials across this boundary. The presence of pathological tissue can induce a shift in the functional organization and location far from its presumed anatomical localization (41, 42) and make traditional sulcal markers harder to discern with low spatial resolution of clinical ECoG grids.

We recorded SSEPs from awake subjects (n = 4) undergoing tumor resection, each with a 1024-channel PtNRGrid with 1-mm spacing (Fig. 1C) placed across the central sulcus near the hand region of the somatomotor sensory cortex while peripheral nerves were stimulated (Fig. 3, A and D, and figs. S21 and S22). The implantation site of the PtNRGrid was marked and identified on a reconstructed model of the patient's brain along with lesion location based on functional magnetic resonance imaging (fMRI) and structural MRI (Fig. 3A). We observed a small stimulus artifact from peripheral nerve stimulation that was followed by high-amplitude SSEPs at 10 to 40 ms (Fig. 3B). These waveforms revealed characteristic positive and negative peaks (43) that reversed phase at the FB denoting the M1-S1 FB (Fig. 3B). The spatially mapped SSEP waveforms captured by the entire PtNRGrid (fig. S23) again clearly demonstrate phase reversal boundary on the cortical surface. Similar SSEP waveforms were recorded with a conventional, dual-column, 2 × 8, 16-channel clinical ECoG grid with 10-mm spacing and 2.3-mm-diameter recording contacts (Fig. 3C and figs. S24 and S25). The maximum interpeak amplitude of SSEPs measured by the PtNRGrid was 214 µV (Fig. 3B), whereas SSEPs measured by the clinical ECoG grid (Fig. 3C) on the same patient only showed 5-µV interpeak amplitude.

The PtNRGrids revealed the precise curvilinear nature of the M1-S1 FB with millimeter-scale resolution at a sampling frequency of 20 kHz. The subject's lesion (Fig. 3A) contributed to the broadening and distorting of the SSEP waveforms on both the PtNRGrids (Fig. 3B) and on the clinical ECoG (Fig. 3C), in agreement with the findings of prior clinical studies (39). In addition, the SSEPs recorded with the PtNRGrid were minimally affected by the presence of underlying surface blood vessels (44): The waveform shapes and amplitudes ("CS" denoting the anatomical central sulcus in Fig. 3B and fig. S26) of the channels on top of the blood vessel did not show any noticeable difference compared to those of the adjacent channels. Although the SSEPs were minimally affected by the blood vessel (fig. S26), it is reported that higher-frequency signals (30 to 70 Hz) could be attenuated by 30 to 40% by the presence of the blood vessel (44).

To construct the two-dimensional maps for the curvilinear FB, we used the conventional potential-based phase reversal technique (Fig. 3E) and a correlation technique that we devised to identify the FB in diseased tissue (Fig. 3F). We calculated the Pearson correlation coefficients of the waveforms between 5 and 50 ms after stimulus for all the working channels with respect to the channel in the middle of the grid. Channels with correlation coefficients above or below 0.5 were separated by a dotted line to depict the M1-S1 FB (Fig. 3F), which agrees well with that deduced directly from potential maps (Fig. 3E). We observed a highly detailed spatial map depicting considerable offset, based on SSEPs (Fig. 3) and HGA (Fig. 4), between the M1-S1 FB and the anatomical central sulcus using the PtNRGrid (FB versus CS in Fig. 3D), consistent with functional reorganization with brain lesions (41, 42). However, it is important to note that these SSEPs are projections of event-related potentials from deeper layers that are often oblique to the plane of the cortical surface. Extension of this FB below the surface must be validated with depth recordings (45). Nevertheless, the M1-S1 FB revealed by the PtNRGrid was concordant with the gold standard clinical mapping using conventional bipolar stimulation and with higher resolution than conventional clinical ECoG grid passive gamma mapping using CortiQ system.

We also recorded SSEPs from the human brain using a 2048-channel PtNRGrid with 1.8-mm pitch (Fig. 1D and figs. S27 to S29). The waveforms (30 to 3000 Hz, N=22) exhibit clear P20-N20 peak responses of ~20 ms after the median nerve stimulation (Fig. 3G). The severe anatomical distortion and the limited time of recording precluded assessing a FB in this return surgery (fig. S30). Nevertheless, the results of Fig. 3G illustrate that the scalable PtNRGrids enable multithousand-channel recordings from the human brain. PEDOT:PSS electrodes (1024 channels) with 1-mm pitch and 100- μ m electrode contact diameter also recorded SSEPs from the human brain with an interpeak amplitude up to 57 μ V (fig. S31).

PtNRGrids reveal large-scale spatiotemporal dynamics of motor and sensory activity in humans

Motivated by the rise of interest in using ECoG grids for brain-machine interfaces (5, 8–10, 21–23), we investigated whether the high spatial and temporal resolution of the PtNRGrid could be used to map sensory- and motor-evoked activities. Following the phase reversal mapping of the functional M1-S1 boundary and with the same PtNRGrid placement on the same participant, we either stimulated individual fingers with vibrotactile stimulators or asked the patient

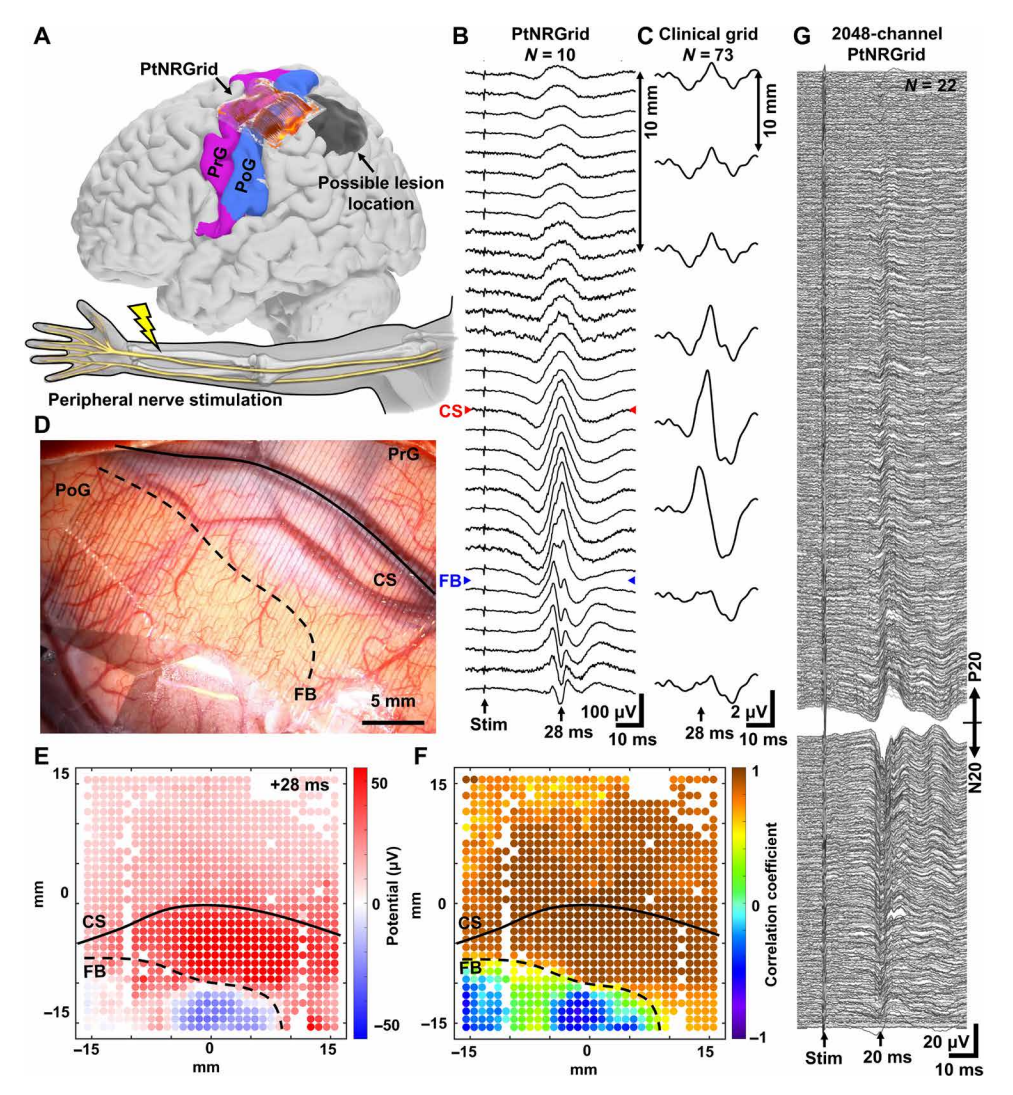


Fig. 3. Mapping the curvilinear nature of the functional sensory/motor regions in the human brain with millimeter resolution. (**A**) Reconstructed model of the patient's brain and the electrode implantation locations. Electrodes were implanted near the hand region, and the peripheral nerve was electrically stimulated. Somatosensory evoked potential (SSEP) waveforms along a line across the central sulcus (CS) and M1-S1 functional boundary (FB) recorded with a (**B**) 32 × 32 PtNRGrid with 1-mm spacing and (**C**) 2 × 8 clinical grid with 10-mm spacing. (**D**) Implantation picture of the electrodes near the hand region. (**E**) A 1024-channel potential mapping of the stimulation-evoked waves 28 ms after the stimulation [as opposed to 20 ms due to distortion from brain lesion as shown in (B) and (C)]. (**F**) Correlation coefficient mapping with respect to the waveforms measured with respect to the channel in the center of the grid. (**G**) Human brain SSEPs from a 2048-channel PtNRGrid. Channels are sorted according to the peak potential amplitude and polarity at 20 ms after the stimulation, and channels with high contact impedance were excluded from the plot. PrG: precentral gyrus, PoG: postcentral gyrus.

to perform specific hand movements (Fig. 4A and fig. S32). After individual fingertip stimulation, we observed a clear enhancement in HGA as large as 3 σ from baseline (Fig. 4B), the largest of which was localized only in the primary somatosensory cortex (Fig. 4B). Vibrotactile stimulation of each fingertip evoked spatially distinctive HGA patterns, with some channels tuning to all fingertips with varying magnitudes. After superimposing HGA on an optical image of the implanted PtNRGrid, we could observe the fine spatial distribution of the neural correlates of vibrotactile stimulation and compare this with the M1-S1 boundary and the cortical anatomy using phase reversal (Fig. 4C).

We next demonstrated the high spatiotemporal capabilities of the PtNRGrids during a hand grasping task (Fig. 4, D to L). As with the vibrotactile stimulation, we observed highly localized HGA on the PtNRGrid during the motion (Fig. 4G), near completion of motion (Fig. 4H), and for 100 ms after completion of motion (Fig. 4I) (see also movie S1). Furthermore, coordination between the S1 and M1 cortices during the grasping task could be seen at high resolution via the PtNRGrid. In a snapshot of the dynamics through time along a single line of electrodes cut across a corner of the grid (highlighted by the yellow rectangle in Fig. 4I), we illustrate the spatial dynamics for the selected 16 channels across the M1-S1 boundary for the HG (Fig. 4E) and beta (Fig. 4F) bands. These band-specific (spectrotemporal) dynamics showed remarkable correlation with the hand movement captured by time-locked flex sensors on the subject's hand (Fig. 4D). Distinctive HGA in the M1 cortex was observed during motor initiation, was seen in both M1 and S1 cortices during the hand closure onset, and, lastly, lingered only within the S1 cortex when the motion was complete. High-amplitude beta wave in the M1 cortex was observed before the motion, during the planning stage, attenuated during execution of the motion, and increased once again after the motion was completed (Fig. 4, D to F). Similar behavior was observed under trials of repeated hand grabbing motion (see fig. S33). These observations of alternating amplitude in HGA and beta activity before, during, and after the motion agree with prior observations (46-48).

Last, we showed that with the large channel count of the PtNRGrid, we could construct maps of brain wave propagation at high spatial resolution within a physiologically relevant cortical cover-

age (Fig. 4, J to L, and fig. S34). During the hand grasping task, we calculated the spatial gradient of the phase of the beta waves (13 to 30 Hz) (33, 34) recorded by our PtNRGrids to infer propagation direction (Fig. 4, J to L, and movies S2 and S3). We further overlaid streamlines originating from selected regions in the S1 and M1 cortices on top of the vector fields for a visual aid of the long-range propagation directions. We found clear propagation dynamics across the M1-S1 FB, which correlated with the hand grabbing motion. In the preparation stage of the motion, we observed noticeable long-range beta waves propagating from the S1 cortex to M1 cortex (Fig. 4J). During the motion, the beta waves were suppressed

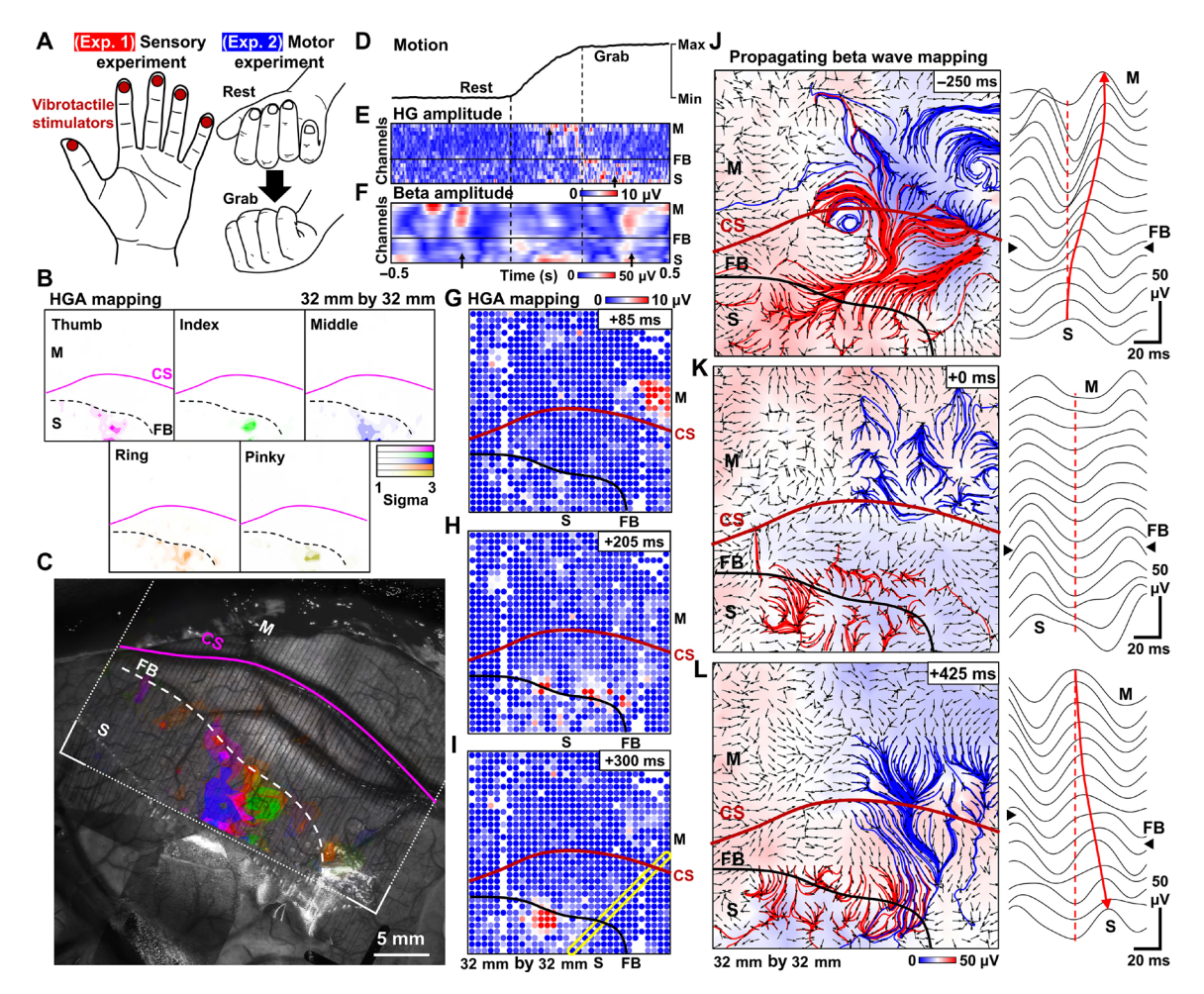


Fig. 4. Functional mapping with millimeter resolution: PtNRGrid records detailed sensory and motor spatiotemporal dynamics in humans. (A) Schematics of the sensory and motor experiments. For sensory experiment, individual fingers were stimulated by vibrotactile stimulation in sequence with 1-s stimulation at 2-s intervals. For the motor experiment, the patient was asked to perform a grasping task. (B) Spatial mapping of HGA of individual fingers in response to vibrotactile stimulations. (C) Overlay plot of HGA sensory responses for individual fingers superimposed on top of a photo of the surface of the patient's brain. (D) Motion of the hand recorded with the bending sensor. The amplitude of (E) HGA and (F) beta activity of channels selected along the yellow diagonal rectangle in (I) plotted over a 1-s time window during the motion. Spatial mapping of HGA over three different time points during the hand grabbing motion. (G) Initially localized HGA appears on the motor region, (H) then both the motor and sensory regions show HGA, and, (I) eventually, the HGA only appears on the sensory region. Propagating beta waves and waveforms across the CS in the (J) planning stage of the motion, (K) during the motion, and (L) after the completion of motion. The red and blue streamlines originate from the sensory and motor cortices, respectively. The background color represents the amplitude of the beta wave potential, and the arrowheads indicates the propagating direction of the beta waves. Right plots are raw waveforms for the yellow box in (I) around the timestamps of (J) to (L).

and exhibited lack of coherence in the vector fields (Fig. 4K). After the motion was complete, the propagating direction reversed, as represented by the streamlines (Fig. 4L and atop a reconstructed brain model in movie S4). Similar propagating wave dynamics were reproduced in multiple hand grabbing motions (fig. S35). Higher wave propagation speed was observed between the electrodes placed across the central sulcus, which is an artifact, considering that the adjacent electrodes placed across the sulcus are separated by up to a few centimeters on an unfolded cortical surface (fig. S36). Because slightly different frequency windows of 9 to 18 Hz (34) and 10 to 45 Hz (33) were selected in prior works for the propagating beta wave analysis, we repeated the propagating beta wave analysis at three different frequency windows: 13 to 30, 9 to 18, and 10 to 45 Hz (figs. S37 and S38). All three beta wave frequency windows showed that the beta wave amplitude (fig. S37) and propagating wave directions (fig. S38) before, during, and after the hand movement were

consistent with each other. By detecting the propagation dynamics of beta waves with high spatial resolution at physiologically relevant coverage using our PtNRGrids, we have enhanced functional mapping by revealing large-scale brain activity across frequency bands.

PtNRGrids record pathological wave dynamics

Last, we determined the utility of PtNRGrids for high-resolution intraoperative neuromonitoring to detect ictal onset zones and patterns of seizure spread. PtNRGrids (1-mm spacing, 32 × 32 contacts, and 0.5-mm-diameter perfusion holes; Fig. 1C) were placed over the cortex in a patient with intractable epilepsy related to a left anterior temporal lobe cavernoma who was elected for surgical resection (Fig. 5A). Using PtNRGrids allowed passive recordings of local field potential and active electrical stimulation through the perfusion holes (uniformly distributed at 0.5-mm diameter and 1-mm spaced; Fig. 5A) using a standard handheld clinical stimulator

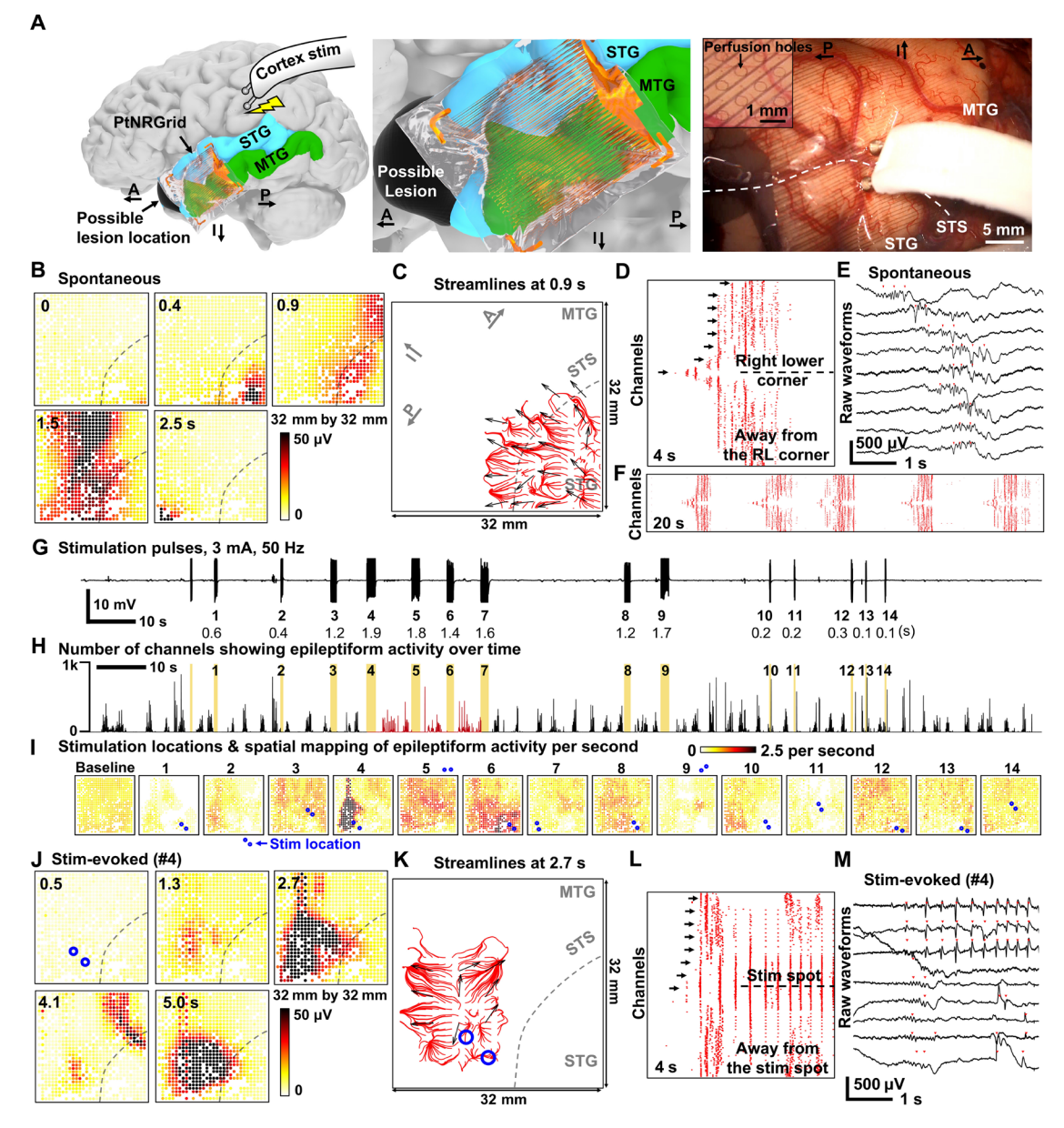


Fig. 5. Pathological mapping with millimeter resolution: PtNRGrids reveal detailed spatiotemporal dynamics of spontaneous and stimulated epileptiform discharges from a patient with epilepsy. (A) Left: Reconstructed model of electrode placement on the temporal lobe of the patient's brain and the schematics of charge-balanced biphasic direct current stimulation with the bipolar (Ojemann) probe. Middle: Magnified model near the electrode. Right: Photo showing the cortical tissues directly being stimulated through the electrode. Inset is a magnified image showing the 0.5-mm-diameter perfusion holes that are distributed at a 1-mm pitch on the electrode, allowing direct current stimulation at any point on the grid. Positions of the superior temporal sulcus (STS), superior temporal gyrus (STG), and middle temporal gyrus (MTG) are marked on the photo. Anatomical orientation arrows indicate anterior (A), posterior (P), and inferior (I). (B to F) Spontaneous epileptiform discharges. (B) Spatial mapping of the 10- to 59-Hz spontaneous brain wave amplitude. The location of STS is marked with dotted lines. (C) Streamlines plot at 0.9 s depicting the spontaneous propagating wave together with the vectors indicating the direction of propagating waves. Automatically detected epileptiform discharges for all channels in (D) 4-s and (F) 20-s time windows. (E) Raw waveforms selected from arrow-marked channels of (D). The channels are sorted according to the distance from the right lower (RL) corner of the electrode; the channel in the midline is closest to the lower right corner. (G) Time course and recordings of the stimulation pulse artifacts for time locking with evoked response. The stimulation sequence number and duration of stimulation time are indicated below the waveforms. (H) Number of channels showing epileptiform discharges over time. The yellow color indicates the stimulation time points, and the red colored regions mark significant enhancement in epileptiform discharge detection for stimulation numbers 4, 5, and 6 (P < 0.001). (I) Spatial mapping of epileptiform discharge rate after each stimulation trial. Stimulation locations on or near the electrode are indicated by pair of blue dots for the 14 stimulation trials. (J to M) Stimulation-evoked epileptiform discharges, similar to (B) to (F). (J) Spatial mapping of the 10- to 59-Hz stimulation-evoked brain wave amplitude. (K) Streamlines plot at 2.7 s depicting the stimulation-evoked propagating wave together with the vectors indicating the direction of propagating waves. (L) Automatically detected epileptiform discharges for all channels in a 4-s time window. The channels are sorted according to the distance from the stimulation point. (M) Raw waveforms selected from arrow-marked channels of (L). Propagating waves for (C) spontaneous epileptiform discharge and (K) stimulation-evoked epileptiform discharge. The red streamlines for (C) originate from the right lower corner, whereas those for (K) originate near the stimulation location. The blue circles in (K) are the bipolar stimulator contact points on the cortex.

(Fig. 5A) to induce interictal epileptiform activity (49–52). Control benchtop experiments on brain models made of gelatin confirmed that the PtNRGrid electrode and the electronics were not affected by the bipolar stimulation (fig. S39).

Passive mapping of the epileptogenic tissue with the PtNRGrid revealed ongoing epileptiform activity (Fig. 5, B to F), also shown in the spatial mapping of RMS amplitude of the neural activity filtered in the frequency window of 10 to 59 Hz at different time epochs (Fig. 5E). The onset of epileptiform activity began near the lower right corner of the grid, then spread across the vertical midline, and terminated at the lower left corner (Fig. 5B and movie S5). To investigate whether the observed epileptiform waves were consistent over time, we applied automatic detection algorithms, generally used for detecting interictal discharges (53), to all channels and generated a raster plot of the activity as a function of time (Fig. 5, D and F). After sorting the channels according to the distance from the lower right corner, we found a 20-s window with repetitive epileptiform events occurring about every 4 s across the entire grid (Fig. 5F), which is magnified to show a single event of a recurring epileptiform waveform within a 4-s time window (Fig. 5, D and E). These repeated epileptiform waves consistently originated from the lower right corner of the grid, spread across the entire grid within 1 s, and subsequently disappeared 1 s later. Automatically detected epileptiform events (Fig. 5E) exhibit clear temporal shifts between the spontaneous epileptiform waveforms from channel to channel (overlayed on a reconstructed brain model of the participant in movie S6). Collectively, these maps and videos provide further evidence of utility for the PtNRGrids for large-scale high-resolution mapping of such pathologic activity.

Active mapping was performed in the same patient (Fig. 5, G to M). Using the same epileptiform discharge detection algorithm as Fig. 5D, we counted the number of channels on the PtNRGrid that detected epileptiform discharges and plotted the number of events as a function of time (Fig. 5H). Spontaneous and repetitive epileptiform activity persisted across the entire recording. Regardless of the stimulation location, we observed that stimulation pulses with short duration (<1 s) did not increase the underlying spontaneous epileptiform discharge activity (Fig. 5I). However, longer stimulation trials of 1.4 to 1.9 s such as trials 4, 5, and 6 significantly increased the number of epileptiform discharge events (P < 0.001) for the recording channels within 16 mm from the stimulation point (N = 471, 199, and 304 for trials 4, 5, and 6, respectively), particularlyevents with characteristics similar to interictal discharges. The duration of the pulse determines the total delivered charge density that is correlated with evoked responses (54, 55). The spatially resolved heatmaps of the stimulation-evoked activity can be clearly observed where it can be noted that the longer trials (4 and 6) were characterized by significantly enhanced after-discharges detected around the stimulation positions (P < 0.001) (Fig. 5I).

In stimulation-evoked epileptiform discharges, we found a clear enhancement of the amplitude of detected epileptiform activity within the 10- to 59-Hz frequency window, which persisted for more than 5 s after the bipolar stimulation ceased (Fig. 5J; see also movie S7). By sorting the automatically detected epileptiform events according to distance from the stimulation center (Fig. 5L), we observed that the first epileptiform events were initiated near the stimulated region. After stimulation, bursts of epileptiform discharges occurred every 0.3 s and continued for a longer duration than the less-frequent spontaneous epileptiform discharges. These

phenomena are clearly exhibited in the raw waveform recordings from selected channels (Fig. 5, L and M) and can be viewed atop a reconstructed brain model of the participant (movie S8).

Last, we investigated the origin and spatiotemporal dynamics of both the spontaneous and stimulation-induced epileptiform activity using vector fields and streamlines. Immediately before epileptiform events, the vector fields are mostly incoherent (figs. S40 and S41) but become coherent near the larger-amplitude epileptiform events. The characteristics of the spontaneous epileptiform activity can be inferred from the red streamlines that originate from the right lower corner near the location of the lesion in this patient (Fig. 5C). In contrast, the streamlines for stimulation-evoked epileptiform activity originate and spread away from the position of the stimulator (Fig. 5K), demonstrating high-resolution spatial and temporal mapping of the sites of origin. Representative coherent streamlines and vector field arrows were selected to better illustrate the long-range propagating dynamics of epileptiform events (Fig. 5, C and K). The entire streamlines and vector field of epileptogenic activities at different time points are shown in fig. S40 for the spontaneous and in fig. S41 for the stimulation-evoked activities. The epileptogenic tissue tested by this experiment was removed as a planned left temporal lobectomy, which included lesional (cavernoma) tissue and all the epileptic neocortical tissue discerned by prior stereoelectroencephalography seizure mapping and was deemed resectable as well by the PtNRGrid. The patient remained seizure free to the date of this manuscript synthesis, which is about 6 months after surgery.

DISCUSSION

Our studies demonstrate the range of utility of PtNRGrids for high spatial and temporal recording of neural activity for research and clinical intraoperative use. The PtNRGrids were built on thin, transparent, and conformal substrates and were reconfigured in pitch and total cortical coverage with 1024 and 2048 low-impedance contacts over an area as large as 8 cm by 8 cm, scalable for rodent or human work. The fabrication was performed on a large-area, 180 mm-by-180 mm glass substrate with thin-film processes substantially advancing the manufacture of neural probes beyond the conventional 100-mm and 150-mm silicon (Si) substrates. The largerarea manufacturing afforded the capability to connect to thousands of channels and the formation of long metal strips to isolate the sterile surgical medium from the acquisition electronics for patient safety. In addition, the fabrication process afforded large-area coverage of the PtNRGrids on the brain (up to 8 cm by 8 cm achieved in this work) and safety and sterility in the operating room for intraoperative monitoring purposes. Successful transition to the large-area glass substrates opens the possibility of integrating the display panel-manufacturing technology with neurotechnology and promises excellent scalability, considering the size of the glass panel used in display industry (up to a few square meters) and the high-resolution lithography capability (1.2 µm for both metal line and space) of flat panel displays (56). The large-area glass substrates also offer potential advances in manufacturing biomedical devices for use in humans that can leverage electronic (thin-film transistors) and optoelectronic (light-emitting diodes and imagers) advances achieved by the display industry for utility in human biomedical devices.

A commonly voiced concern over increasing the channel count of microelectrode arrays is the potential for electrical cross-talk to introduce artifacts into the neurophysiological recordings. This electrical cross-talk is primarily a result of parasitic capacitance between neighboring leads and thus will scale directly with increasing trace length and inversely with their trace pitch. Thus, traces should be kept short to reduce these parasitic paths. The termination impedance of neighboring channels to tissue (the electrochemical interfacial impedance) also needs to be accounted for, especially for conventional high-impedance electrochemical interfaces, which can affect cross-talk through parasitic capacitance paths. However, this is not a concern for the low-impedance PtNR contacts, which maintain 1-kHz impedances that are at least 10 million times lower than the impedance of the parasitic capacitances.

We show high-fidelity broadband recordings from rodents, where the high spatial resolution of the PtNRGrids enabled identification of individual cortical columns from the surface of the brain. The PtNRGrids were easily translated to the intraoperative setting, enabling the first human recordings with 1024-channel PtNRGrids from 13 subjects and 2048-channel PtNRGrids from 1 subject. The PtNRGrids mapped sensory and pathological epileptiform activity from the surface of the brain and detected relevant somatosensory dynamics in high spatial resolution over a physiologically relevant cortical coverage. Previous investigations of propagation characteristics of beta waves in the human brain were carried out with a relatively small area coverage of 4 mm by 4 mm using Utah arrays (33, 57) or with ECoG grids with sparse 1-cm spatial resolution (34).

The PtNRGrids revealed the precise curvilinear nature of the M1-S1 FB with millimeter-scale resolution at a sampling frequency of 20 kHz, superior to the low-resolution boundaries identified with conventional ECoG grids (43) or the temporally limited fMRI (58). The SSEPs measured with PtNRGrids had interpeak amplitudes up to 214 μ V, compared to the 5- μ V interpeak amplitudes measured on the same patient with the clinical grid. Note that interpeak amplitudes have been observed to fall within a range of 5 to 120 µV in a 230-patient study of clinical ECoG grid recordings (39). The lower amplitudes on the clinical grid can be attributed to both a spatial averaging on their ~6000× larger surface area than the PtNR contacts and a lower conformity to the brain surface resulting from the 1-mm-thick substrate used in clinical grids (compared to the 6.6-µm-thick parylene C substrate used in our PtNRGrids). It is also possible that the clinical ECoG grid that has sparsely distributed contacts (1 cm) missed the cortical region with the highest SSEP amplitude because it is a usual practice to adjust the location and angle of the clinical ECoG grid to obtain maximum peak amplitude (39). We demonstrated high-resolution recordings from the surface of the human brain with 1024- and 2048-channel PtNRGrids, which enable high-resolution intraoperative recordings in neurosurgical operations, estimated to be as many as 13.8 million annually (59). However, the system in its current form does not enable chronic recordings, which have different design considerations that are beyond the scope of this work. To achieve chronic recordings, either denser custom-made connectors that are slim enough to be externalized through the scalp, as done in epilepsy monitoring, or direct integration of integrated circuits and wireless transceivers to the implant becomes necessary (25, 60). The engineering challenges for each part of the implant increase, and their safety and the durability of efficacy become critical.

We demonstrated a recording density up to 4444 cm $^{-2}$ (contact pitch, 150 μ m) using a single metallization layer of 10- μ m-pitch metal leads and 30- μ m-diameter PtNR contacts. To increase the

recording density, the width of the metal leads would need to decrease to enable tighter pitch, and thickness would need to increase to maintain low metal lead impedance. There are practical lithographic limitations for patterning narrow and thick metal leads necessitating the use of multilayer metallization, which relaxes the constrains on the metal lead width. By making dual- and triple-layer electrodes, the electrode density can increase up to 17,776 cm $^{-2}$ (contact pitch, 75 μ m) and 71,104 cm $^{-2}$ (contact pitch, 37.5 μ m), respectively. Higher recording densities beyond 71,104 cm $^{-2}$ would require a smaller PtNR contact diameter. A trade-off between the recording density and the impedance magnitude of the individual contacts will need to be considered.

The development of a real-time display of PtNRGrid recordings in a meaningful and potentially medically informative way holds the potential to improve surgical procedures. Although the higherresolution mapping can carry important implications for neurosurgical procedures, it is important to note that the surgical precision in current clinical practice does not meet millimeter-scale resolution. However, surgical resection boundaries obtained with current clinical electrodes are grossly determined with their 1-cm contact spacing. We anticipate that the PtNRGrids that determine surgical boundaries with millimeter-scale resolution might inform better resection practices by delineating the curvilinear nature of the functional and pathological boundaries that is not possible otherwise. With the development of higher-precision resection methods such as laser ablation or robot-assisted surgery, millimeter-scale spatial resolution recording might be useful for performing millimeter-scale resection of the brain tissue.

Last, the PtNRGrids were used for passive mapping in this work. Although the PtNRGrid has perfusion holes that enabled bipolar stimulation with external devices, direct current stimulation through the grid is desired. In addition, microstimulation of smaller tissue volume may be preferred, particularly for individual functional cortical columns that were isolated using the PtNRGrids. Extension of this work should enable stimulation through the PtNRGrids, which were shown in our earlier work, to hold one of the highest charge injection capacities for safe stimulation (27).

PtNRGrids hold promise for superior mapping during neurosurgical intervention through high spatial resolution and coverage while maintaining excellent broadband temporal resolution compared to the clinical electrodes. PtNRGrid technology has the capacity to scale to more than 2048 channels, to pave the way for better neurosurgical mapping strategies, and to enable possibilities for therapies, brain-computer interfaces, and better patient outcomes as the technology is advanced for chronic applications.

MATERIALS AND METHODS

Study design

Objectives of the study were to (i) demonstrate that 1024- and 2048-channel PtNRGrids have higher spatial resolution that better delineated FBs in the human brain than the standard clinical electrodes, (ii) test the signal amplitudes of PtNRGrids compared to the standard clinical electrodes, (iii) isolate the neural correlates and dynamic activity during motor and sensory tasks with high spatial resolution with the PtNRGrids, and (iv) investigate the microscale dynamics of spontaneous and stimulation-evoked epileptic discharges with the PtNRGrids. All animal experiments were approved by the University of California San Diego (UCSD) Institutional

Animal Care and Use Committee under protocol \$16020. We successfully gathered surface ECoG recordings of all intended stimulus-evoked responses and gathered postmortem histological stains from two rats. These data were not blinded, and we did not include a randomization of subject selection in this study.

Twenty human subjects were recruited to participate in this study under two Institutional Review Board (IRB) approvals (UCSD IRB #181556 and Oregon Health and Science University IRB #19099). Subjects were considered for recruitment if the details of their surgery coincided with a particular experimental paradigm, for example, motor mapping experiments required patients with an exposure of the motor and sensorimotor cortex and required clinical motor mapping to be part of their normal clinical care. We selected the types of PtNRGrids and tasks depending on the location and size of the craniotomy determined by the clinical team. Participants were informed of the research and given time to understand the risks and benefits of participation before being asked for consent. Data from each participant were deidentified before analysis, and each experimental paradigm included controls for acquiring a baseline recording before or throughout the given recording period. Trial numbers within a given subject recording were determined on the basis of a maximum recording time of 15 min in the operating room setting along with the number of variables being swept. The data collected from subjects with severe brain tumor; low responsiveness due to age, anesthesia, or surgical procedures; or task-unrelated cortical exposure were excluded from the study. We did not include a randomization of subject selection in this study because patient data were considered separate datasets. Experimental conditions and a summary of all subjects are presented in table S1.

Statistical analysis

All statistical comparisons were performed using nonparametric measures, so we did not test for normality. Spontaneous epileptiform discharge rates for each recording channel detected using automatic algorithms (53) were estimated from the 6-min baseline recording data. After-discharge rates induced by stimulation for all recording channels were estimated by taking a 4-s time window starting between 0.5 and 4.5 s after each bipolar stimulation. Sample sizes for each stimulation trial were the recording channels within a 16-mm radius from the bipolar stimulation site that also had electrochemical impedance below 100 kilohm at 1 kHz. Under these criteria, the numbers of channels (N) used in statistical analysis for each stimulation trial number (#) defined as $N_{\#}$ were as follows: $N_1 = 351$, $N_2 = 177$, $N_3 = 540$, $N_4 = 471$, $N_5 = 199$, $N_6 = 304$, $N_7 = 299$, $N_8 = 365$, $N_9 = 252$, $N_{10} = 357$, $N_{11} = 631$, $N_{13} = 284$, and $N_{14} = 633$. For the selected channels, Wilcoxon signed-rank test was used to analyze whether the stimulation significantly increased the number of discharges compared to that of the spontaneous discharges. Stimulation trial 12 was excluded from the statistical analysis because of the short time window between trials 12 and 13.

SUPPLEMENTARY MATERIALS

www.science.org/doi/10.1126/scitransImed.abj1441 Supplementary Materials and Methods Figs. S1 to S41 Tables S1 and S2 Movies S1 to S8 References (61–64)

View/request a protocol for this paper from Bio-protocol.

REFERENCES AND NOTES

- E. M. Maynard, C. T. Nordhausen, R. A. Normann, The Utah intracortical electrode array: A recording structure for potential brain-computer interfaces. *Electroencephalogr. Clin. Neurophysiol.* 102, 228–239 (1997).
- T. Yang, S. Hakimian, T. H. Schwartz, Intraoperative ElectroCorticoGraphy (ECog): Indications, techniques, and utility in epilepsy surgery. Epileptic Disord. 16, 271–279 (2014).
- 3. W. Penfield, H. Jasper, *Epilepsy and the functional anatomy of the human brain* (Little. Brown. 1954).
- H. Duffau, M. Lopes, F. Arthuis, A. Bitar, J. P. Sichez, R. van Effenterre, L. Capelle, Contribution of intraoperative electrical stimulations in surgery of low grade gliomas: A comparative study between two series without (1985–96) and with (1996–2003) functional mapping in the same institution. J. Neurol. Neurosurg. Psychiatry 76, 845–851 (2005).
- G. K. Anumanchipalli, J. Chartier, E. F. Chang, Speech synthesis from neural decoding of spoken sentences. *Nature* 568, 493–498 (2019).
- J.-P. Lachaux, N. Axmacher, F. Mormann, E. Halgren, N. E. Crone, High-frequency neural activity and human cognition: past, present and possible future of intracranial EEG research. *Prog. Neurobiol.* 98, 279–301 (2012).
- N. Mesgarani, C. Cheung, K. Johnson, E. F. Chang, Phonetic feature encoding in human superior temporal gyrus. Science 343, 1006–1010 (2014).
- T. Pistohl, A. Schulze-Bonhage, A. Aertsen, C. Mehring, T. Ball, Decoding natural grasp types from human ECoG. Neuroimage 59, 248–260 (2012).
- J. Kubanek, K. J. Miller, J. G. Ojemann, J. R. Wolpaw, G. Schalk, Decoding flexion of individual fingers using electrocorticographic signals in humans. J. Neural Eng. 6, 066001 (2009).
- T. Yanagisawa, M. Hirata, Y. Saitoh, T. Goto, H. Kishima, R. Fukuma, H. Yokoi, Y. Kamitani, T. Yoshimine, Real-time control of a prosthetic hand using human electrocorticography signals. J. Neurosurg. 114, 1715–1722 (2011).
- D. Khodagholy, J. N. Gelinas, T. Thesen, W. Doyle, O. Devinsky, G. G. Malliaras, G. Buzsáki, NeuroGrid: Recording action potentials from the surface of the brain. *Nat. Neurosci.* 18, 310–315 (2015).
- L. R. Hochberg, M. D. Serruya, G. M. Friehs, J. A. Mukand, M. Saleh, A. H. Caplan, A. Branner, D. Chen, R. D. Penn, J. P. Donoghue, Neuronal ensemble control of prosthetic devices by a human with tetraplegia. *Nature* 442, 164–171 (2006).
- J. Viventi, A conformal, bio-interfaced class of silicon electronics for mapping cardiac electrophysiology. Sci. Transl. Med. 2, 24ra22 (2010).
- J. Viventi, D. H. Kim, L. Vigeland, E. S. Frechette, J. A. Blanco, Y. S. Kim, A. E. Avrin,
 V. R. Tiruvadi, S. W. Hwang, A. C. Vanleer, D. F. Wulsin, K. Davis, C. E. Gelber, L. Palmer,
 J. van der Spiegel, J. Wu, J. Xiao, Y. Huang, D. Contreras, J. A. Rogers, B. Litt, Flexible,
 foldable, actively multiplexed, high-density electrode array for mapping brain activity
 in vivo. Nat. Neurosci. 14, 1599–1605 (2011).
- 15. N. V. Thakor, Translating the brain-machine interface. Sci. Transl. Med. 5, 210ps17 (2013).
- G. H. Wilson, S. D. Stavisky, F. R. Willett, D. T. Avansino, J. N. Kelemen, L. R. Hochberg, J. M. Henderson, S. Druckmann, K. V. Shenoy, Decoding spoken English from intracortical electrode arrays in dorsal precentral gyrus. J. Neural Eng. 17, 066007 (2020).
- L. R. Hochberg, D. Bacher, B. Jarosiewicz, N. Y. Masse, J. D. Simeral, J. Vogel, S. Haddadin, J. Liu, S. S. Cash, P. van der Smagt, J. P. Donoghue, Reach and grasp by people with tetraplegia using a neurally controlled robotic arm. *Nature* 485, 372–375 (2012).
- S. J. Bensmaia, D. J. Tyler, S. Micera, Restoration of sensory information via bionic hands. Nat. Biomed. Eng., (2020).
- C. E. Vargas-Irwin, J. M. Feldman, B. King, J. D. Simeral, B. L. Sorice, E. M. Oakley, S. S. Cash, E. N. Eskandar, G. M. Friehs, L. R. Hochberg, J. P. Donoghue, Watch, imagine, attempt: Motor cortex single-unit activity reveals context-dependent movement encoding in humans with tetraplegia. Front. Hum. Neurosci. 12, 450 (2018).
- M. Vigneau, V. Beaucousin, P. Y. Hervé, H. Duffau, F. Crivello, O. Houdé, B. Mazoyer, N. Tzourio-Mazoyer, Meta-analyzing left hemisphere language areas: Phonology, semantics, and sentence processing. *Neuroimage* 30, 1414–1432 (2006).
- M. S. Fifer, G. Hotson, B. A. Wester, D. P. McMullen, Y. Wang, M. S. Johannes, K. D. Katyal, J. B. Helder, M. P. Para, R. J. Vogelstein, W. S. Anderson, N. V. Thakor, N. E. Crone, Simultaneous neural control of simple reaching and grasping with the modular prosthetic limb using intracranial EEG. *IEEE Trans. Neural Syst. Rehabil. Eng.* 22, 695–705 (2014).
- W. Wang, J. L. Collinger, A. D. Degenhart, E. C. Tyler-Kabara, A. B. Schwartz, D. W. Moran, D. J. Weber, B. Wodlinger, R. K. Vinjamuri, R. C. Ashmore, J. W. Kelly, M. L. Boninger, An electrocorticographic brain interface in an individual with tetraplegia. *PLOS ONE* 8, e55344 (2013).
- S. Acharya, M. S. Fifer, H. L. Benz, N. E. Crone, N. V. Thakor, Electrocorticographic amplitude predicts finger positions during slow grasping motions of the hand. *J. Neural Eng.* 7, 046002 (2010).
- 24. C.-H. Chiang, S. M. Won, A. L. Orsborn, K. J. Yu, M. Trumpis, B. Bent, C. Wang, Y. Xue, S. Min, V. Woods, C. Yu, B. H. Kim, S. B. Kim, R. Huq, J. Li, K. J. Seo, F. Vitale, A. Richardson, H. Fang,

SCIENCE TRANSLATIONAL MEDICINE | RESEARCH ARTICLE

- Y. Huang, K. Shepard, B. Pesaran, J. A. Rogers, J. Viventi, Development of a neural interface for high-definition, long-term recording in rodents and nonhuman primates. *Sci. Transl. Med.* **12**, (2020).
- E. Musk, An integrated brain-machine interface platform with thousands of channels.
 J. Med. Internet Res. 21. e16194 (2019).
- K. Sahasrabuddhe, A. A. Khan, A. P. Singh, T. M. Stern, Y. Ng, A. Tadić, P. Orel, C. L. Reau, D. Pouzzner, K. Nishimura, K. M. Boergens, S. Shivakumar, M. S. Hopper, B. Kerr, M.-E. S. Hanna, R. J. Edgington, I. M. Namara, D. Fell, P. Gao, A. Babaie-Fishani, S. Veijalainen, A. V. Klekachev, A. M. Stuckey, B. Luyssaert, T. D. Y. Kozai, C. Xie, V. Gilja, B. Dierickx, Y. Kong, M. Straka, H. S. Sohal, M. R. Angle, The Argo: A high channel count recording system for neural recording in vivo. J. Neural Eng. 18, 015002 (2021).
- M. Ganji, A. C. Paulk, J. C. Yang, N. W. Vahidi, S. H. Lee, R. Liu, L. Hossain, E. M. Arneodo, M. Thunemann, M. Shigyo, A. Tanaka, S. B. Ryu, S. W. Lee, Y. Tchoe, M. Marsala, A. Devor, D. R. Cleary, J. R. Martin, H. Oh, V. Gilja, T. Q. Gentner, S. I. Fried, E. Halgren, S. S. Cash, S. A. Dayeh, Selective formation of porous Pt nanorods for highly electrochemically efficient neural electrode interfaces. *Nano Lett.* 19, 6244–6254 (2019).
- 28. F.-J. Liao (Google Patents, 2007).
- 29. H. Shirai, M. Inoue, S. Hashimoto (Google Patents, 2006).
- I. Uguz, M. Ganji, A. Hama, A. Tanaka, S. Inal, A. Youssef, R. M. Owens, P. P. Quilichini, A. Ghestem, C. Bernard, S. A. Dayeh, G. G. Malliaras, Autoclave sterilization of PEDOT: PSS electrophysiology devices. *Adv. Healthc. Mater.* 5, 3094–3098 (2016).
- 31. C. C. Petersen, The functional organization of the barrel cortex. Neuron 56, 339-355 (2007).
- 32. A. Keller, in The Barrel Cortex of Rodents (Springer, 1995), pp. 221–262.
- D. Rubino, K. A. Robbins, N. G. Hatsopoulos, Propagating waves mediate information transfer in the motor cortex. *Nat. Neurosci.* 9, 1549–1557 (2006).
- L. Muller, G. Piantoni, D. Koller, S. S. Cash, E. Halgren, T. J. Sejnowski, Rotating waves during human sleep spindles organize global patterns of activity that repeat precisely through the night. *eLife* 5, e17267 (2016).
- S. Ray, N. E. Crone, E. Niebur, P. J. Franaszczuk, S. S. Hsiao, Neural correlates of high-gamma oscillations (60–200 Hz) in macaque local field potentials and their potential implications in electrocorticography. *J. Neurosci.* 28, 11526–11536 (2008).
- M. Liguz-Lecznar, J. Skangiel-Kramska, Vesicular glutamate transporters VGLUT1 and VGLUT2 in the developing mouse barrel cortex. *Int. J. Dev. Neurosci.* 25, 107–114 (2007)
- E. Neafsey, E. L. Bold, G. Haas, K. M. Hurley-Gius, G. Quirk, C. F. Sievert, R. R. Terreberry, The organization of the rat motor cortex: A microstimulation mapping study. *Brain Res. Rev.* 11, 77–96 (1986).
- E. T. Fonoff, J. F. Pereira Jr., L. V. Camargo, C. S. Dale, R. L. Pagano, G. Ballester, M. J. Teixeira, Functional mapping of the motor cortex of the rat using transdural electrical stimulation. *Behav. Brain Res.* 202, 138–141 (2009).
- J. Romstöck, R. Fahlbusch, O. Ganslandt, C. Nimsky, C. Strauss, Localisation
 of the sensorimotor cortex during surgery for brain tumours: Feasibility and waveform
 patterns of somatosensory evoked potentials. J. Neurol. Neurosurg. Psychiatry 72,
 221–229 (2002).
- C. Cedzich, M. Taniguchi, S. Schäfer, J. Schramm, Somatosensory evoked potential phase reversal and direct motor cortex stimulation during surgery in and around the central region. *Neurosurgery* 38, 962–970 (1996).
- A. Haseeb, E. Asano, C. Juhász, A. Shah, S. Sood, H. T. Chugani, Young patients with focal seizures may have the primary motor area for the hand in the postcentral gyrus. *Epilepsy Res.* 76, 131–139 (2007).
- H. Duffau, J. P. Sichez, S. Lehéricy, Intraoperative unmasking of brain redundant motor sites during resection of a precentral angioma: Evidence using direct cortical stimulation. Ann. Neurol. 47, 132–135 (2000).
- C. C. Wood, D. D. Spencer, T. Allison, G. McCarthy, P. D. Williamson, W. R. Goff, Localization of human sensorimotor cortex during surgery by cortical surface recording of somatosensory evoked potentials. J. Neurosurg. 68, 99–111 (1988).
- M. Bleichner, M. J. Vansteensel, G. M. Huiskamp, D. Hermes, E. J. Aarnoutse, C. H. Ferrier, N. F. Ramsey, The effects of blood vessels on electrocorticography. *J. Neural Eng.* 8, 044002 (2011).
- E. Balzamo, P. Marquis, P. Chauvel, J. Regis, Short-latency components of evoked potentials to median nerve stimulation recorded by intracerebral electrodes in the human pre- and postcentral areas. Clin. Neurophysiol. 115, 1616–1623 (2004)
- G. Pfurtscheller, B. Graimann, J. E. Huggins, S. P. Levine, L. A. Schuh, Spatiotemporal patterns of beta desynchronization and gamma synchronization in corticographic data during self-paced movement. Clin. Neurophysiol. 114, 1226–1236 (2003).
- H. Shibasaki, M. Hallett, What is the Bereitschaftspotential? Clin. Neurophysiol. 117, 2341–2356 (2006).
- 48. G. Pfurtscheller, C. Neuper, Event-related synchronization of mu rhythm in the EEG over the cortical hand area in man. *Neurosci. Lett.* **174**, 93–96 (1994).
- 49. E. L. So, Integration of EEG, MRI, and SPECT in localizing the seizure focus for epilepsy surgery. *Epilepsia* **41**, S48–S54 (2000).

- A. Chari, R. C. Thornton, M. M. Tisdall, R. C. Scott, Microelectrode recordings in human epilepsy: A case for clinical translation? *Brain Commun.* 2, fcaa082 (2020).
- A. M. Taplin, A. de Pesters, P. Brunner, D. Hermes, J. C. Dalfino, M. A. Adamo, A. L. Ritaccio, G. Schalk, Intraoperative mapping of expressive language cortex using passive real-time electrocorticography. *Epilepsy Behav. Case Rep.* 5, 46–51 (2016).
- J. Jacobs, M. Zijlmans, R. Zelmann, A. Olivier, J. Hall, J. Gotman, F. Dubeau, Value of electrical stimulation and high frequency oscillations (80–500 Hz) in identifying epileptogenic areas during intracranial EEG recordings. *Epilepsia* 51, 573–582 (2010).
- R. Janca, P. Jezdik, R. Cmejla, M. Tomasek, G. A. Worrell, M. Stead, J. Wagenaar, J. G. R. Jefferys, P. Krsek, V. Komarek, P. Jiruska, P. Marusic, Detection of interictal epileptiform discharges using signal envelope distribution modelling: Application to epileptic and non-epileptic intracranial recordings. *Brain Topogr.* 28, 172–183 (2015).
- C. Donos, I. Mindruţă, J. Ciurea, M. D. Mălîia, A. Barborica, A comparative study
 of the effects of pulse parameters for intracranial direct electrical stimulation in epilepsy.

 Clin. Neurophysiol. 127, 91–101 (2016).
- C. C. McIntyre, W. M. Grill, Finite element analysis of the current-density and electric field generated by metal microelectrodes. *Ann. Biomed. Eng.* 29, 227–235 (2001).
- K. Iwamoto, in Novel Patterning Technologies for Semiconductors, MEMS/NEMS and MOEMS 2020 (International Society for Optics and Photonics, 2020), vol. 11324, p. 1132405.
- Z. W. Davis, L. Muller, J. Martinez-Trujillo, T. Sejnowski, J. H. Reynolds, Spontaneous travelling cortical waves gate perception in behaving primates. *Nature* 587, 432–436 (2020).
- T. Inoue, H. Shimizu, N. Nakasato, T. Kumabe, T. Yoshimoto, Accuracy and limitation of functional magnetic resonance imaging for identification of the central sulcus: Comparison with magnetoencephalography in patients with brain tumors. *Neuroimage* 10, 738–748 (1999).
- M. C. Dewan, A. Rattani, G. Fieggen, M. A. Arraez, F. Servadei, F. A. Boop, W. D. Johnson, B. C. Warf, K. B. Park, Global neurosurgery: The current capacity and deficit in the provision of essential neurosurgical care. Executive Summary of the Global Neurosurgery Initiative at the Program in Global Surgery and Social Change. *J. Neurosurg* 130, 1055–1064 (2018).
- J. D. Simeral, T. Hosman, J. Saab, S. N. Flesher, M. Vilela, B. Franco, J. N. Kelemen,
 D. M. Brandman, J. G. Ciancibello, P. G. Rezaii, E. N. Eskandar, D. M. Rosler, K. V. Shenoy,
 J. M. Henderson, A. V. Nurmikko, L. R. Hochberg, Home use of a percutaneous wireless intracortical brain-computer interface by individuals with tetraplegia. *IEEE Trans. Biomed. Eng.* 68, 2313–2325 (2021).
- S. M. Lauer, U. Schneeweiß, M. Brecht, S. Ray, Visualization of cortical modules in flattened mammalian cortices. J. Vis. Exp., e56992 (2018).
- A. L. Ritaccio, P. Brunner, G. Schalk, Electrical stimulation mapping of the brain: Basic principles and emerging alternatives. J. Clin. Neurophysiol. 35, 86–97 (2018).
- T. Kaiju, M. Inoue, M. Hirata, T. Suzuki, High-density mapping of primate digit representations with a 1152-channel μECoG array. J. Neural Eng. 18, 036025 (2021).
- 64. C.-H. Chiang, C. Wang, K. Barth, S. Rahimpour, M. Trumpis, S. Duraivel, I. Rachinskiy, A. Dubey, K. E. Wingel, M. Wong, N. S. Witham, T. Odell, V. Woods, B. Bent, W. Doyle, D. Friedman, E. Bihler, C. F. Reiche, D. G. Southwell, M. M. Haglund, A. H. Friedman, S. P. Lad, S. Devore, O. Devinsky, F. Solzbacher, B. Pesaran, G. Cogan, J. Viventi, Flexible, high-resolution thin-film electrodes for human and animal neural research. J. Neural Eng. 18, 045009 (2021).

Acknowledgments: We acknowledge insightful discussions with E. Halgren of UC San Diego, S. Cash of Massachusetts General Hospital, and A. Devor and M. Thunemann of Boston University. We are grateful for the technical support from the nano3 cleanroom facilities at UCSD's Qualcomm Institute where the PtNRGrid fabrication was conducted. This work was performed, in part, at the San Diego Nanotechnology Infrastructure (SDNI) of UCSD, a member of the National Nanotechnology Coordinated Infrastructure, which is supported by the NSF (grant ECCS1542148). Funding: This work was supported by the NIH award no. NBIB DP2-EB029757 to S.A.D., NINDS R01NS123655-01 to S.A.D., NINDS UG3NS123723-01 to S.A.D., and NIDA R01-DA050159 to S.A.D.; NSF award no. 1728497 to S.A.D. and CAREER no. 1351980 to S.A.D.; and an NSF Graduate Research Fellowship Program no. DGE-1650112 to A.M.B. Any opinions, findings, and conclusions or recommendations expressed in this material are those of the author(s) and do not necessarily reflect the views of the funding agencies. Author contributions: S.A.D. conceived and led the project, Y.T. fabricated the PtNRGrids, designed the tasks, and conducted all data analysis with S.A.D.'s guidance. A.M.B. designed the custom-made acquisition system and the motor task and stimulation capture hardware with input from I.G. and participated in data analysis; D.R.C., B.S., D.A.S., A.C.P., J.C.Y., S.B.-H., and A.M.R. performed tests and guided the electrode design for clinical translation. Y.T., A.M.B., K.L., and K.J.T. performed the rat experiments, and K.J.T. performed the histology. B.S., E.C.B., and A.M.R. designed clinical experiments and performed OR recordings; D.R.C., D.A.S., Y.T., A.M.B., and S.M.R. participated in some of the OR recordings, J.L. fabricated the PtNRGrids used in the sensory/motor tasks, and Y.G.R. and M.G. contributed to the fabrication process development. H.O. performed the bending cycle tests. A.C.P. and Y.T. composed the videos on the reconstructed brain models of subjects from fMRI and structural MRI. S.A.D. and Y.T. wrote

SCIENCE TRANSLATIONAL MEDICINE | RESEARCH ARTICLE

the manuscript, and all authors discussed the results and contributed to the manuscript writing. **Competing interests:** The authors declare the following competing interests: Y.T., A.M.R., and S.A.D. have equity in Precision Neurotek Inc. that is cofounded by the team to commercialize PtNRGrids for intraoperative mapping. S.A.D. and H.O. have competing interests not related to this work including equity in FeelTheTouch LLC. S.A.D. was a paid consultant to MaXentric Technologies. D.R.C., K.J.T., and D.A.S. have equity in Surgical Simulations LLC. A.M.R. has an equity and is a cofounder of CerebroAl. A.M.R. received consulting fees from Abbott Inc. and Biotronik Inc. The other authors declare that they have no competing interests. **Data and materials availability:** All data obtained in this study are either presented in the paper and the Supplementary Materials or deposited in open database. Animal brain recording data could be accessed at OpenNeuro (https://openneuro.

org/), and the human brain recording data could be found in Data Archive BRAIN Initiative (DABI) (https://dabi.loni.usc.edu/). Custom MATLAB code (version R2021a) in combination with open source automatic IID detection (www.ieeg.org) and propagating wave (https://mullerlab.github.io/) codes were used for the analyses and are available in GitHub (https://ytchoe.github.io/). The authors thank Dr. Woojin Choi for suggesting using the photoresist AZ5214 instead of NR9 3000 which significantly reduced the photolithography exposure time.

Submitted 23 April 2021 Accepted 15 December 2021 Published 19 January 2022 10.1126/scitranslmed.abj1441

Science Translational Medicine

Human brain mapping with multithousand-channel PtNRGrids resolves spatiotemporal dynamics

Youngbin TchoeAndrew M. BourhisDaniel R. ClearyBrittany StedelinJihwan LeeKaren J. TonsfeldtErik C. BrownDominic A. SilerAngelique C. PaulkJimmy C. YangHongseok OhYun Goo RoKeundong LeeSamantha M. RussmanMehran Ganjilan GaltonSharona Ben-HaimAhmed M. RaslanShadi A. Dayeh

Sci. Transl. Med., 14 (628), eabj1441. • DOI: 10.1126/scitranslmed.abj1441

Cortex in high resolution

Recording brain cortical activity with high spatial and temporal resolution is critical for understanding brain circuitry in physiological and pathological conditions. In this study, Tchoe *et al.* developed a reconfigurable and scalable thin-film, multithousand-channel neurophysiological recording grids using platinum nanorods, called PtNRGrids, that could record thousands of channels with submillimeter resolution in the rat barrel cortex. In human subjects, PtNRGrids were able to provide high-resolution recordings of large and curvilinear brain areas and to resolve spatiotemporal dynamics of motor and sensory activities. The results suggest that PtNRGrids could be used in the preclinical and clinical setting for high spatial and temporal recording of neural activity.

View the article online

https://www.science.org/doi/10.1126/scitransImed.abj1441

https://www.science.org/help/reprints-and-permissions

Use of think article is subject to the Terms of service

Science Translational Medicine

Supplementary Materials for

Human brain mapping with multithousand-channel PtNRGrids resolves spatiotemporal dynamics

Youngbin Tchoe et al.

Corresponding author: Shadi A. Dayeh, sdayeh@eng.ucsd.edu

Sci. Transl. Med. 14, eabj1441 (2022) DOI: 10.1126/scitranslmed.abj1441

The PDF file includes:

Supplementary Materials and Methods Figs. S1 to S41 Tables S1 and S2 Legends for movies S1 to S8 References (61–64)

Other Supplementary Material for this manuscript includes the following:

Movies S1 to S8

Materials and Methods

1. Fabrication, Packaging, and Connectorization of PtNRGrids

1.1. Fabrication of Reliable Fine Metal Traces on Parylene C Films

Polished and cleaned photomask-grade soda lime glass plate (Nanofilm) with dimensions of 7" × 7" × 0.06" were used as substrates for the fabrication. Prior to coating Micro-90 and parylene C films on the glass, the surface was treated with 200 W oxygen plasma for 5 min (Plasma Etch, Inc. PE100) to make the surface hydrophilic. We then spin-coated a 0.1% diluted and filtered Micro90 layer on the glass substrate as a release layer for the parylene C film in the last step of the fabrication process. Then, a 3.7-µm-thick-parylene C layer was coated on the vertically loaded glass substates using a parylene deposition system (Specialty Coating Systems 2010 Labcoter) Metal leads with width, spacing, and length of 4 μ m, 6 μ m, and > 10 cm respectively were formed on the parylene C layers by a standard lithography, descum, metal deposition, and lift-off process using the AZ5214E-IR photoresist (MicroChemicals), maskless photolithography system (Heidelberg MLA150), UV flood exposure system (DYMAX), plasma etcher (Oxford Plasmalab 80), and e-beam evaporator (Temescal). Metal leads were composed of Cr/Au (10/250 nm) and the entire lithography, deposition, and lift-off process was repeated on top of the first metal lead layer to form Cr/Au/Cr/Au (10/250/10/250 nm) metal leads. This double-patterning process was employed to increase yield and reduce risk of photoresist particles from compromising the thin traces.

1.2. PtAg Alloy Deposition for PtNRs

After the metal leads were prepared a 30µm-diameter-PtAg alloy was formed on the individual recording sites by photolithography, descum, and PtAg alloy co-sputtering using the maskless photolithography system with NR9-6000 (Futurrex) photoresist, plasma etcher, and magnetron DC/RF sputter (Denton Discovery 18), respectively. The detailed fabrication

methods and characteristics of PtNRs can be found elsewhere (27). Notably, this process involves a selective etching of silver in a dealloying process, leaving behind non-toxic platinum. A 50-nm-thick Ti capping layer was deposited on top of PtAg alloys to prevent oxidation in air or under oxygen plasma (see Fig. S1A).

1.3. Via Holes, Perfusion Holes, and Electrode Outline Etching

A second parylene C layer (3.1 µm) was then conformally deposited, preceded by an oxygen plasma treatment to enhance the adhesion between the layers. On top of the second parylene C layer, a Ti (50nm) hard mask was deposited and AZ5214E-IR photoresist was coated on top of the Ti layer and patterned to open via holes for recording sites, perfusion holes, and the outline of the electrodes (see Fig. S1B). An SF₆/Ar reactive ion etcher (Oxford Plasmalab80) was used to pattern the Ti layer through the photoresist, and 200 W oxygen plasma was used to etch parylene C films all the way through the surface of the glass substrate or Ti-cap layers of PtAg. The outline of the electrode was defined by a dry etching process to produce much more clearly defined sidewalls compared to those defined by a laser cutter, which usually yielded rough sidewalls and left black carbon microparticles. After completing the etching process, the substates were hard baked at 150°C for 40min to release the stress built up in the parylene C layers. Ti hard masks on parylene C and PtAg alloys were removed by dipping the sample in 6:1 buffered oxide etchant (BOE) and rinsing in DI water. The electrodes were lifted-off from the substrate in DI water with the dissolution of the underlying Micro90 layer. The released electrodes were then dealloyed on the surface of 60°C nitric acid for 2min with the PtAg alloy facing downward, thereby forming the PtNRs, which were then immersed and rinsed in DI water (see Fig. S1C). The microscopic morphology of the electrode is shown by the SEM images in Fig. S2.

1.4. Effect of Perfusion Holes in Achieving Highly Intimate Contact to the Brain Tissue

As the channel count and the area of the electrode scaled up to $3.2 \text{ cm} \times 3.2 \text{ cm}$, adherence of the electrode to the brain tissue was not fully preserved throughout the electrode area. Although the electrode was as thin as 6.6 µm, pockets of cerebrospinal fluid (CSF) as well as air bubbles were frequently trapped between the tissue and the electrode (Fig. S3F). These issues degraded the reproducibility of the recording due to the formation of dead zones (trapped CSF and possibly air bubbles). With the introduction of the perfusion holes, air bubbles or trapped CSF were not observed underneath the PtNRGrids in the OR (Fig. S3G), and the reproducibility of the human brain recording was greatly enhanced. We performed a benchtop experiment to demonstrate the effect of perfusion holes on adherence to the 3D objects (Figs. S3A-E). PtNRGrids with and without perfusion holes were placed on the red-colored gelatin droplet/PDMS mold and gently tapped with a gauze in the same manner. The PtNRGrid without the perfusion holes had trapped solution and air bubbles underneath it (Fig. S3B), and the cross-sectional image revealed that the separation between the electrode and PDMS can be as large as 200 µm (Fig. S3D). On the other hand, the PtNRGrids with the perfusion holes excellently conformed to the 3D PDMS mold (Fig. S3B), and the high proximity between the PtNRGrid and PDMS mold made it impossible to measure the thickness of the gap under the resolution of the cross-sectional microscope image shown in Figure S3E.

1.5. 1024 Channels PEDOT:PSS Electrode

The fabrication process of multi-thousand channel PtNRGrids is also compatible with poly(2,3-dihydrothieno-1,4-dioxin)-poly(styrenesulfonate) (PEDOT:PSS). Using a spin-coating and lift-off method, we successfully fabricated electrodes with PEDOT:PSS (see Fig. S4) and recorded from patients in both OHSU and UCSD under IRB authorization.

1.6. Bonding the Electrode to the Extender Printed Circuit Board (PCB)

The electrodes were then bonded on an extender PCB using silver epoxy (MG Chemicals 8331). Silver epoxy was selectively deposited on the footprints of an extender PCB through a 50-µm-thick silicone adhesive PET tape (Advanced Polymer Tape) stencil mask where holes were defined using a laser cutter (Universal Laser Cutter, VLS 3.50). The amount of silver epoxy that was required for reliable bonding was optimized by adjusting the size of the holes in the stencil mask. Micro-alignment stages with four-axis degrees of freedom were used to precisely align the PtNRGrid (that was temporarily placed on 5" × 5" glass plate) and the extender PCB (see Fig. S5A). Once aligned and placed in contact, the PtNRGrid and extender PCB were cured on 85°C hotplate for 15min under 5-10 N force to fully cure the silver epoxy and ensure electrical connection across all bonding contacts. The electrically bonded PtNRGrid was then released from the glass plate, and benchtop characterization of the electrodes was performed. Prior to the bonding, the PCB edge was grinded and smoothed to minimize the potential damage on the thin metal leads in parylene C films as shown in Fig. 5C. The bonding interface and the photos of the electrodes on both sides are shown in Figs. 5B, D, and E.

1.7. Connectorization and Acquisition Electronics

We developed a custom acquisition board using Intan Technologies' RHD2164 chipset to simultaneously record from up to 1024 channels with up to 30 kilo-samples per second (ksps) per channel. These chips contain an AC coupled differential analog front end (AFE) which applies a programmable bandpass filter (typically from 0.09 Hz to 7.6 kHz) and samples these signals with a 16-bit ADC. The total data throughput of the system was roughly 2.4 GB/min when sampled at 20 ksps. Given the proposed applications of this platform for use in microelectrocorticography, it is important to capture the full bandwidth of neurophysiological signals - from local field potentials to spiking and high gamma activity. To this end, our platinum

nanorod microelectrodes exhibited an average 1 kHz impedance magnitude in the tens of kiloohms which resulted in a high signal-to-noise ratio (SNR) for this particular AFE.

Although Intan Technologies offers an excellent platform for acquisition of ultra-high-resolution neurophysiology, they currently do not offer any scalable connectorization methods. It is known that the connectors are a major bottleneck in the effort to scale to thousands or hundreds of thousands of recording channels, thus we adapted connectorization techniques developed by the microelectronics industry. The first version of our acquisition board (denoted ORB1024 V1, see Fig. S6) used an off-the-shelf LGA1155 CPU socket to make an electrical connection to our sterilizable electrode arrays. Adopting this land grid array socket allowed us to temporarily and robustly connect to our flexible and sterilizable electrodes without having to integrate expensive acquisition chips into each electrode. The socket was placed in the center of the ORB1024 V1 to optimize routing and separate analog traces from digital. Additionally, a central cutout was made in the board to allow for back-side access to the center of the connector for in-vitro studies.

The ORB1024 V1 also includes a latching relay which selects between an on-electrode reference and an external needle reference. This latching relay is driven by a digital output from one of the RHD2164 chips which can be set through a software interface, allowing researchers to choose between these two options without physically touching the board (in an intraoperative setting, where the board is covered by a sterile drape). The board also includes a physical switch to select between shorting reference to ground or keeping them separate, which was often useful in animal and benchtop testing to optimize baseline noise performance prior to conducting experiments. Finally, touch-proof connectors are included to allow for clinical twisted-pair needle reference and ground electrodes to be connected, and an LED indicates power to the board.

2. Electrical, electrochemical, and mechanical characterization of PtNRGrids

2.1. Crosstalk and Noise of Ultra-High-Density Gold Interconnects

A commonly voiced concern over increasing the density of microelectrode arrays is the potential for electrical crosstalk to introduce artifacts into the neurophysiological recordings. This electrical crosstalk is primarily a result of parasitic capacitance between neighboring leads and thus will scale directly with increasing trace length and inversely with their trace pitch. Thus, traces should be kept short to reduce these parasitic paths. The termination impedance of neighboring channels to tissue (the electrolytic interfacial impedance) also needs to be accounted for, especially for conventional high-impedance electrochemical interfaces which can affect crosstalk through parasitic capacitance paths. However, this is not a concern for the low impedance PtNR contacts which maintain 1 kHz impedances that are at least 10 million times lower than the impedance of the parasitic capacitances. It should be noted that open channels on any grid including PtNRGrids can be problematic and these have been excluded (cut off of $100 \text{ k}\Omega$) from our analysis.

It is exceedingly difficult to measure crosstalk directly in a benchtop experiment in part because there is inherent shunting between neighboring channels at the electrode-tissue interface. Furthermore, the electrochemical impedance acts as a terminating impedance for neighboring channels (victim channels), meaning that simply grounding these channels would not be an adequate method of replicating a real-world setting. Thus, to investigate the crosstalk in our electrodes, we performed several benchtop measurements to isolate these parasitic capacitances as well as the electrochemical impedances of the PtNR microelectrodes in saline to generate an electrical model for the signal pathways.

A simplified circuit model detailing the relevant impedances of our PtNR microelectrode arrays is presented in Fig. S7. This model includes lumped models of each electrochemical impedance (denoted Z_{ex}), coplanar parasitic capacitance between

neighboring channels (denoted Cpx), parallel-plate parasitic capacitance between the electrolytic solution and each metal trace (denoted Cs), and finally, the amplifier input impedance which is reported by Intan Technologies to be 12pF. Here, we demonstrate the concept of an ideal isolated signal, Vi, and the paths this signal can take to couple on to neighboring channels (crosstalk). It is insightful to view this system as a current divider, where most of the leakage current in adjacent channels will be directed back through the low impedance electrolytic interfacial impedance (denoted Z ex) rather than through the amplifier.

We first measured the 1kHz electrochemical impedance of all 1024 channels on a freshly prepared microelectrode array and plotted the data spatially to find a region in the array with working neighboring channels whose leads ran adjacent to one another. Using a calibrated benchtop LCR meter, we then measured the impedance magnitude and phase (and subsequently extracted the equivalent parallel capacitance and resistance) over a frequency range of 1Hz to 1Mhz.

First, we measured the impedance between a platinum reference needle placed in phosphate buffered saline (PBS; Gibco® DPBS (1X) 14190-144), and the metal contact of the PCB bonded to our microelectrode array (which was also placed in PBS). Note that this measurement represented not only the electrolytic impedance, but also the trace impedance, contact resistances, and saline spreading resistance. We repeated this measurement for several neighboring electrodes and found similar measurements that matched well with our group's previously reported electrochemical impedance spectra of 30um diameter PtNR microelectrodes(27), indicating that these resistive components were small compared to the primarily capacitive electrolytic impedance of the PtNR electrode.

Next, focusing on the same set of neighboring channels (whose leads ran parallel to one another), we measured the impedance between adjacent channels (Fig. S8), channels separated by one (Fig. S9), and channels separated by two (Fig. S10). We repeated these

measurements under three conditions: The electrode floating in air (infinite termination impedance), the electrode floating over grounded PBS, but face up so as to only form a parallel-plate capacitance with the metal traces without forming an electrolytic interfacial impedance, and finally, with an equivalent but un-bonded PCB in air. The measurements with the electrode floating in air represented the coplanar capacitances, Cp1, Cp2, and Cp3. The measurements with the electrode flipped over grounded PBS represented the parallel combination of the coplanar capacitance with the parallel-plate capacitance. Finally, the measurement of the unbonded PCB was done to separate the parasitics of the PCB from the parasitics of the thin film metallization.

From the above measurements and model, we then derived a transfer function under two conditions: first, with a working neighboring channel whose electrochemical impedance, Ze2, is on par with the mean across the array (Fig. S11), and second, with an open neighboring channel whose electrochemical impedance, Ze2, is several orders of magnitude higher than the mean across the array (Fig. S12). We found that the amplitude of an input signal in adjacent channels (denoted Vr) is several orders of magnitude lower than the working channel (Vw) amplitude so long as the adjacent channels have proper termination impedance at the electrolytic interface. Importantly, this analysis is consistent with observed baseline recordings which clearly demonstrate low crosstalk. We also observed that in the limit as Ze2 $\rightarrow \infty$, the adjacent channel sees a capacitive voltage divider between Cp, Ca, and Cs, resulting in the bode plot (Fig. S12).

The above investigation shows that crosstalk is much worse when a channel has infinite electrochemical impedance. Of course, this is intuitively obvious, because if a channel is not working (is disconnected from the electrophysiologic medium), it essentially becomes an antenna that will only pick up noise. A very similar situation arises when thin-film metal traces crack or are disconnected by particles during fabrication near the electrode site. Thus,

when we say, "proper termination impedance", we essentially mean that the electrochemical impedance is non-infinite.

2.2. Bending Cycles Test

We performed 84,000 cycles of lead bend testing exceeding 90° bends (EN 45502) using a robotic gripper model 2F-140 (Robotiq) and custom made sample holders as shown in Fig. S13. We measured 755 functional contacts before bending (average impedance was 23 ± 3 K Ω for 30 μ m diameter contacts before and after all bending tests). After bending, 759 contacts were functional. The same device was then subjected to 205,000 lead bend cycles of -40° to $+40^{\circ}$ bends (ANSI/AAMI CI86:2017, recommended -15° to $+15^{\circ}$, 100,000 cycles). 752 contacts were functional after bending tests. The less than 1% change in number of functional channels is attributed to different contact latching between the device extender and the LGA socket on the acquisition board and is minimal indicating resilience of our electrodes to bending cycles.

3. Rat Whisker Barrel Recording

3.1. Surgical Procedures of Anesthetized Rat Craniotomy

All procedures were approved by the UCSD Institutional Animal Care and Use Committee. Male Sprague Dawley rats (10-18 weeks of age) from Charles River were sedated with 3-4% isoflurane and fixed in a stereotaxic frame (Kopf Instruments). Once stable, rats were reduced to 3% isoflurane for maintenance, while monitoring heart rate and breathing (Mouse Stat Jr, Kent Scientific). Prior to the craniotomy, contralateral side individual whiskers that were to be stimulated were colored with Sharpies to easily distinguish them in the air-puff stimulation experiment, and the remaining whiskers were trimmed off. A craniotomy was made on the right skull 1 cm lateral and 2 cm posterior from the bregma, exposing the somatosensory

(including barrel) cortex, over the right motor cortex. The dura was carefully opened and retracted from the brain, and a small piece of saline-soaked gauze was placed over the brain until the implant was ready. Once the craniotomy was complete, the rat was transitioned from isoflurane to ketamine/xylazine (100 mg/kg ketamine / 10 mg/kg xylazine) and re-dosed every 20-30 min for the duration of the experiment. Temperature, heart rate, and oxygen concentrations were monitored for the entirety of the experiment to ensure adequate anesthesia.

3.2. Implantation of PtNRGrid in Rat Model Undergoing Sensory Stimulation

The typical size of the craniotomy was $6 \times 6 \text{mm}^2$, and the $5 \times 5 \text{mm}^2$ 1024 channel PtNRGrid was implanted covering nearly the entire exposed area of the brain. The reference needle electrode was typically implanted near the neck of the rat, and ground was typically connected to a surrounding faraday cage or stereotaxis frame. Individual whiskers were stimulated with an air-puff stimulator using the Pneumatic PicoPump (WPI, PV830). Air-puff was delivered through a 1 mm diameter glass microcapillary tube with a pressure of 20 psi for single whisker stimulation and 40 psi for whole whiskers, neck, trunk, tail, and limbs stimulations. After a 10 s baseline recording, each whisker or organ was stimulated 50 times, once every 1 s. To minimize the chance of stimulating multiple whiskers other than the whisker of interest, whiskers were subsequently trimmed off after each recording. Electrical stimulations of the hindlimb and forelimb were done by inserting a pair of subdermal needle electrodes into the limb muscles and injecting bi-phasic current pulse (2.55 mA, 1 ms positive/1 ms negative) using the Intan RHS system. Both the air-puff and electrical stimulation were time locked to the recording system by sending TTL signals to both the stimulator and the Intan recording controller. From the animal model, we performed experiments with the PtNRGrid bonded to either a small PCB (Fig. S14D) or to an extender board (Fig. S14E). Both the small

PCB (Rat 1, 2, and 3) and extender PCB (Rat 4) recorded excellently localized HGA that is presented in Fig. S14.

3.3. Histology of the Rat Brain

After recordings, the sedated rat was euthanized and the corners of the PtNRGrids were marked by vertically puncturing the brain tissues with Dil (InvitrogenTM)-coated ultrafine tungsten probe tips (The Micromanipulator Company). The brain was then rapidly dissected and placed into 4% paraformaldehyde (PFA) solution in phosphate-buffered saline (PBS) at room temperature for 2 hours. Each hemisphere of the cortex was then peeled away and flattened per Lauer et al. (61). Briefly, cortices were flattened between two glass slides in 0.1 M PB for 24 hours at 4° C, to the thickness of 2 mm (using two other standard slides as supports). Flattened cortices were fixed overnight in 4% PFA at 4° C and then transferred to 30% sucrose. Once the tissue had sunk, they were sectioned at 50 µm on a cryostat and serial sections were collected in a 24-well dish in PBS. Alternate sections were washed in PBS and underwent antigen retrieval for 20 min in heated 1X Citra buffer (Biogenex Laboratories). Slices were washed in PBS and underwent a protein block in PBS-T (0.03% Triton-X) with 5% goat serum (Vector Labs, S-1000) for one hour. Slices were then incubated in rabbit antigoat VGLUT2 antibody (Abcam, ab216463, 1:1000) in PBS-T overnight at 4° C. The next day, slices were washed in PBS and incubated for 30 min in secondary (1:100 goat anti-rabbit 488 (Thermo-Fisher, A11008)) in PBS-T. Slices were washed, mounted, and cover-slipped using ProLong Gold (Thermo-Fisher). Images were acquired at the UCSD Nikon Imaging Core using a Nikon Eclipse Ti2-E equipped with a DS-Qi2 CMOS camera, controlled by NIS-E-Elements (Nikon). Images were processed using Image J.

3.4. Spatial Mapping, Channel Selection, and 60 Hz Noise Notch Filter for Rat Brain Recording

The 1024 channels recorded with the customized amplifier boards and the Intan recording controllers were mapped to the spatial coordinates of the individual recording sites on the PtNRGrids. We tabulated this mapping in a spreadsheet for each type of electrode and used this information to spatially display the impedance magnitudes, waveforms, and potentials. The channels with above $100~\mathrm{k}\Omega$ *in vivo* impedance magnitudes at 1 kHz were deemed open channels and excluded from the analysis. Neighboring channels with exceedingly low impedance magnitude from the norm were also evaluated as potential shorts. All recorded signals, unless specified as 'raw' signal, were first processed by eliminating 60 Hz and their noise harmonics with digital notch filters.

3.5. Localization of the Neural Responses in Rat Experiments

The waveforms presented in Figs. 2B and C are the N=50 trial average of the raw waveforms based on the TTL pulses time-locked to the air-puff stimulation. We then rereferenced the recorded signals by subtracting the common-averaged signal across channels. The common-average was calculated either by taking the average of all the working channels or by taking the average of a few selected channels. The problem of taking common-average from all the working channels was that, due to the high SNR of PtNRGrids, clear stim-evoked neural response was present in the common-average even after averaging signals from all the channels. Because of this, the re-referencing process caused negative-potential deflection on the channels that recorded no neural response which we believed was misleading. For this reason, we performed common-average referencing by averaging signals from ten channels that did not show ECoG responses. This effectively removed the motional artifacts, electrocardiogram, and low frequency noise. The signals were digitally filtered using a

Butterworth 4th order filter under selected frequency windows, and 50 trials were aligned and averaged based on the TTL pulses that triggered air-puff or electrical stimulation. All digital filters were implemented in Matlab using the zero-phase distortion filtering function, "filtfilt", which effectively doubled the filter order to 8. The amplitude of the signals in each frequency window were calculated by taking root-mean-square (RMS) of the absolute value of the Hilbert transformed signal in a 10~100ms time window after the stimulation.

Since the stim-evoked peak responses usually appeared a few milliseconds offset from each other, we also calculated trial averaging by finding the maximum correlations between the stim-evoked responses between trial epochs (see Fig. S18). Compared to the trial average taken by the TTL pulses, the trial average taken by the maximum correlation approach showed higher peak response and better represented individual trials in terms of pulse width due to the reduced jitter between trial epochs. The spatial mapping of high gamma activity (HGA) was calculated by taking RMS of the HGA in 2 ms time windows near the peak response for all the channels. We used customized colormaps to further define the spatial extent of HGA colormap (see Fig. S19). For superimposing the spatial mapping of HGA on top of desaturated VGLUT2 histology image, we used the 'Color' blending mode in Adobe Photoshop that preserved the grey levels in the background histology image while adding hue and saturation of the colored localized HGA (Fig. 2E).

3.6. Rat Whisker Barrel Experiment

We recorded sub-millimeter scale localized HGAs from four different rats as shown in the overlaid HGA mapping evoked by different whiskers or limb stimulations as shown in Figure S20. All stimulation were air-puff, except the forelimb and hindlimb electrical stimulation for Rat 4. Rats 1-3 were recorded with PtNRGrid bonded on small PCBs, while Rat4 was recorded using a PtNRGrid bonded on an extender board.

We performed different number and type of tasks for each rat since the conditions of the rats were variable. For example, Rat 3 was not doing well after three whisker stimulations, and we had to terminate the experiment after C2, C3, C4 whisker stimulation. We note that for every stimuli and task we performed, we did observe a corresponding submillimeter region of neural correlates.

4. Human Brain Recording

4.1. Participant and Task Information

Table S1 summarizes the participant, electrode, and task information.

4.2. Sterilization of the Electrodes

The PtNRGrid was packaged in DuraHolder Instrument Protection System (Key Surgical) pouches that kept the electrodes flat during the sterilization process for Steam Sterilizers (Steris) and V-PRO (Steris) as shown in Fig. S21A. The electrodes sterilized by STERRAD® (ASP Global Manufacturing, GmbH) were packaged with Plasma-CelTM Instrument Foam Protection (Healthmark Industries). The pouch and foam effectively protected the PtNRGrid during the sterilization process by providing non-stick cushions and keeping them flat under multiple cycles of chamber pressure changes while allowing steam or aerosolized hydrogen peroxide to freely access the electrodes. Even after standard interstate shipping (FedEx Air Freight), the characteristics of PtNRGrids packaged in DuraHolder pouches were unaltered, confirming the robustness of the PtNRGrids as well as the packaging method. The packaged electrodes were placed inside a sterilization tray on top of an autoclave-compatible silicone mat and underwent a sterilization process. For steam sterilizers, we used Gravity mode 121°C, 30 min process, and, for V-PRO and STERRAD, we used a default sterilization mode. The PtNRGrids were compatible with all the sterilization systems

mentioned above. However, the electrode sterilized by the steam sterilizer often experienced an increase of electrochemical impedance depending on the maintenance state of the heater unit or the purity of the tap water used for steam generation. We believe that the observed increase in impedance magnitude has to do with the adsorbates and impurities from the tap water that incorporates into the electrochemically active sites in PtNRs. Since both V-PRO and STERRAD® use reagent grade hydrogen peroxide, we did not observe an increase in impedance for PtNRGrids after these sterilizations. Most of the results presented in this work were recorded with the PtNRGrids sterilized by V-PRO.

4.3. Sterile Procedures in the Operating Room and the Implantation

The sterilized PtNRGrids were transferred onto a sterile Mayo Stand, and 2/3 of the extender board was inserted through an opening cut in a Situate Sterile Drape (Medtronic 01-0020). Another hole was opened on the Sterile Drape to insert the touch-proof connectors of a sterile twisted pair of subdermal needle electrodes. Tegaderm films (3M) that are impervious to liquids, virus, and bacteria were applied on both sides to seal the gaps between the extender board, wires of needle electrodes, and the sterile drape (Fig. S21B). While the sterile person was holding the outer surface of the Sterile Drape together with the PtNRGrid, the non-sterile person accessed the inner surface of the Sterile Drape and established a connection between the extender board and the amplifier board that was connected with the recording controller through SPI cables (Figs. S21C and D). After connecting the electrode on the amplifier board, the non-sterile person pulled the 2-meter-long Sterile Drape from the inner side to cover all the non-sterile items. This setup allowed us to bring the sterilized PtNRGrids connected to the amplifier board close to the surgical field. Prior to implant, the connectorization of PtNRGrid was first validated by measuring the impedance magnitudes in sterile saline (Fig. S21E), and then implanted onto the patient's brain (Fig. S21F). The Greenberg® Retractors (Symmetry

Surgical GmbH) clamped on the surgical table stabilized the position of the amplifier board. After the PtNRGrid was implanted, subdermal needle electrodes that served as reference and ground were implanted on the temporalis muscle near the recording field.

4.4. Stimulation Capture System

A common experimental paradigm we used took advantage of neuromonitoring procedures wherein a patient's median or ulnar nerves are electrically stimulated while somatosensory evoked potentials (SSEPs) are monitored in order to map the central sulcus functional boundary. The time delay between stimulation and SSEP detection is critical for this paradigm, thus we needed to capture the clinical stimulation signal in parallel with the neurophysiologic signals. This posed a challenge of capturing the timing of stimulation without modifying the clinical medical equipment in any way. The clinical equipment used for bipolar stimulation did not provide digital means of synchronization, thus we developed a custom differential capacitive sensing system which wrapped around the stimulation leads and captured the timing and amplitude information and provided a TTL synchronization signal which was split to the Intan 1024-channel recording controller (see Fig. S22).

4.5. Spatial Mapping, Channel Selection, and 60 Hz Noise Notch Filter for Human Brain Recording

The 1024 and 2048 channels recorded with the customized amplifier boards and the Intan recording controllers were mapped to the spatial coordinates of the individual recording sites on the PtNRGrids. We tabulated this mapping in a spreadsheet for each type of electrode and used this information to spatially display the impedance magnitudes, waveforms, and potentials. The channels with above $100 \text{ k}\Omega$ *in vivo* impedance magnitudes at 1 kHz were deemed open channels and excluded from the analysis. Neighboring channels with exceedingly

low impedance magnitude from the norm were also evaluated as potential shorts. All recorded signals, unless specified as 'raw' signal, were first processed by eliminating 60 Hz and their noise harmonics with digital notch filters.

4.6. Central Sulcus Localization

Signals were digitally filtered in the frequency window of 10-3000 Hz using a Butterworth 4th order filter with Matlab's "filtfilt" function. No re-referencing was used since this could potentially cause an undesirable offset in SSEPs. The train of peripheral nerve stimulation pulses was captured by our differential capacitive sensing system and was used to determine time epochs for trial averaging (N=10~20) the SSEPs. The peripheral nerve electrical stimulation pulses also appeared as sharp stimulation artifact peaks in the ECoG signals, which equivalently worked well to indicate timing of each trial. Since the electrical stim-artifacts agreed so well with the signals captured by the stim capture system, in the later experiments we did not set up the stim capture system and fully relied on the stim-artifacts to align trials.

4.7. 2048 Channels Electrode Recording Platform

The scalable approach of PtNRGrid allowed us to scale the electrode coverage as large as $8 \times 8 \text{ cm}^2$ and to multiple thousands of channels. We fabricated 2048 PtNRGrids and implanted the grid under IRB authorization at OHSU. The image of the electrode, sterilization method, and implantation method photos can be found in Fig. S27, and the 2048-channel recording system connection diagram is illustrated in Fig. S28. The craniotomy of the subject in this case was only $5 \times 5 \text{ cm}^2$, so we were not able to record from the entire area of the grid. In the first implantation, including the region slid under the skull, we implanted the right half of the grid (see Figs. S27E and G). We recorded from the grid in this configuration during a

motor-sensory task for 10min, and then trimmed the electrode as shown in Fig. S27D to make it narrower for ease of implantation. After trimming, the implantation was performed as shown in the lower panel of Fig. S27E without parts of the electrode being folded. The impedance mapping before trimming, after the first implantation, and after the trimming and second implantation are shown in Figs. S27F-H. The slight differences in impedance magnitudes between the left and the right side of the electrode are most likely related to the two separate reference and ground electrodes used for each side of the electrode. This difference could be reduced by splitting the reference and ground electrode connected to the two separate recording systems.

The criteria to choose the 1024 vs the 2048 versions in the in vivo human recordings is related to the size of the craniotomy. It is only possible to fit the 8×8 cm², 2048 version PtNRGrid for a patient who needed a larger craniotomy as deemed necessary by the clinical procedure. Most of the cases that were suitable for human electrophysiological recordings had craniotomy area $\leq 5 \times 5$ cm².

4.8. Multi-Thousands Channel Electrode and Implantable Electrode Recording Platform

Scaling from 1024 to 2048 channels was achieved simply by adding one more set of recording system, and, as much as the surgical area allows, more recording systems could be added to further increase the channel count to several thousands. However, from a practical standpoint, the electronic acquisition units will become crowded and bulky as the channel count increases beyond 4096 channels. To further increase the channel counts while minimizing the space the recording system occupy near the surgical field, higher density connectorization system is being developed (Fig. S29). The amplifier boards having 0.4 mm pitch, higher-density LGA connector and the mock-up of implantation and connector system for 4096 channel is described in Fig. S29.

4.9. Motor Glove Experimental Platform

Many intraoperative cases exposing motor cortex provided us with a unique opportunity to investigate neural correlates between surface recordings and motor tasks in awake patients. In order to take full advantage of these opportunities, we developed a custom glove system that was capable of capturing 9 degrees of freedom (flexion/extension of each finger and wrist, and 3D acceleration of the hand) and could provide vibrotactile stimulation to each fingertip (see Figs. S32A-B). The system connected to a dedicated task tablet, providing and capturing the timing of visual and audio instructions to the patient. The system also included a hand-held button which allowed researchers to capture gross timing information of improvised tasks. Each buffer of data sent from the glove system to the task tablet was marked by a TTL synchronization pulse which was split to the Intan Technologies recording controller unit to time-lock this information to the neural data.

4.10. Human Brain Somotosensory HGA Localization

Recorded data were re-referenced to ten selected channels as discussed in the rat signal processing section and were digitally filtered in the high gamma frequency band of 70-190 Hz using a Butterworth 4^{th} order filter with Matlab's "filtfilt" function. The action of the vibratotactile stimulators was clearly captured on the accelerometers in the glove system, which was used to time lock the sensory input event to the ECoG recording. The amplitude of HGA over time was calculated by taking the absolute value of Hilbert transformed data. We then took the standard deviation, σ , of the baseline noise for each channel with an assumed average of zero, which is equivalent to calculating the RMS value. The RMS values were then taken from the high gamma responses evoked by individual finger stimulations. By dividing the RMS HGA with the noise floor RMS value, we obtained a normalized metric for how many σ the

signal deviated from the noise floor for each channel. This method provided more reliable spatial mapping results compared to the potential mapping method since the noise amplitude significantly varied over channels for this particular recording due to the variation in *in vivo* impedance. ECoG response of sensory stimulation of each finger was spatially mapped with a color range of $1\sim4\sigma$, overlayed on top of each other by 'Multiply' blending mode and superimposed on top of a desaturated craniotomy photo using 'Color' blending mode in Adobe Photoshop.

4.11. Human Brain Motor High Gamma and Beta Wave Analysis

The data was re-referenced and digitally filtered in a high gamma frequency band of 70-190 Hz and beta band of 9-18 Hz using a Butterworth 4th order filter with the "filtfilt" function in Matlab. Amplitudes were calculated by taking the absolute value of the Hilbert transformed data. The hand motion captured by the flexion sensor was used to time lock the event with the ECoG signals. The spatial mapping of HGA in the sigma unit was obtained by dividing the RMS signal from RMS baseline noise. The high gamma amplitudes in Figs. 4E and F are shown without any baseline noise subtraction.

4.12. Human Brain Propagating Beta Wave Signal Processing

The propagating dynamics of the beta waves were calculated by taking the spatial phase gradients of the beta waves following the methods described in Rubino *et al.*(33) and Muller *et al.* (34). The phase angle of the beta wave for each channel was calculated by taking the inverse tangent of the imaginary part over the real part of Hilbert transformed data, and the phase was unwrapped over time. The propagation directions of the beta waves calculated from the spatial phase gradient were represented as a vector field and red and blue streamlines originating from SI and MI cortex, respectively, were used to visualize the long-range

propagation directions of the waves. The streamlines were plotted using the streamline function in Matlab with a default setting. To validate if the propagating wave model applied to the 1024 channel grid could properly interpret the traveling direction of the waves, we plotted the vector fields for artificial gaussian wave models rotating, linearly moving, expanding, shrinking, and changing in amplitude as shown in Fig. S34. The vector fields effectively expressed the propagating direction of the artificial gaussian waves. The vector field became incoherent for a stationary gaussian wave that only changed in amplitude (Fig. S34G), which is in agreement with the previous works (34).

4.13. Stimulation compatibility test through the PtNRGrids

Prior to doing the bipolar stimulation experiment on the surface of the human brain, we first conducted benchtop tests on brain models made of gelatin to investigate if any of the PtNRGrid electrode or electronics are affected by the bipolar stimulation. By adding 0.1M KCl to the gelatin model brain, the conductivity of the model brain was matched to the tissue conductivity of the pig brain. The model brain surface was wet with saline prior to bipolar stimulation as is usually done in the operation room. We stimulated with biphasic stimulating pulses (30 Hz) up to 2.55 mA with 1 ms pulse width and did not observe any damage on the PtNRGrid contacts, wires, or acquisition electronics which suggested there was no leakage current passing through the electrode itself. Potential mapping performed with the PtNRGrid (Fig. S39B) directly shows that the underlying gelatin tissue was electrically stimulated through the perfusion holes, indicating a current path formed through the gelatin channel underneath the PtNRGrid.

The effective contact area of the Ojemann bipolar stimulator probe is known to be 1.6 mm², and it is a common practice to use the current of 1-10 mA(62). When stimulating through the perfusion holes, in any of the contact points on the grid, at least 4 perfusion holes with 0.5

mm diameter were in contact to the Ojemann probe which makes up an effective contact area of >0.8 mm². Considering that the current and charge density could be doubled with the reduction in effective contact area, we limited the stimulation parameter to 0.5 - 5 mA when stimulating through the grid. The stimulation current could go further up by increasing the density and/or size of the perfusion holes.

4.14. Human Brain Epilepsy Monitoring Processing

The data was digitally filtered with a passband of 10-59 Hz using the Butterworth 4th order filter and the "filtfilt" function in Matlab. No re-referencing was done for this set of data to preserve the epileptiform activities happening throughout the entire surface of the grid. Spatial mapping of the amplitudes of the epileptiform activities were calculated by taking the RMS of the potentials in 50 ms time windows. Epileptiform activity was automatically detected by employing an automatic detection algorithm developed to capture interictal discharges in Janca *et al.*(53). The channels were sorted according to the 2D Euclidean distance from the suspected onset zone of the epileptiform activities. The bi-polar stimulation events were clearly captured as large amplitude artifacts by the PtNRGrids, and the stimulation positions were recorded by the surgical microscope video. Adopting the same phase gradient and streamline approach described above, we estimated the propagating direction of the epileptiform activities near the onset zone.

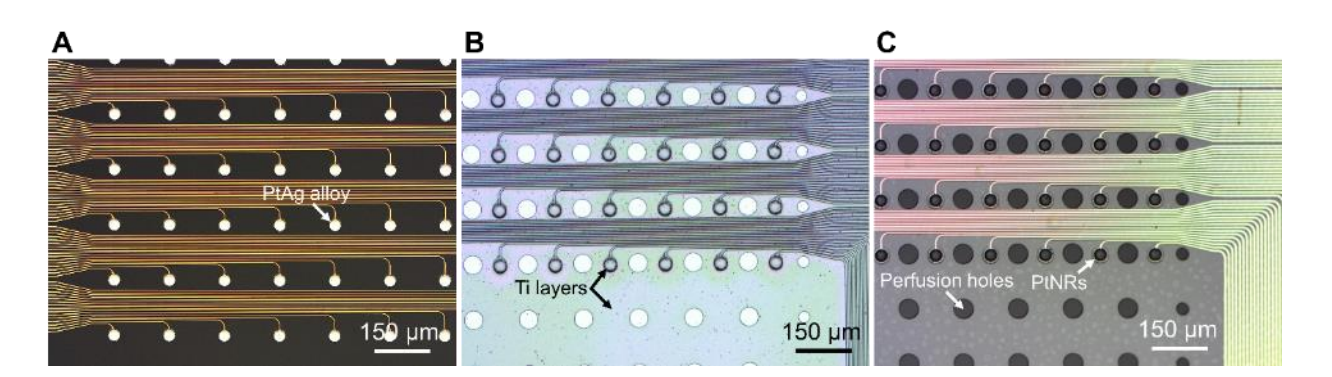


Figure S1. Microscope images during the fabrication processes. (A) Metal leads and PtAg alloy capped with Ti hard mask on 1st parylene C layer. (B) After 2nd parylene C deposition

and Ti hard mask deposition. Photoresist is patterned for via hole etching. (C) After Ti hard masks removal and dealloying.

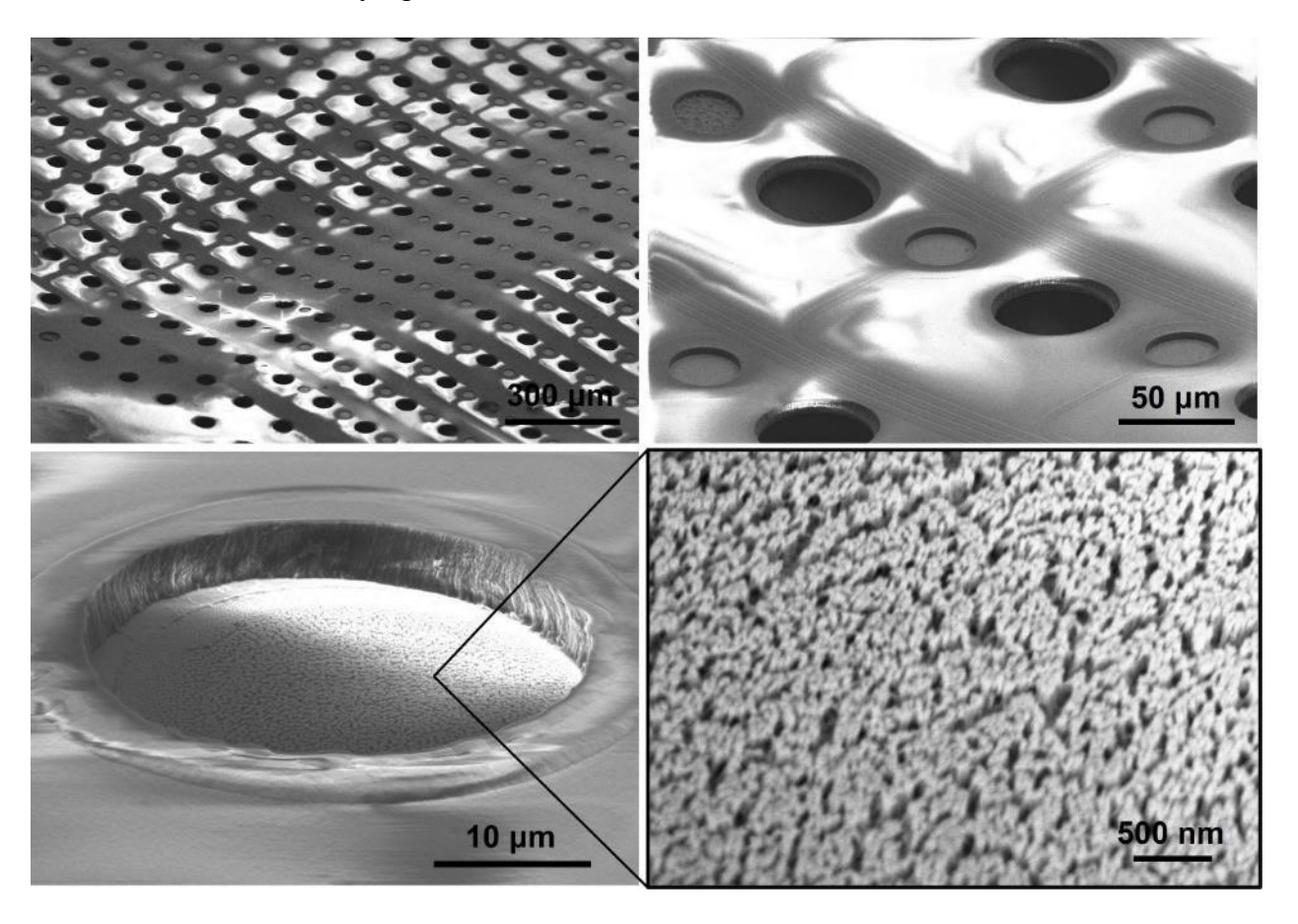


Figure S2. SEM images at different magnifications of the PtNRGrid and contacts.

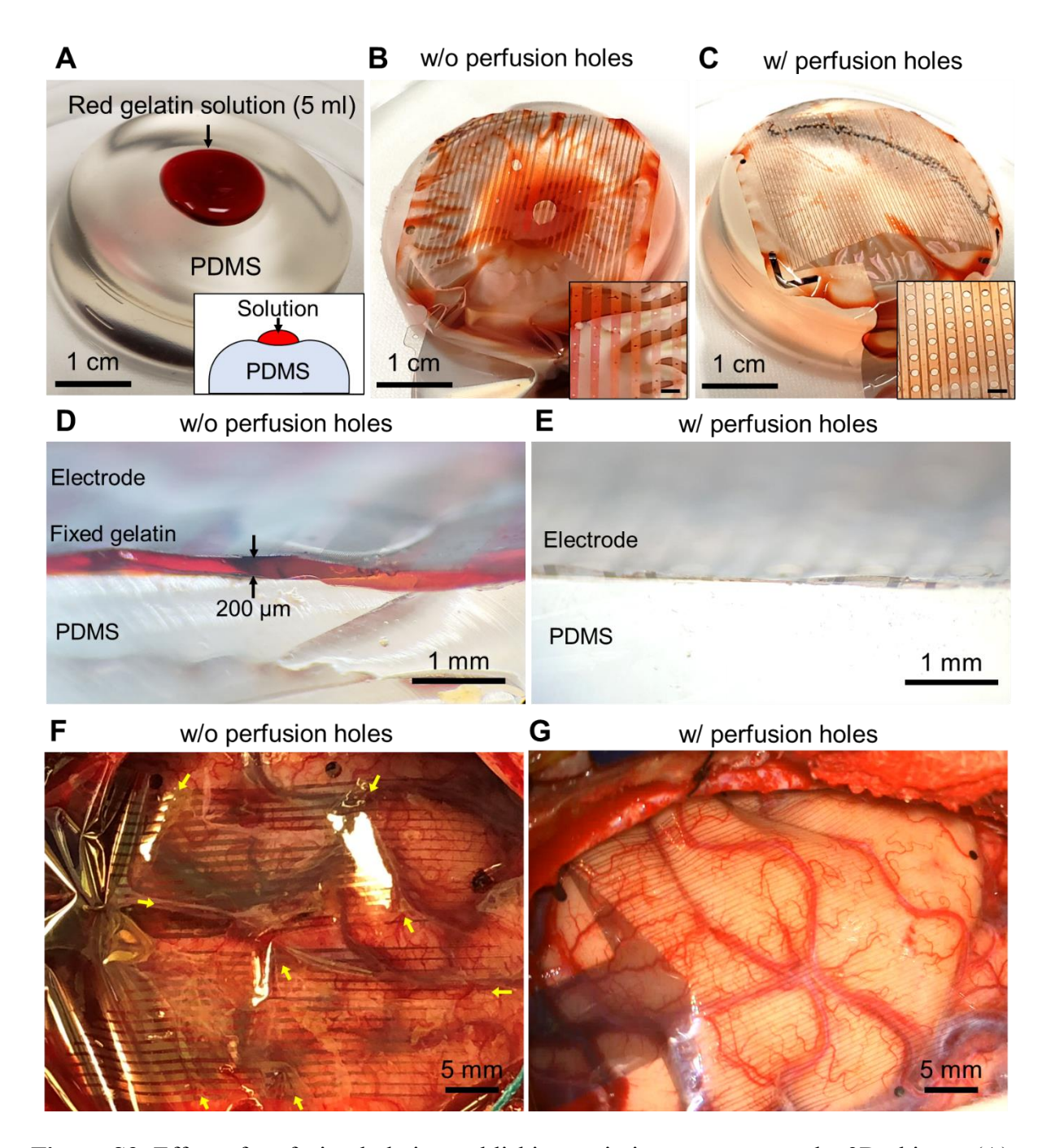


Figure S3. Effect of perfusion hole in establishing an intimate contact to the 3D objects. (A) Red gelatin solution droplet close to the human body temperature on top of the PDMS tissue model. The top surface of the PDMS model was a little recessed as depicted in the inset cross-sectional schematic. PtNRGrids (B) without and (C) with perfusion holes were placed on top of the red gelatin droplet/PDMS block and gently tapped with a gauze in the same manner. Inset figures in (B) and (C) shows the magnified photos with 1 mm scalebars. Cross-sectional images of the liquid (fixed red gelatin) trapped between the PDMS tissue model and the PtNRGrids (D) without and (E) with perfusion holes. PtNRGrids (F) without and (G) with perfusion holes on top of human brain surface. The positions where CSF is trapped underneath the electrode is marked with yellow arrows.

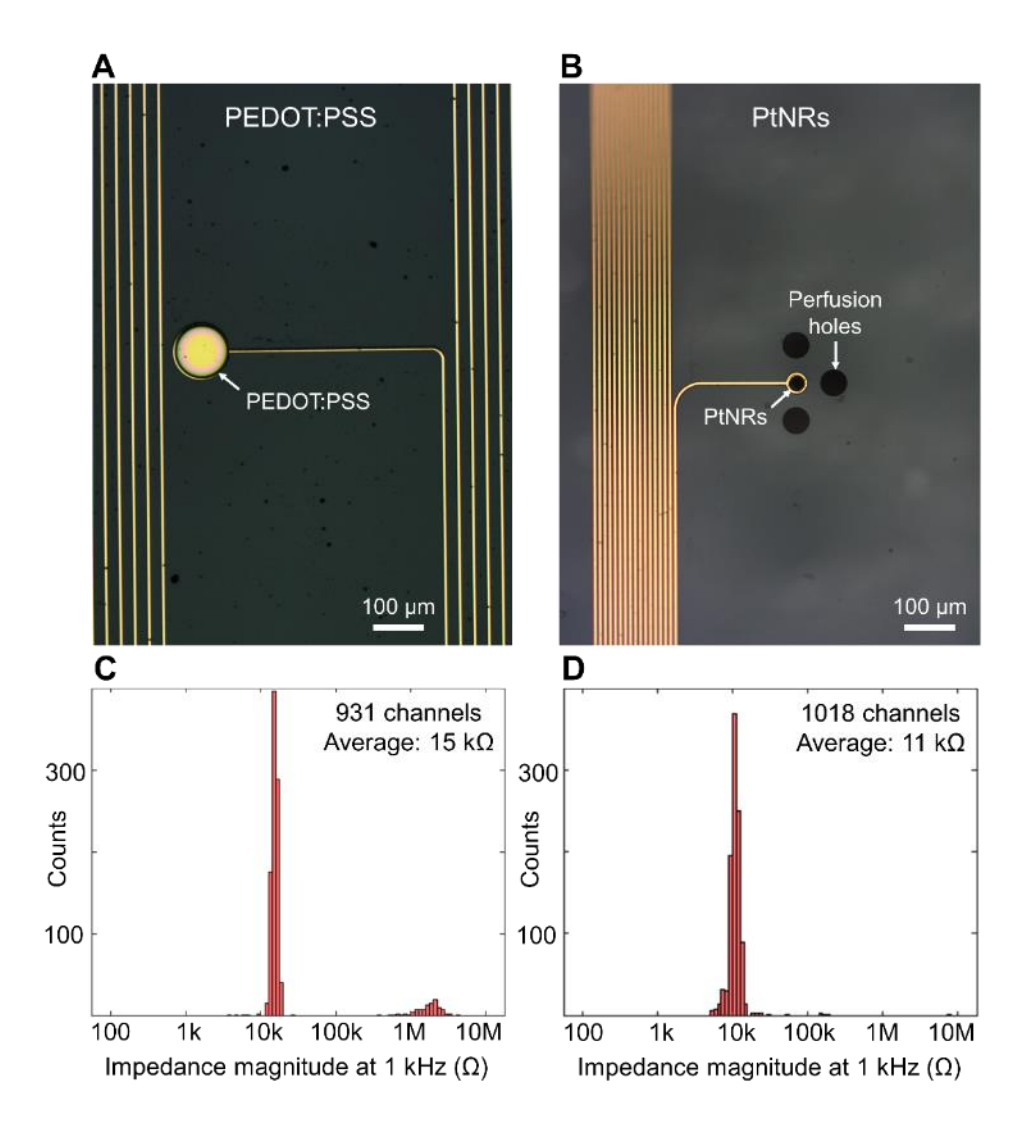


Figure S4. 1024 channels electrode with (A) 100 μ m diameter PEDOT:PSS as electrolytic interface in comparison with (B) 30 μ m diameter PtNRs. Histogram of impedance magnitude at 1kHz for (C) PEDOT:PSS (100 μ m diameter) and (D) PtNRs (30 μ m diameter).

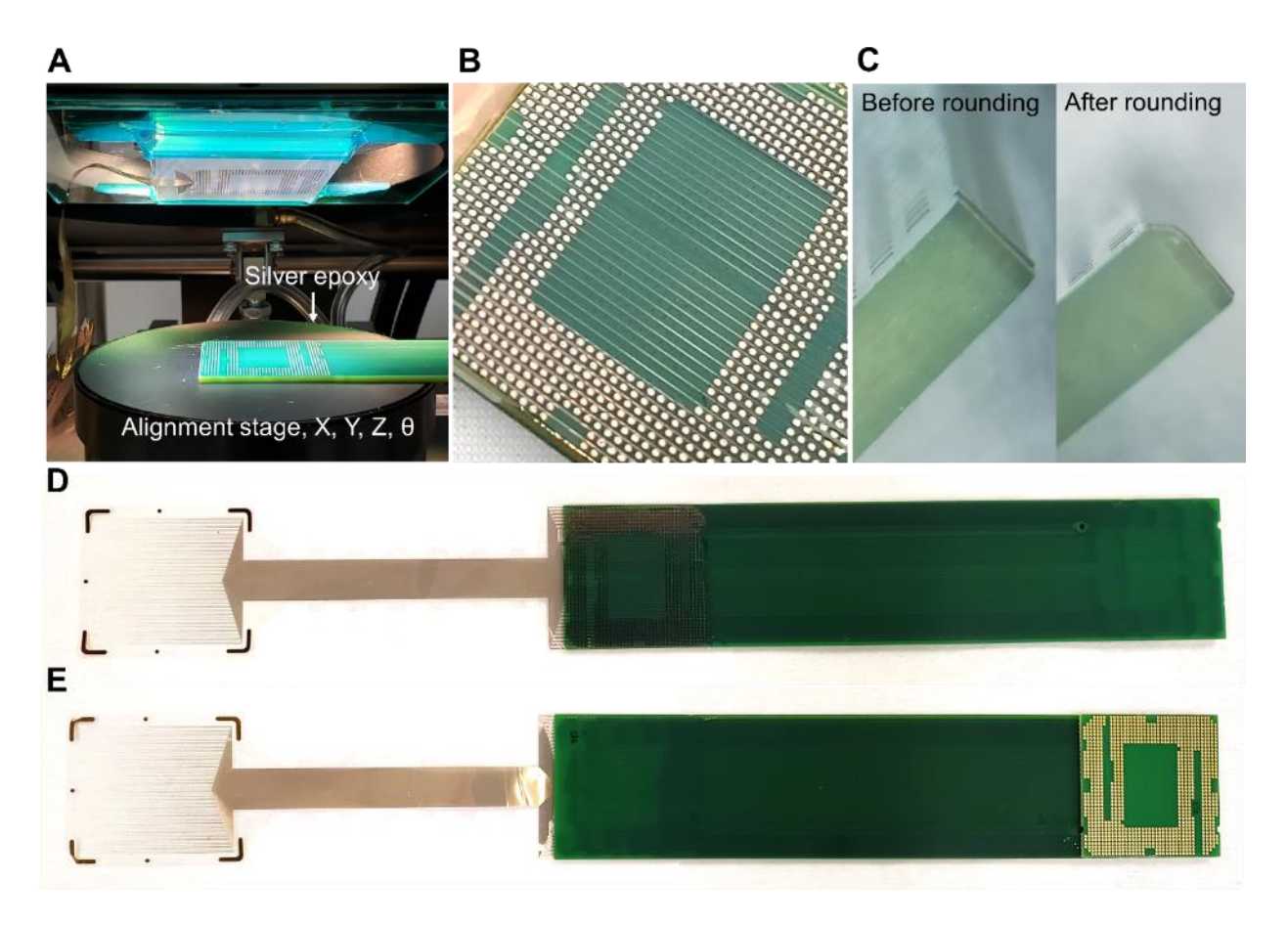


Figure S5. Bonding process of the flexible electrode on the rigid PCB. (A) Electrode and extender board placed on the alignment state. Silver epoxy bumps are deposited on the pads of the PCB side. (B) The bonding interface between the parylene C electrode and the PCB after curing the silver epoxy. (C) The PCB edge rounded to minimize potential damage of the metal leads during handling. Photos of the flexible electrode bonded on the PCB with PtNRs facing (D) downward and (E) upward.



Figure S6. 1024 channels amplifier board populated with LGA1155 connector and Intan RHD2164 chips. 8 SPI cables connect the amplifier board to the recording controller.

Figure S7. A simplified circuit model detailing the parasitic capacitances present in the high-density thin-film interconnects on PtNRGrids.

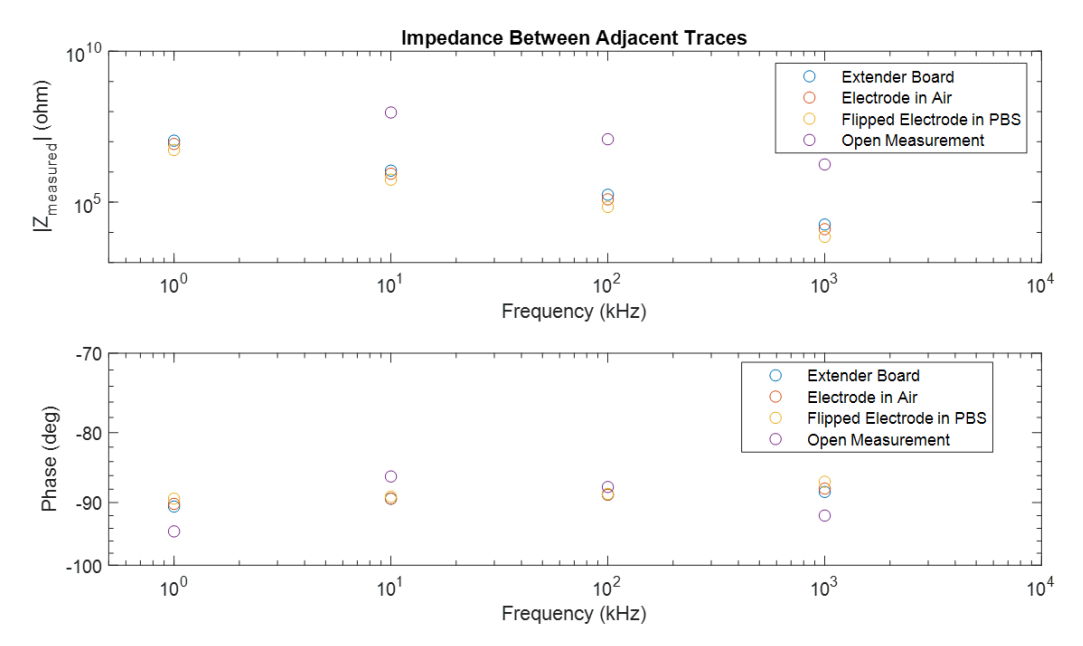


Figure S8. Magnitude and phase plots of the complex impedance between two adjacent channels in various measurement configurations showing capacitive characteristics. A system open measurement is shown as a reference. Values for co-planar capacitance, Cp, and parallel-plate capacitance, Cs, were extracted from the above measurements and used to generate bode plots for crosstalk (see Fig. S11).

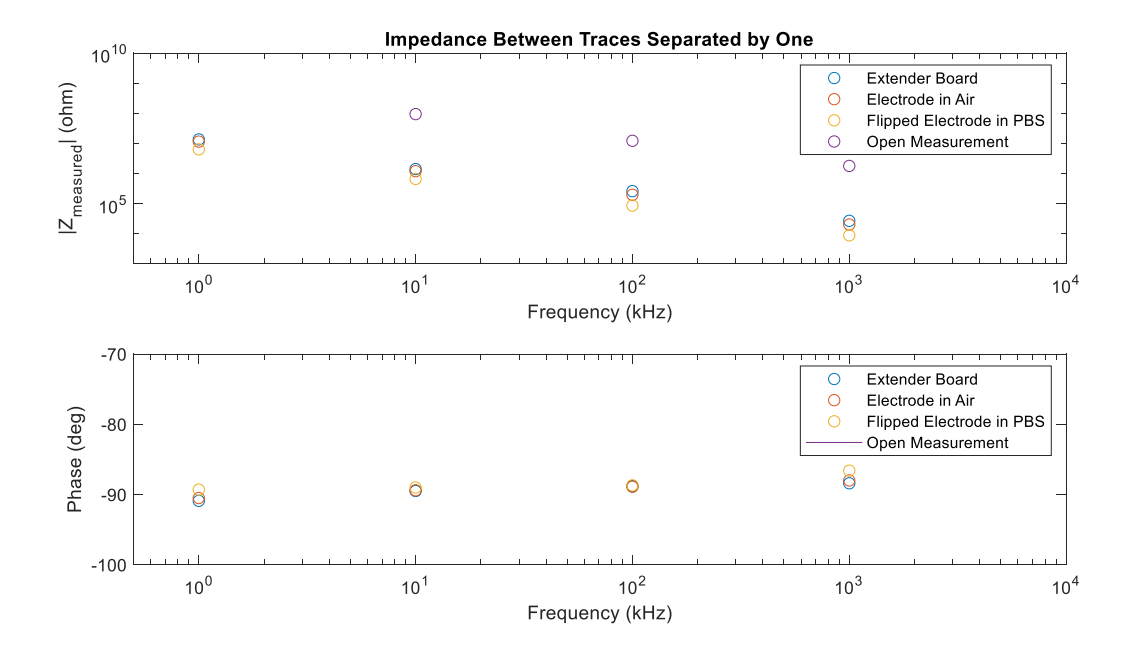


Figure S9. Magnitude and phase plots of the complex impedance between two channels separated by one (there is one channel between each channel) in various measurement configurations showing capacitive characteristics. A system open measurement is shown as a reference.

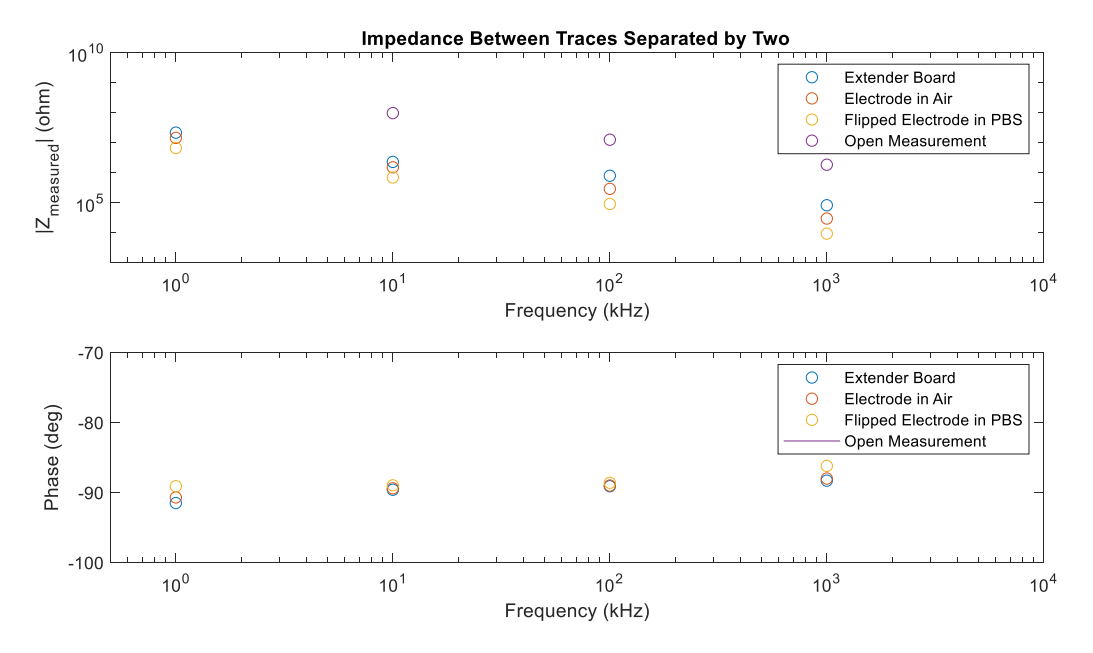


Figure S10. Magnitude and phase plots of the complex impedance between two channels separated by two in various measurement configurations showing capacitive characteristics. A system open measurement is shown as a reference.

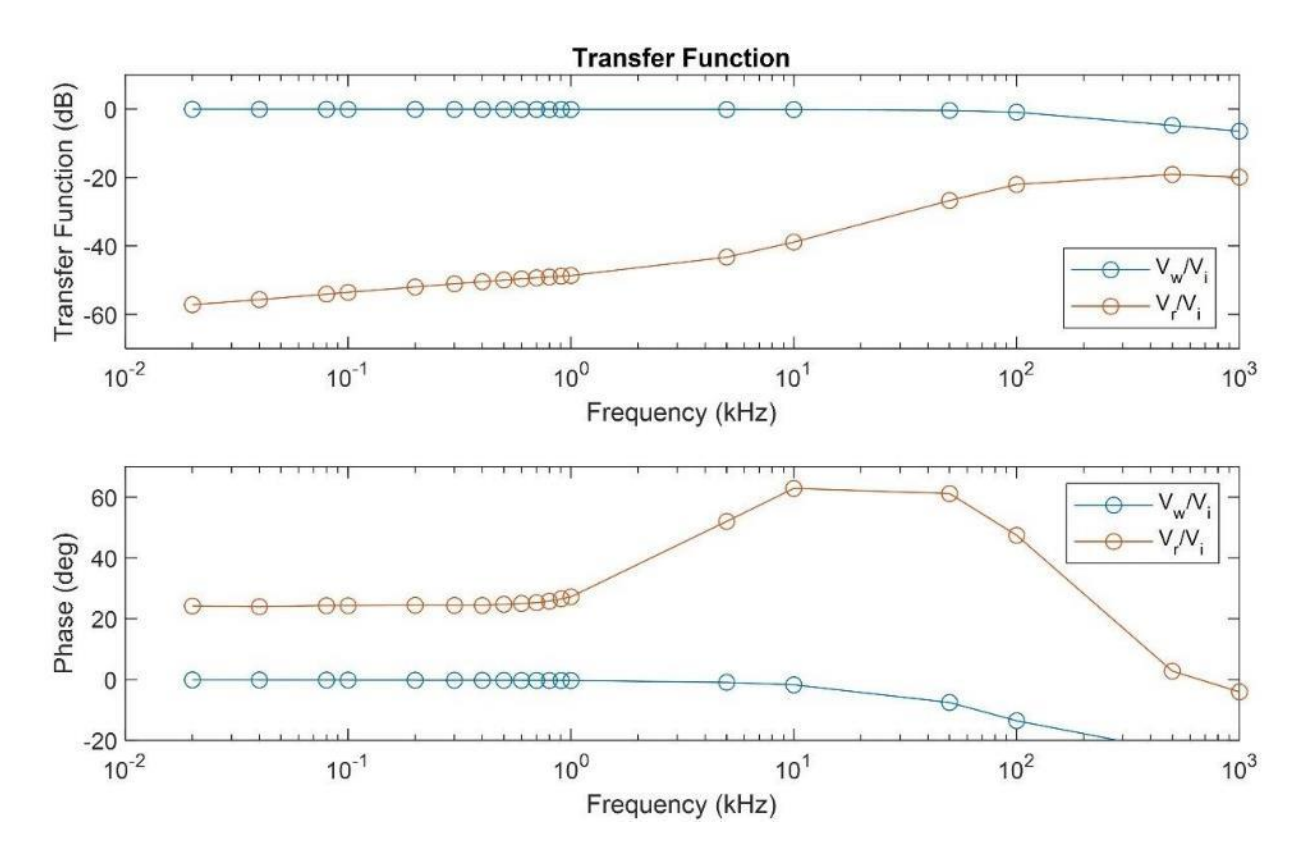


Figure S11. Transfer functions between input and output for a working channel and nearest neighboring channel. Note that the signal bandwidth of interest for neural signals is typically below 1 kHz, thus we can say that the PtNR microelectrodes introduce negligible signal attenuation in the signal path. Additionally, we see that neighboring channels will have near - 60 dB crosstalk isolation at signals of interest. For a 500 μ V amplitude signal, this corresponds to a 0.5 μ V amplitude signal which is below the noise floor of the Intan acquisition system.

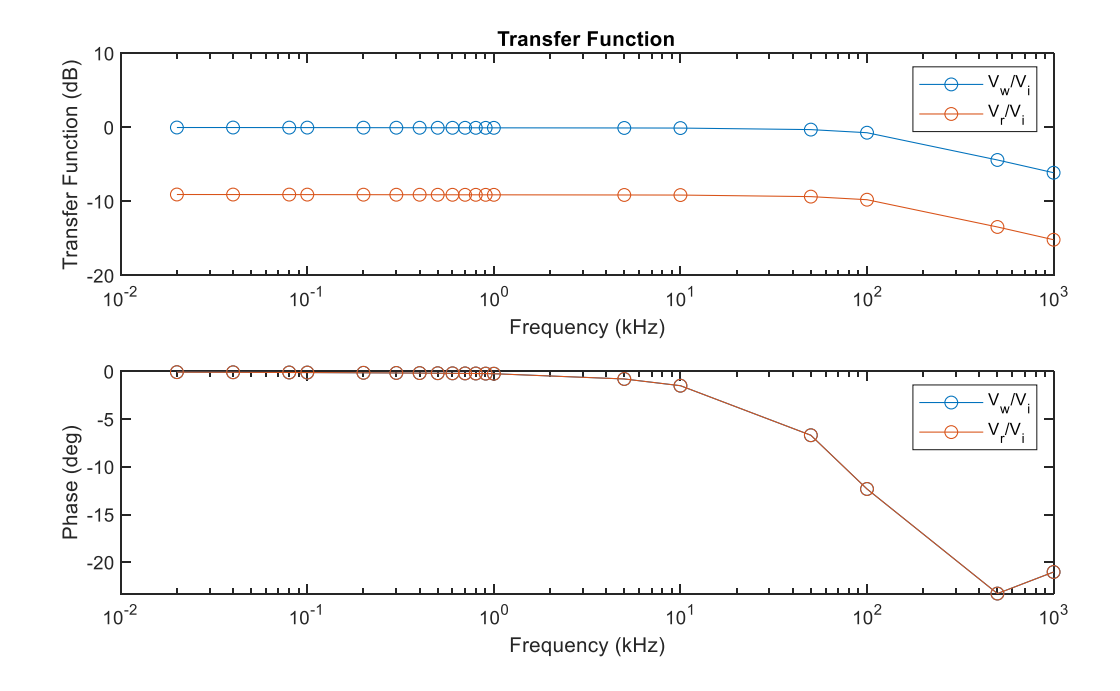


Figure S12. Bode plots showing the transfer functions between 1. an ideal voltage source, Vi, and the working channel intended to measure said voltage, and 2. An ideal voltage source, Vi,

and the adjacent channel which has been electrically disconnected from the electrolytic solution or tissue (denoted Vr). Note that when an adjacent channel is disconnected, the only path for leakage current to flow is through its respective amplifier input impedance. Thus, we see significantly larger crosstalk in the open-channel configuration.

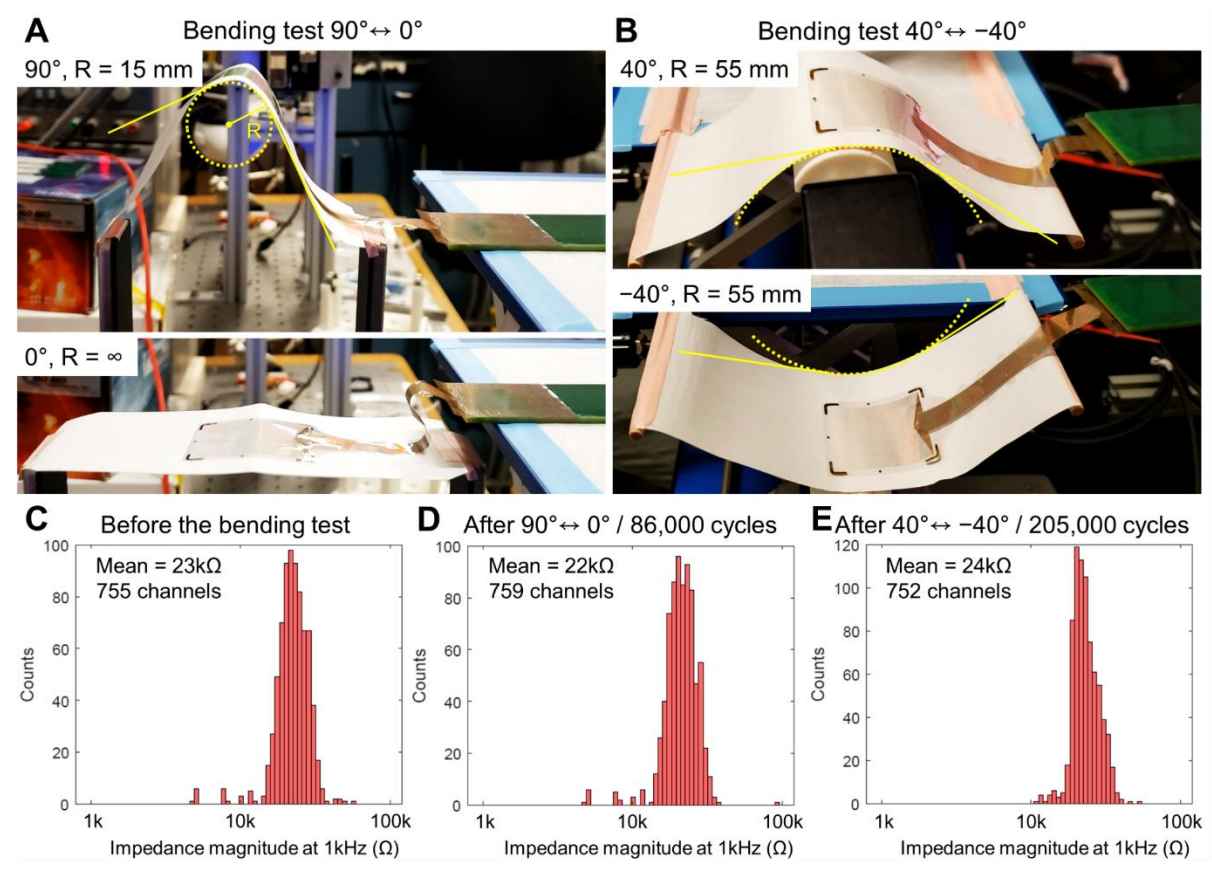


Figure S13. Bending cycles test. Photo of (A) $90^{\circ} \leftrightarrow 0^{\circ}$ and (B) $40^{\circ} \leftrightarrow -40^{\circ}$ bending tests. Impedance histogram of the electrode (C) before, (D) after 86,000 cycles of $90^{\circ} \leftrightarrow 0^{\circ}$ bending, and (E) after 205,000 cycles of $40^{\circ} \leftrightarrow -40^{\circ}$ bending.

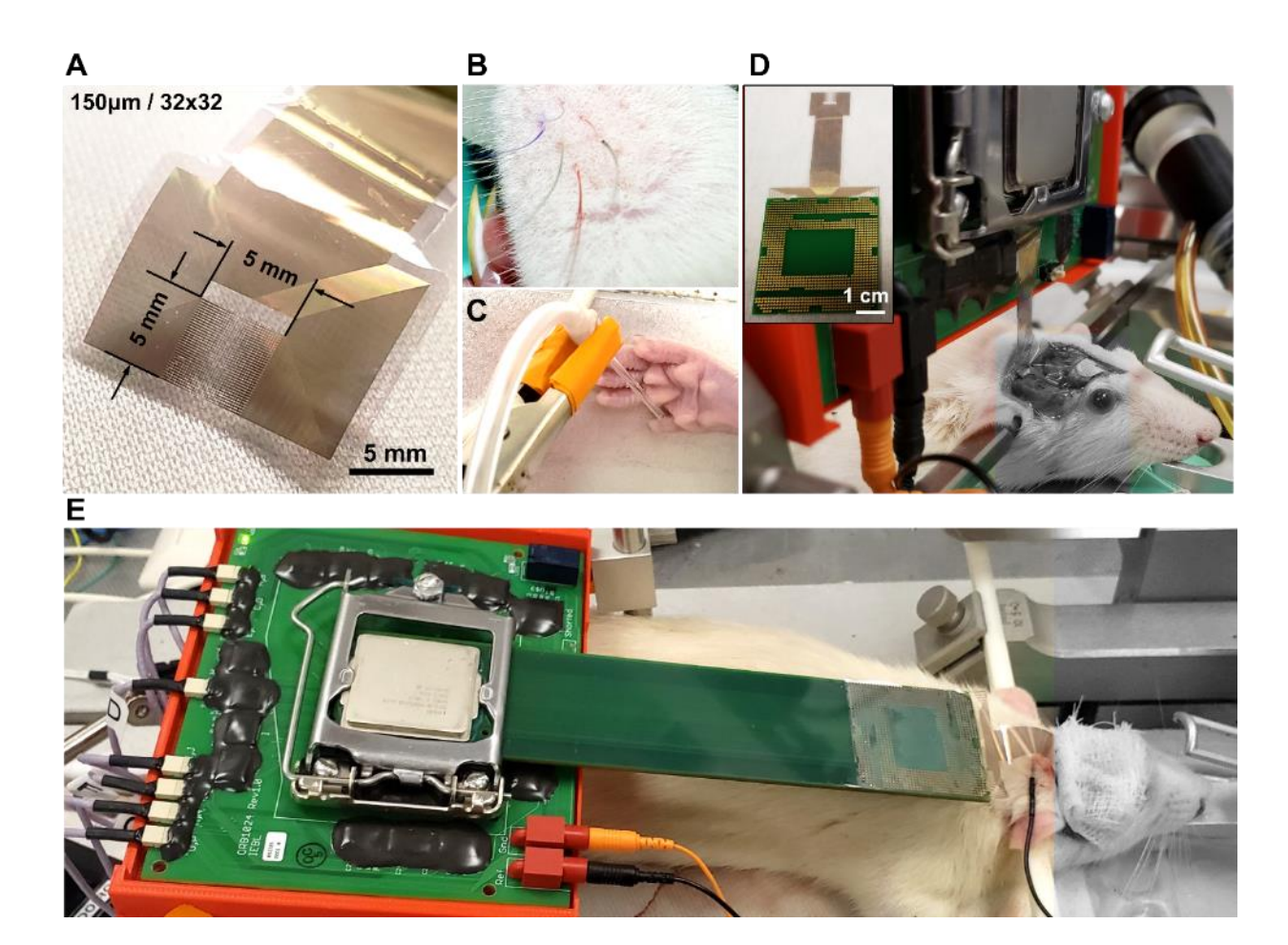


Figure S14. Rat whisker barrel recording experimental setup. (A) Magnified photo of the rat electrode near the recording sites. (B) Individual whiskers colored and (C) hindlimb of the rat. Microcapillary tube shown in (C) is used for an air-puff stimulation. Rat barrel cortex recording with PtNRGrids bonded on (D) a small PCB and (E) extender board.

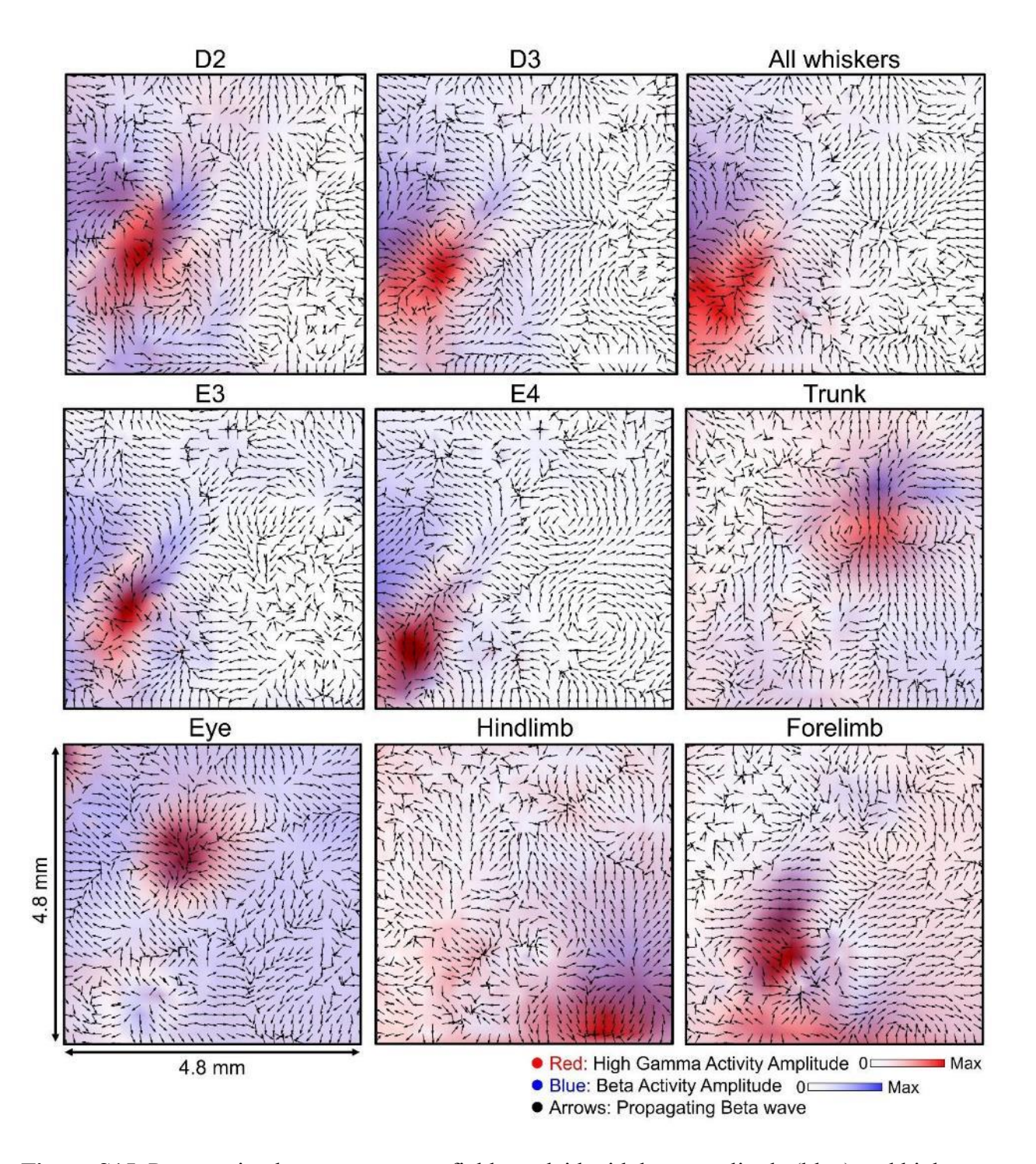


Figure S15. Propagating beta wave vector field overlaid with beta amplitude (blue) and high gamma amplitude (red) for (A) E4 whisker, (B) eye, and (C) trunk.

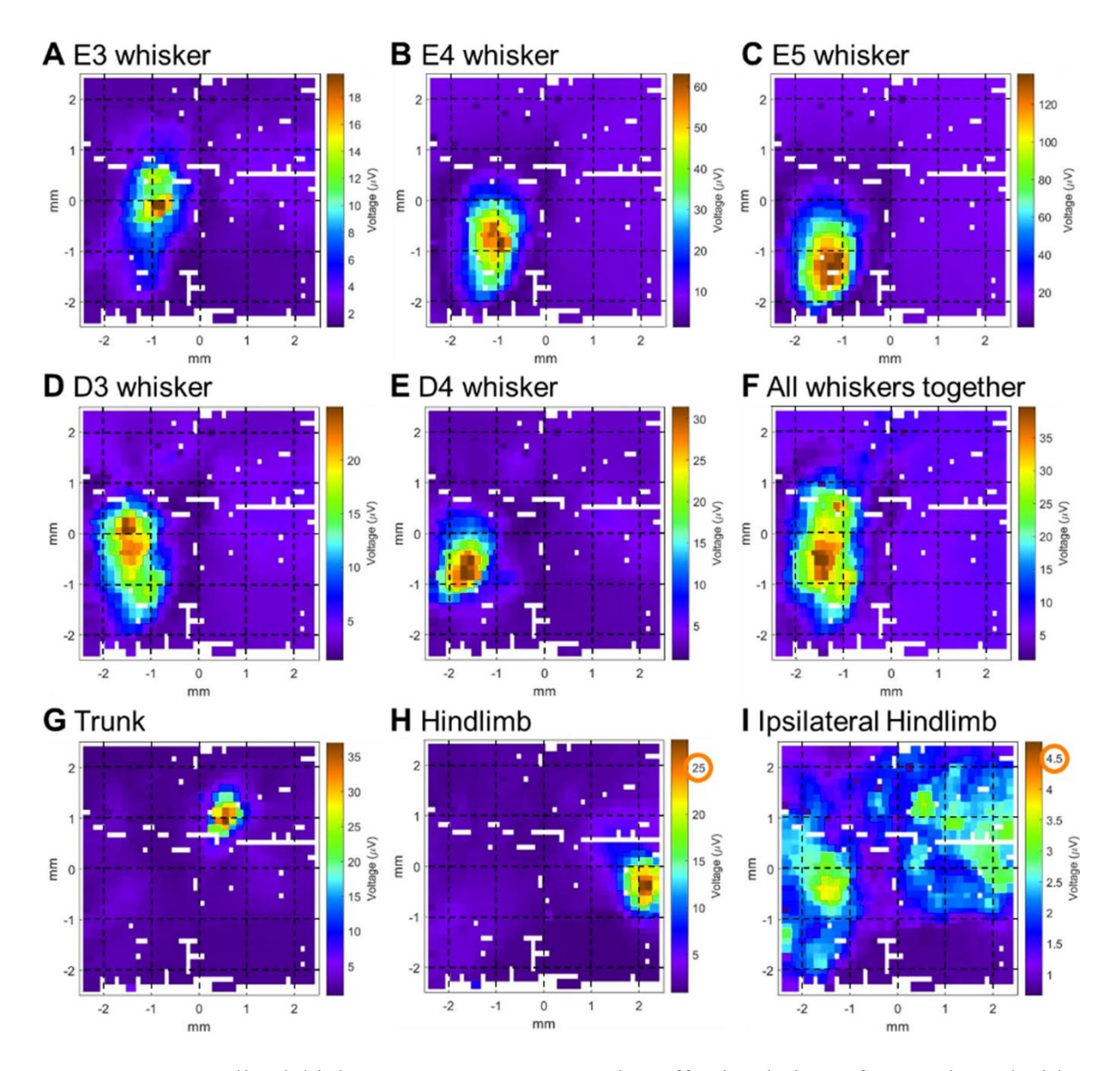


Figure S16. Localized high gamma response to air-puff stimulation of contralateral side $(A)\sim(E)$ individual whiskers, (F) all whiskers, (G) trunk, (H) hindlimb, and (I) ipsilateral side hindlimb.

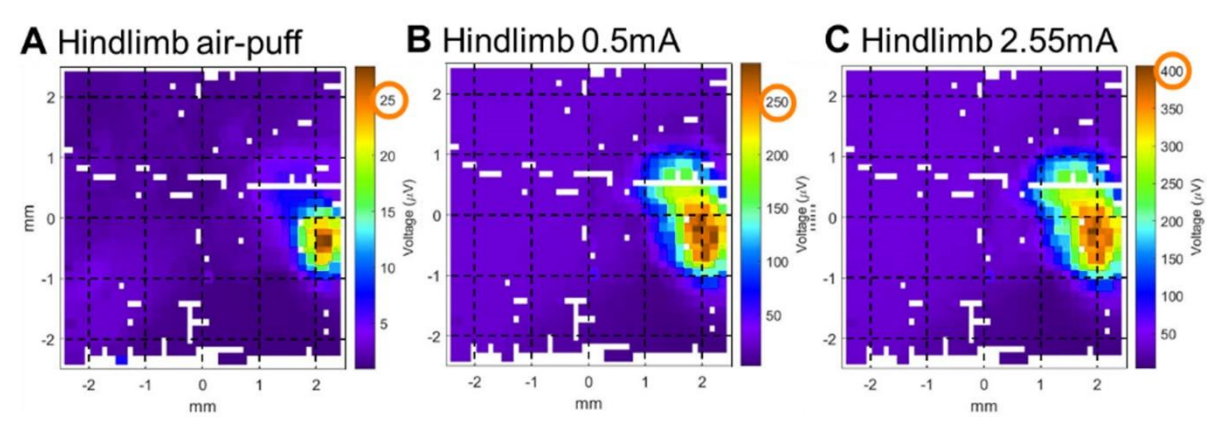


Figure S17. Comparison of (A) air-puff and (B)-(C) electrical stimulation of contralateral side hindlimb of the rat. Electrical stimulation of rat's hindlimb thigh muscles evoked broader and

more than 10 times larger amplitude response on the sensory cortex compared to that of hindlimb air-puff stimulation.

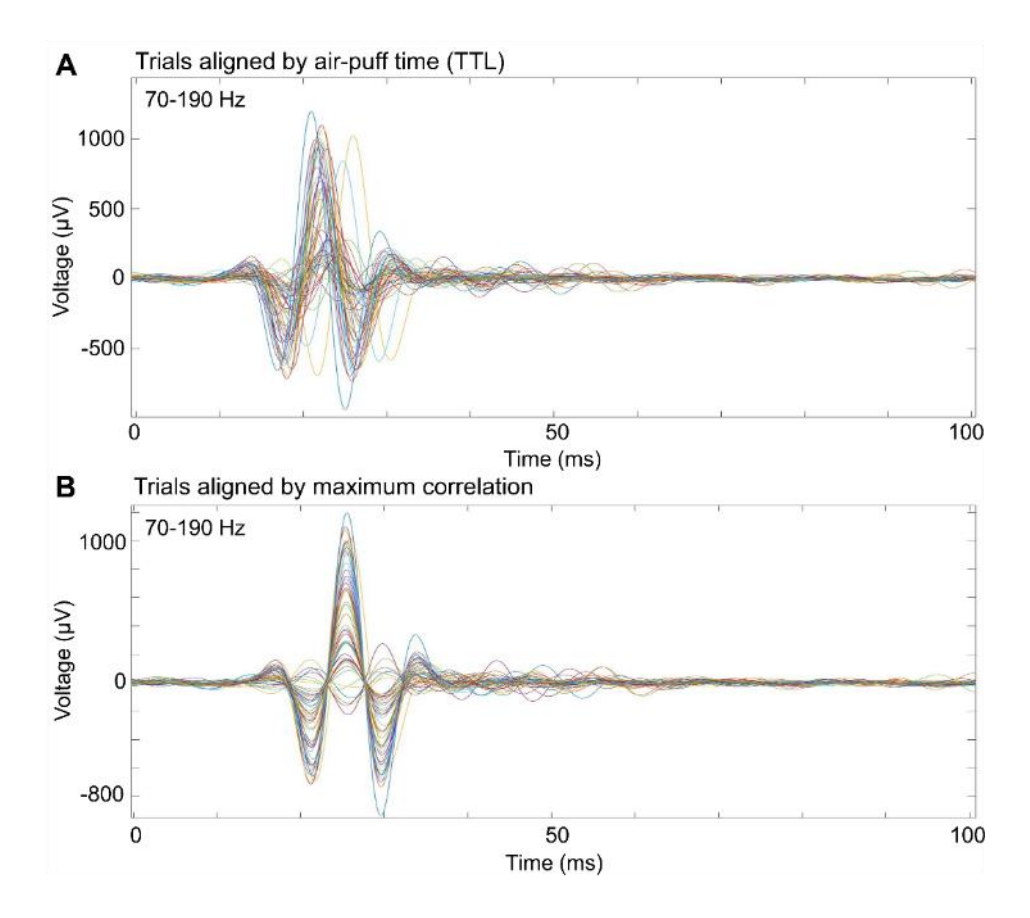


Figure S18. High gamma activity aligned by (A) air-puff stimulation time and (B) maximum correlation of the responses.

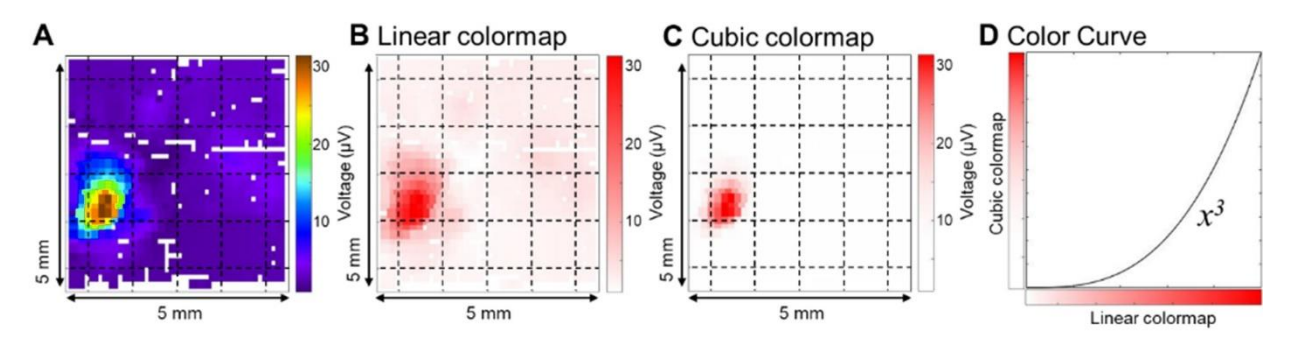


Figure S19. Localized HGA under different colormaps. (A) Purple-green-orange color map, (B) linear color map, (C) cubic color map. Cubic colormap was used to overlay high gamma responses to different whiskers. (D) Color curve used to generate cubic colormap.

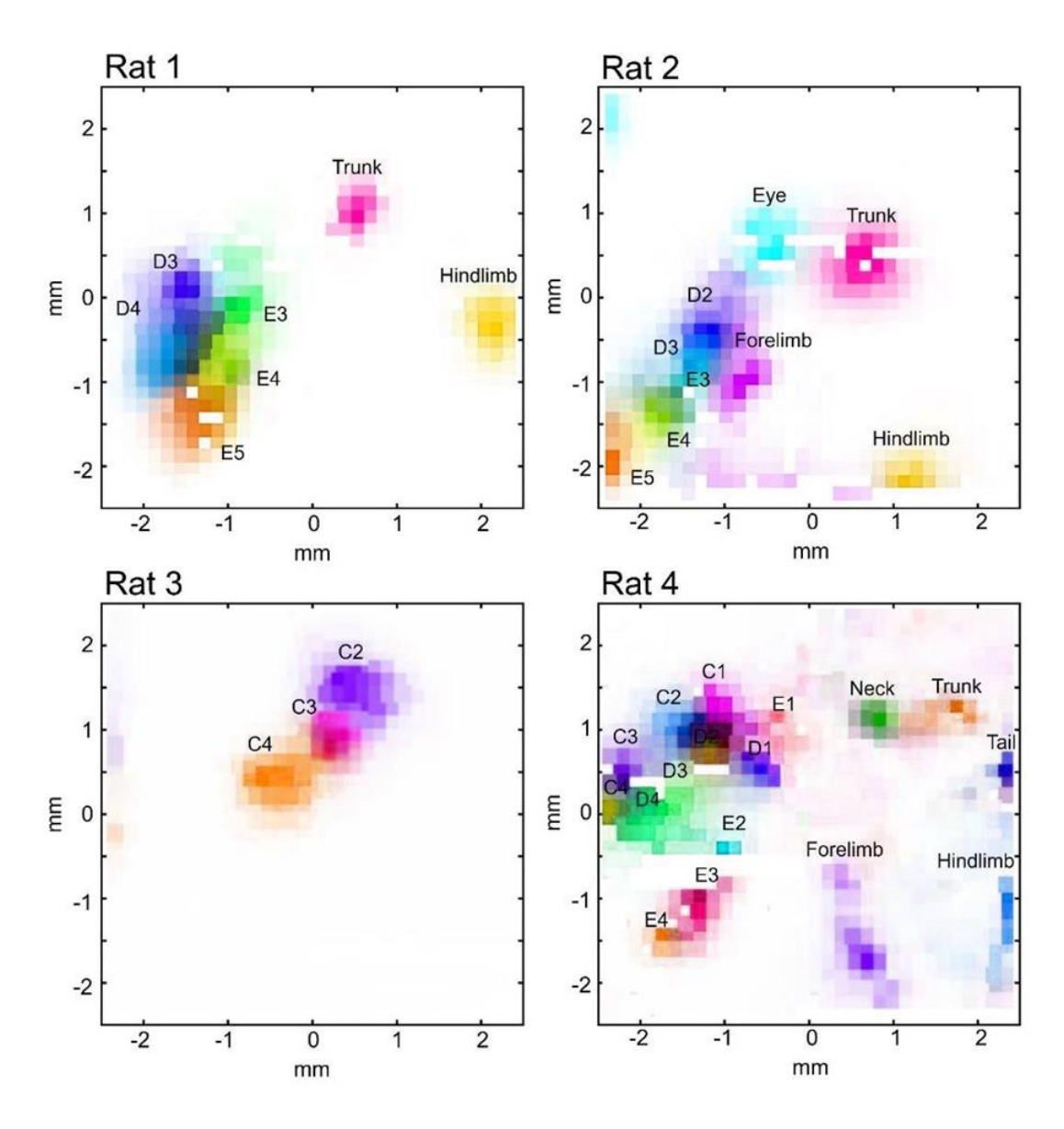


Figure S20. Localized HGA evoked by different whiskers or limbs stimulation for four different rats.

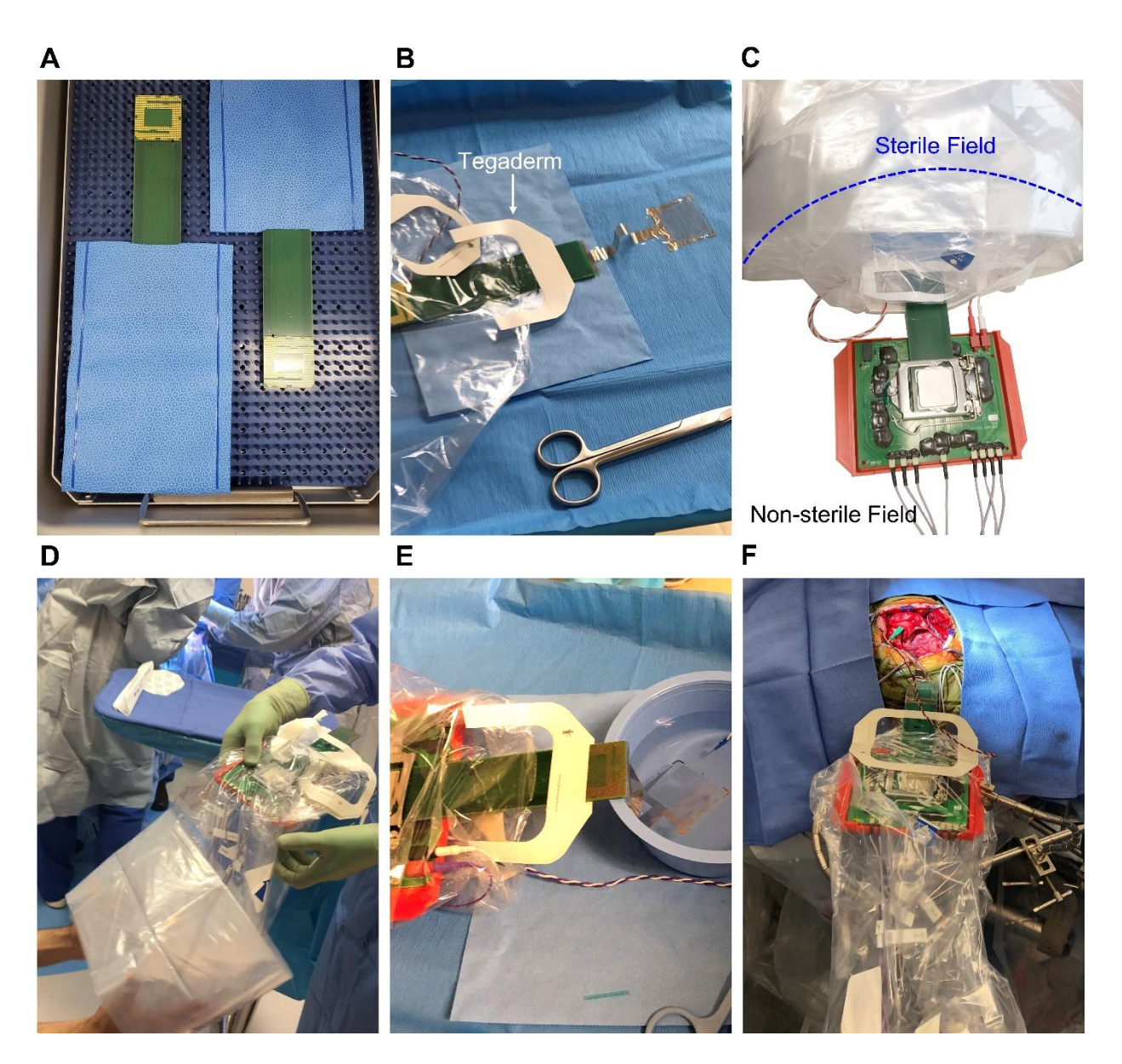


Figure S21. Sterilization and sterile procedures in the operating room. (A) Electrode packaged in DuraHolder pouch placed inside the sterilization tray with silicone mat. (B) Extender board's connector region placed inside the SituateTM Sterile Drape. TegadermTM films were applied for waterproof, sterile barrier. (C) Establishing a connection in a non-sterile zone. (D) Sterile person holding the PtNRGrid and the amplifier board, and non-sterile person pulling the sterile drape from the inner surface. (E) Electrode impedance measurement in saline prior to implantation. (F) Implantation on the patient's brain. Greenberg® Retractors are holding the amplifier board.

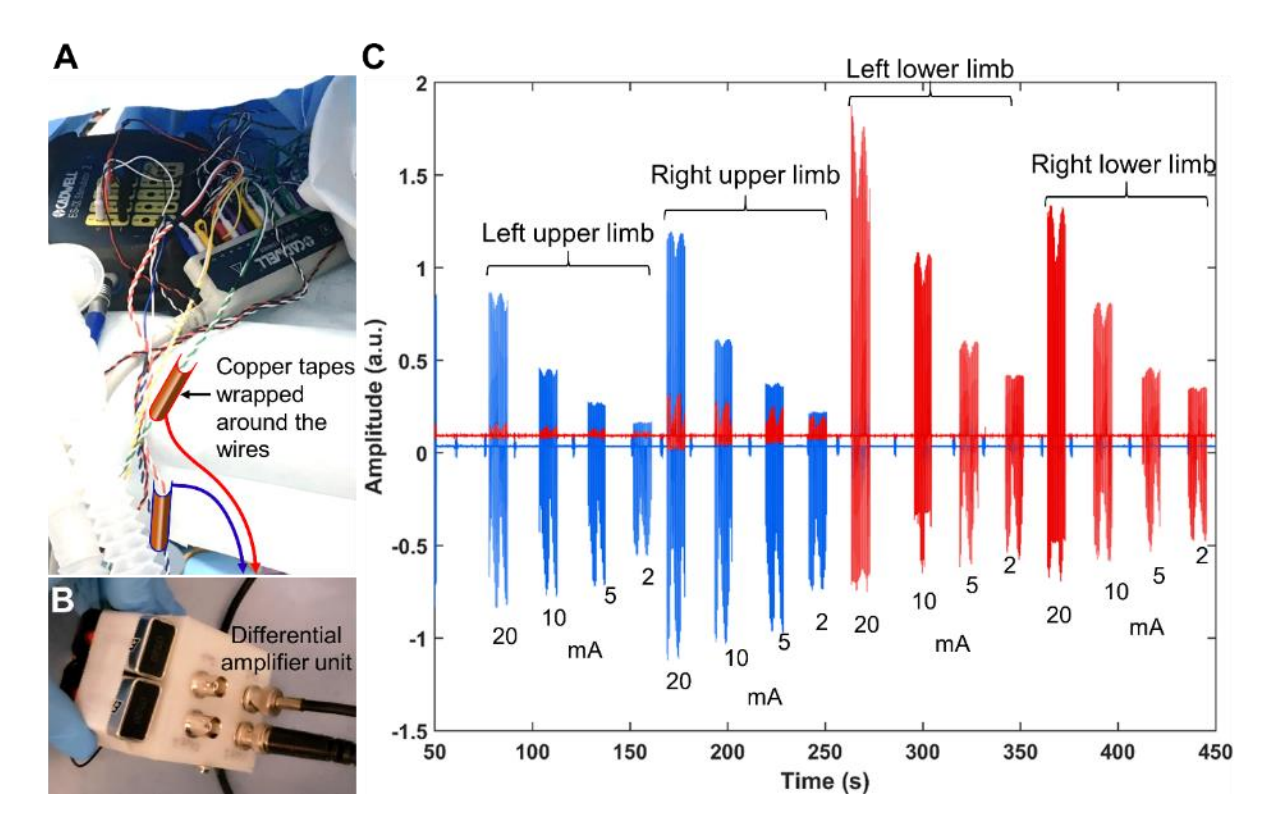


Figure S22. Electrical stimulation signal capture system. (A) Photo of the clinical stimulation controller and the schematics showing how the copper foils were wrapped around the wires. (B) Differential amplifier. (C) Signals captured with this system.

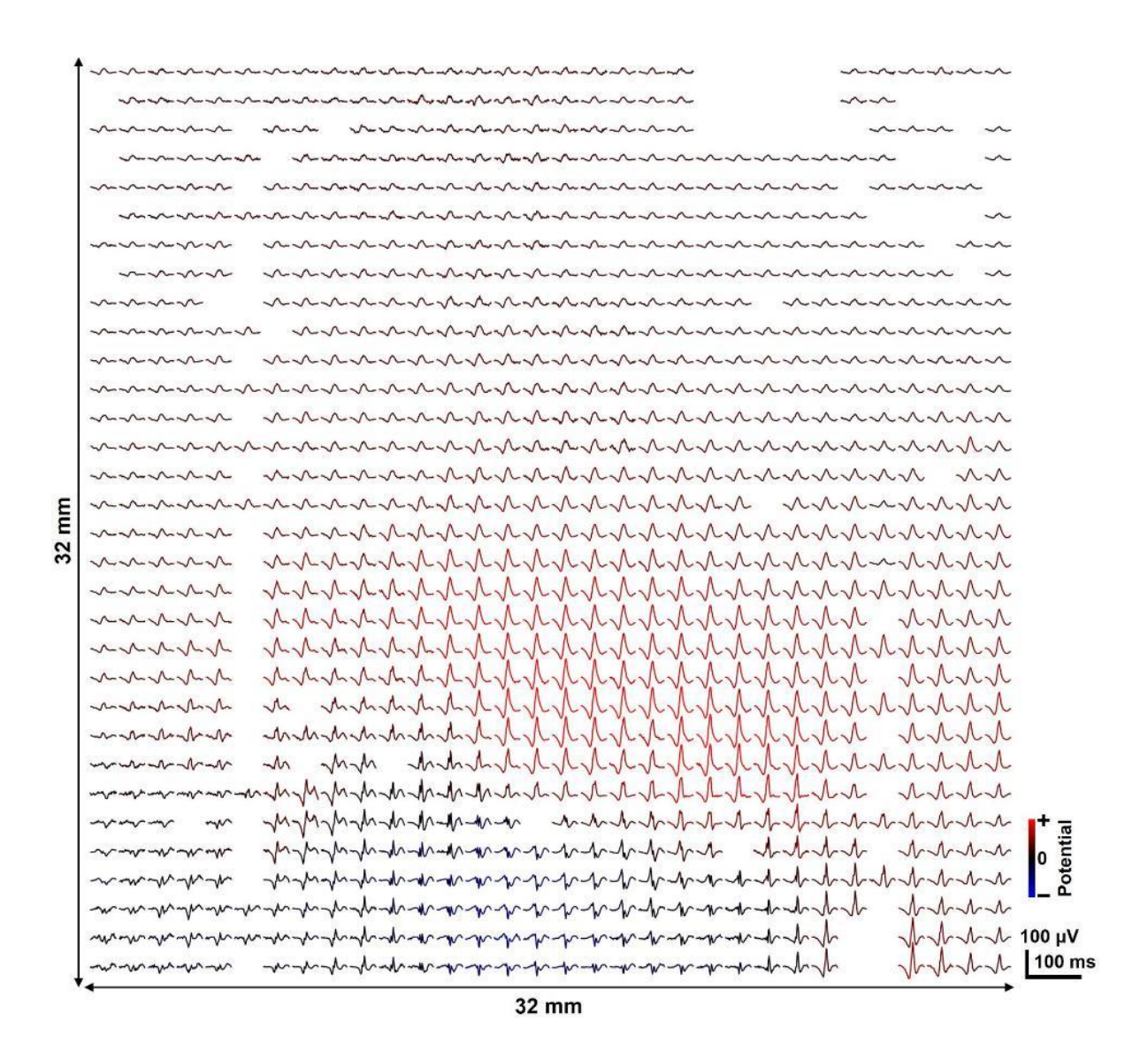


Figure S23. SSEP waveforms recorded with PtNRGrids implanted near the hand region. The waveforms are colored according to the polarity of the potential at 28ms post stimulus.

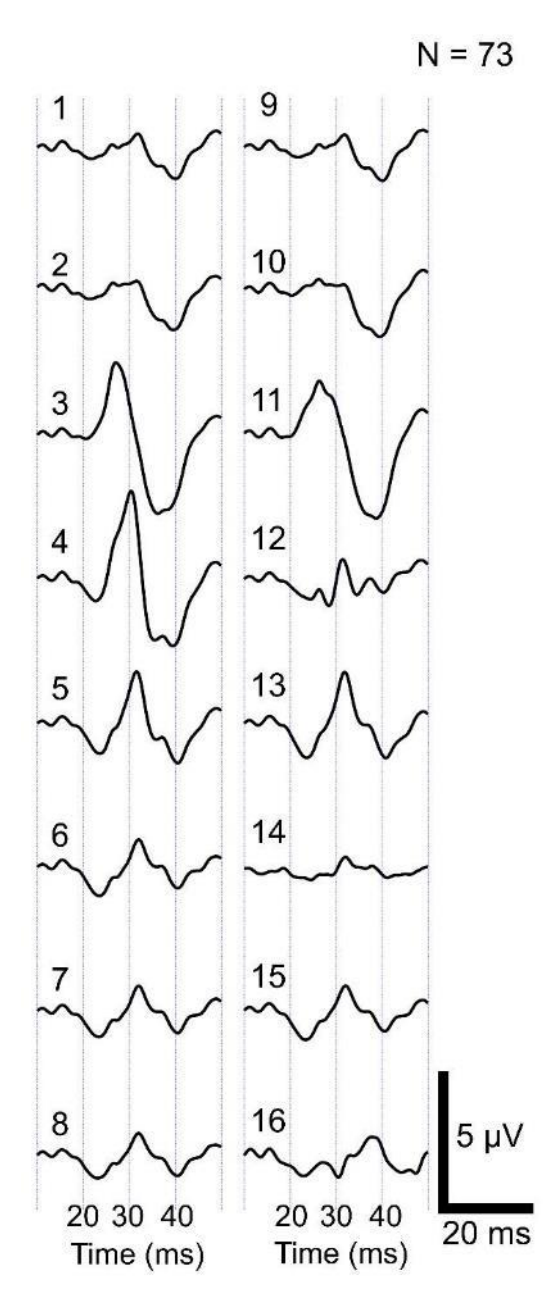


Figure S24. Waveforms of the SSEPs recorded with conventional dual column 2×8 , 16 channels clinical grid implanted near the hand region.

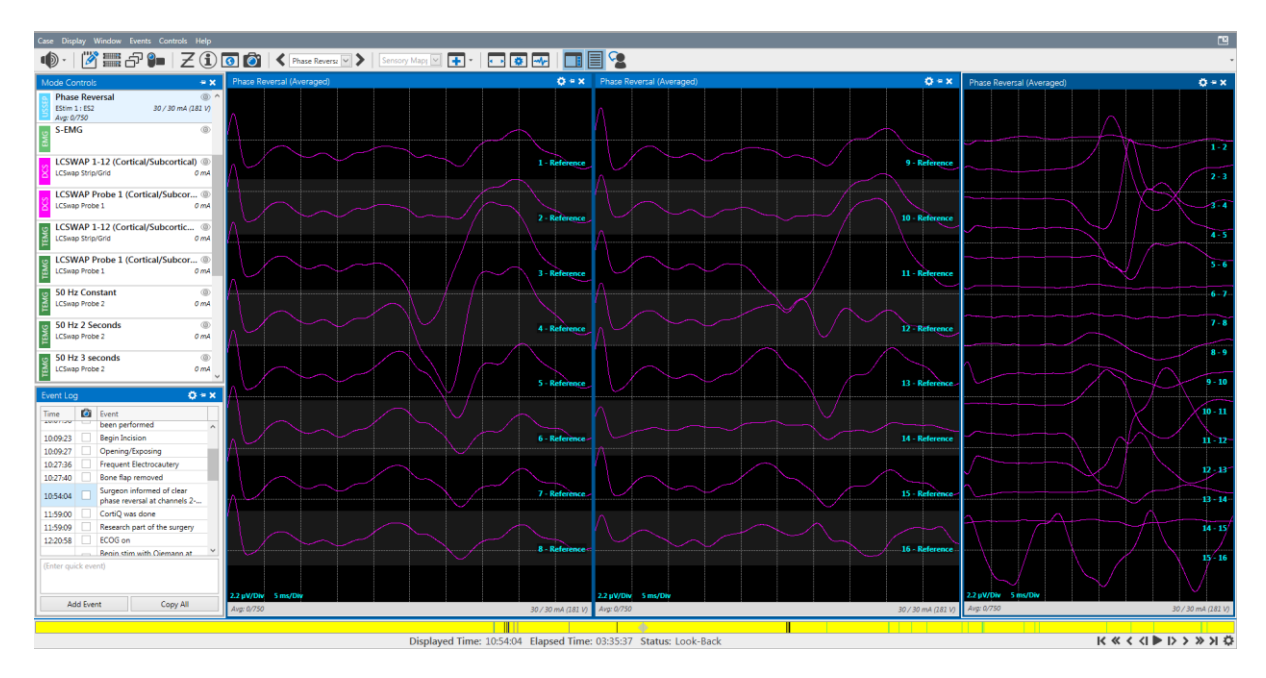


Figure S25. Snapshot of the neuromonitoring software showing trial-averaged phase reversal waveforms measured with the 2×8 clinical ECoG grid.

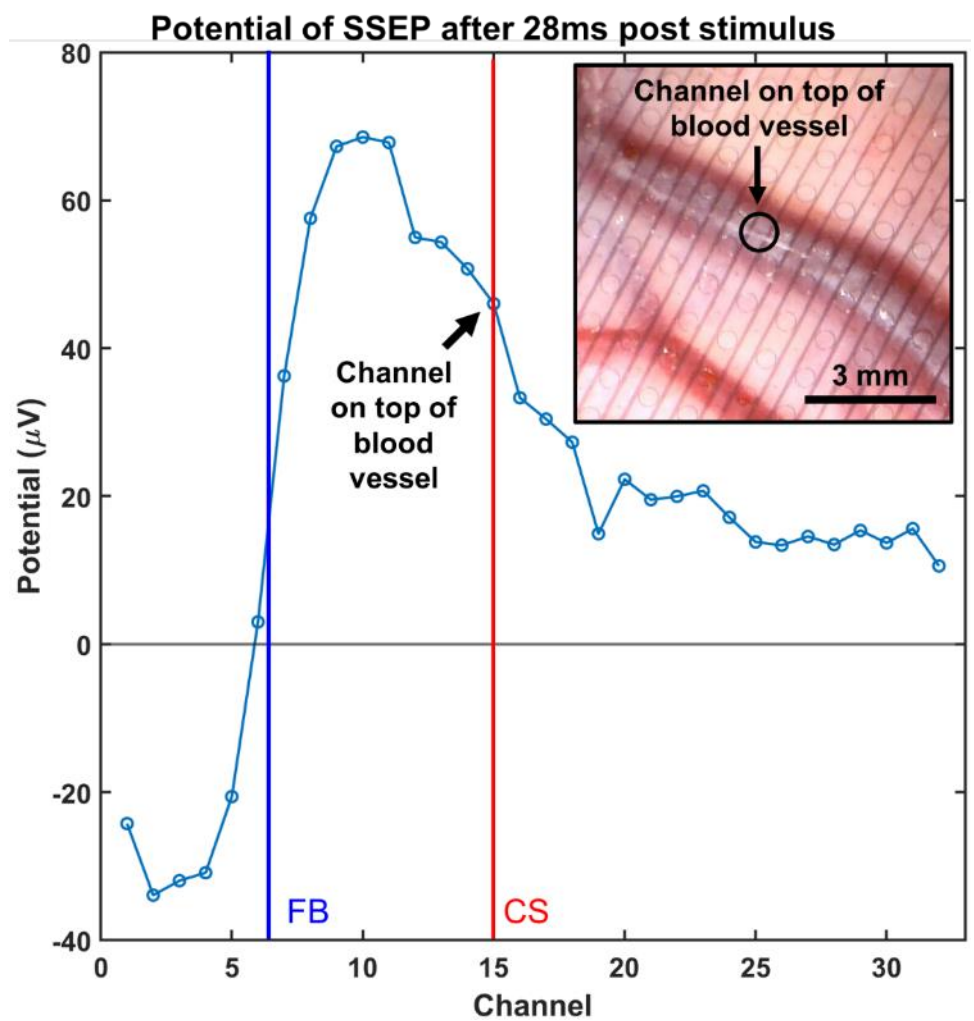


Figure S26. Potential of SSEP after 28 ms post stimulus. Inset figure indicates the channel placed on top of the blood vessel.

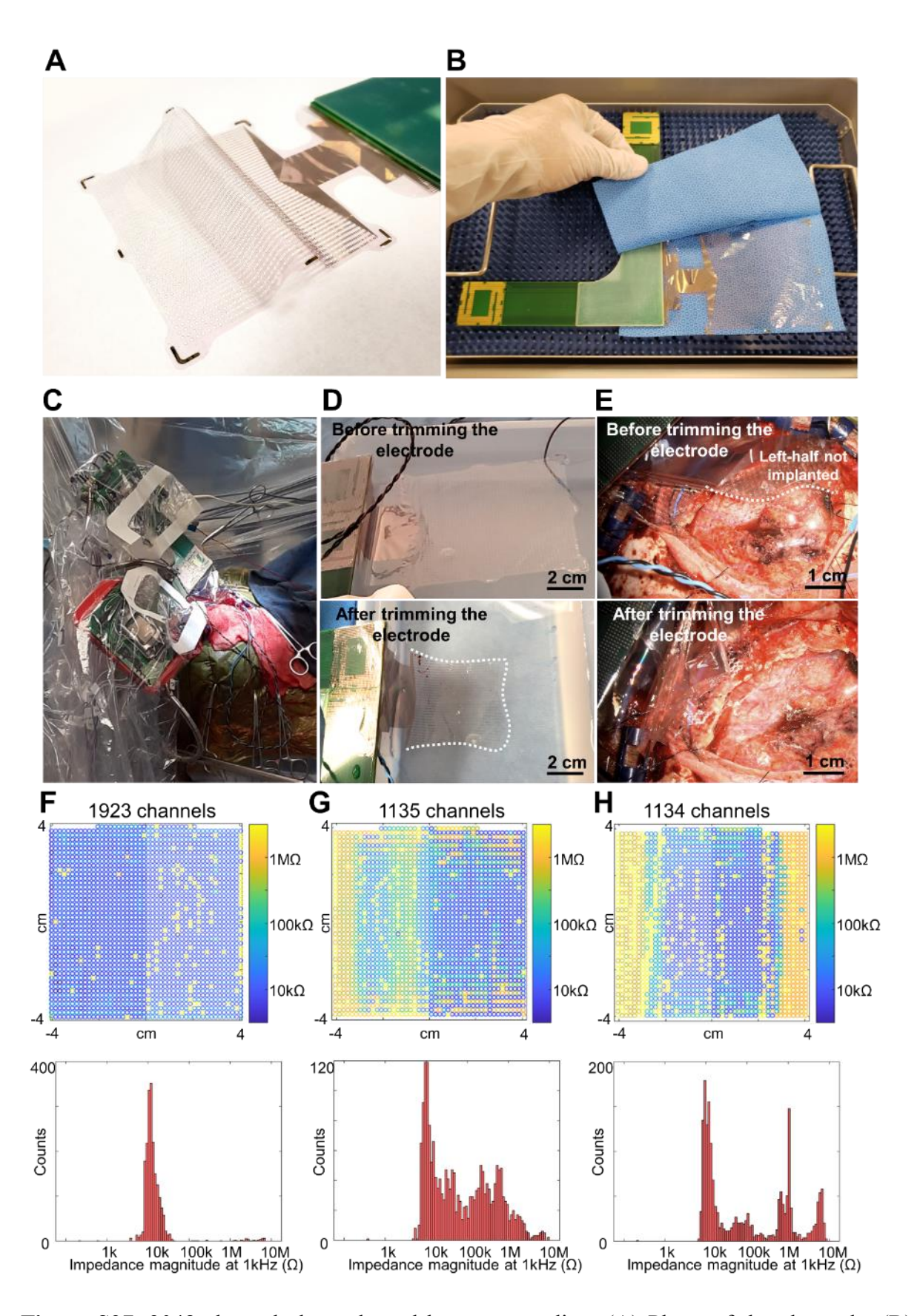


Figure S27. 2048 channel electrode and human recording. (A) Photo of the electrode. (B) Sterilization set up with DuraHolder pouch. Two extender boards are joined by implantable-grade autoclavable glue. (C) Intraoperative recording set up with two amplifier boards wrapped

with sterile drapes and clamped with Greenberg retractors. (D) Electrode before and after trimming. (E) Electrode implanted on the patient's brain before and after trimming. 1 kHz impedance mapping of the electrode (F) in saline after the sterilization, (G) on patient's brain with only the right half implanted, and (H) on patient's brain after trimming the electrode. The 1 kHz impedance histograms show all 2048 channels measured by the recording controller including the channels that were not placed on the cortex or trimmed out.

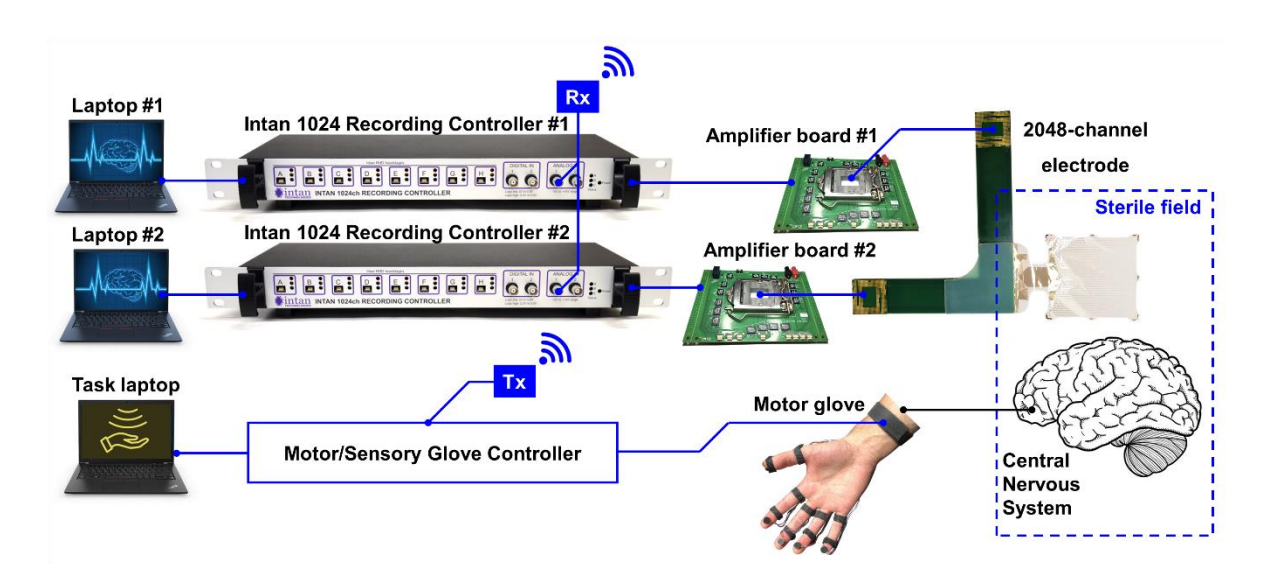


Figure S28. 2048-channel recording system connection diagram. Rx and Tx indicates Zigbee wireless receiver and transmitter, respectively.

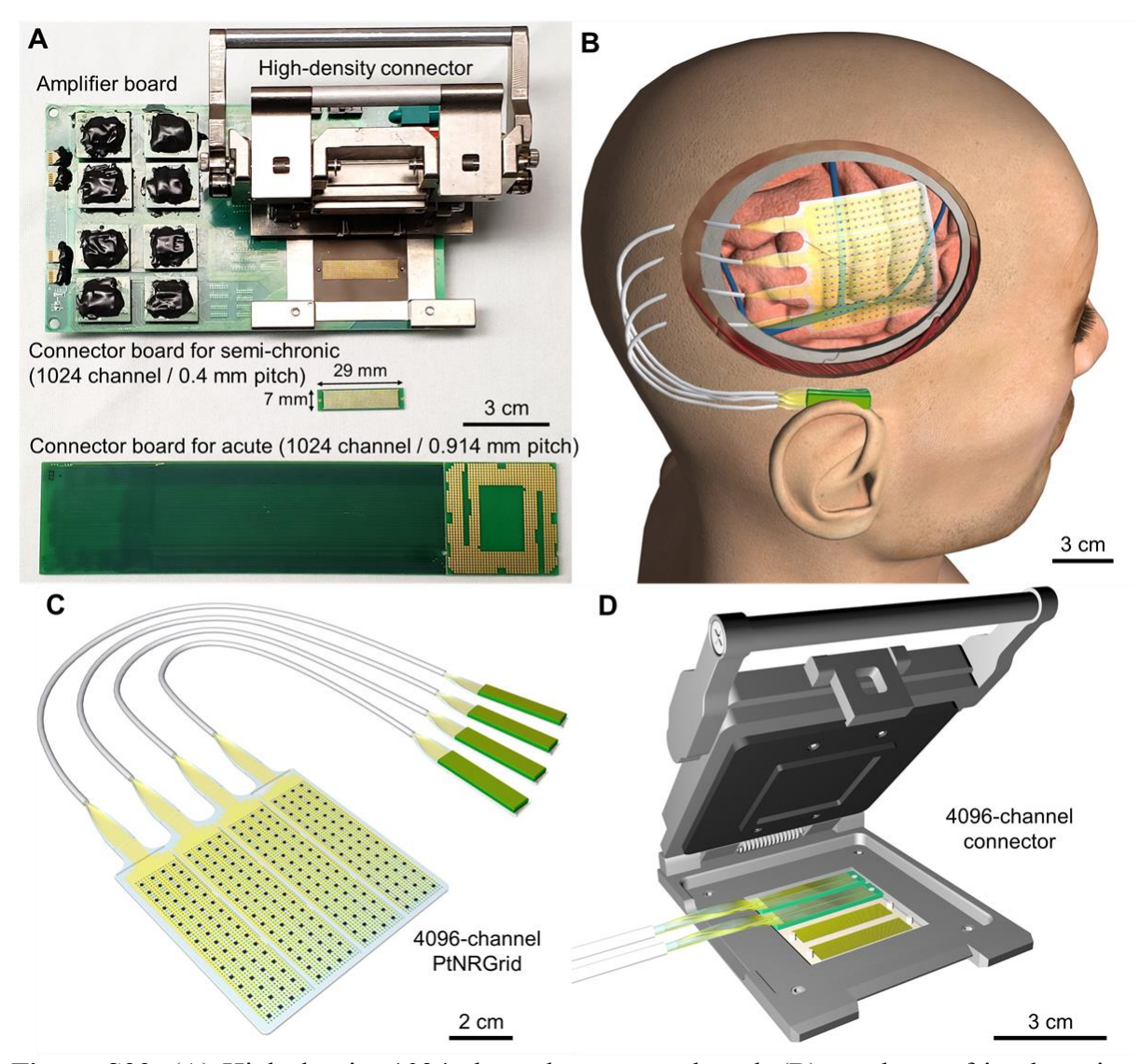


Figure S29. (A) High density 1024 channel connector board, (B) mock-up of implantation strategy of the 4096-channel grid in a semi-chronic setting with tunneled wires through the scalp (C) electrode and (D) connector placement in the specially designed socket.

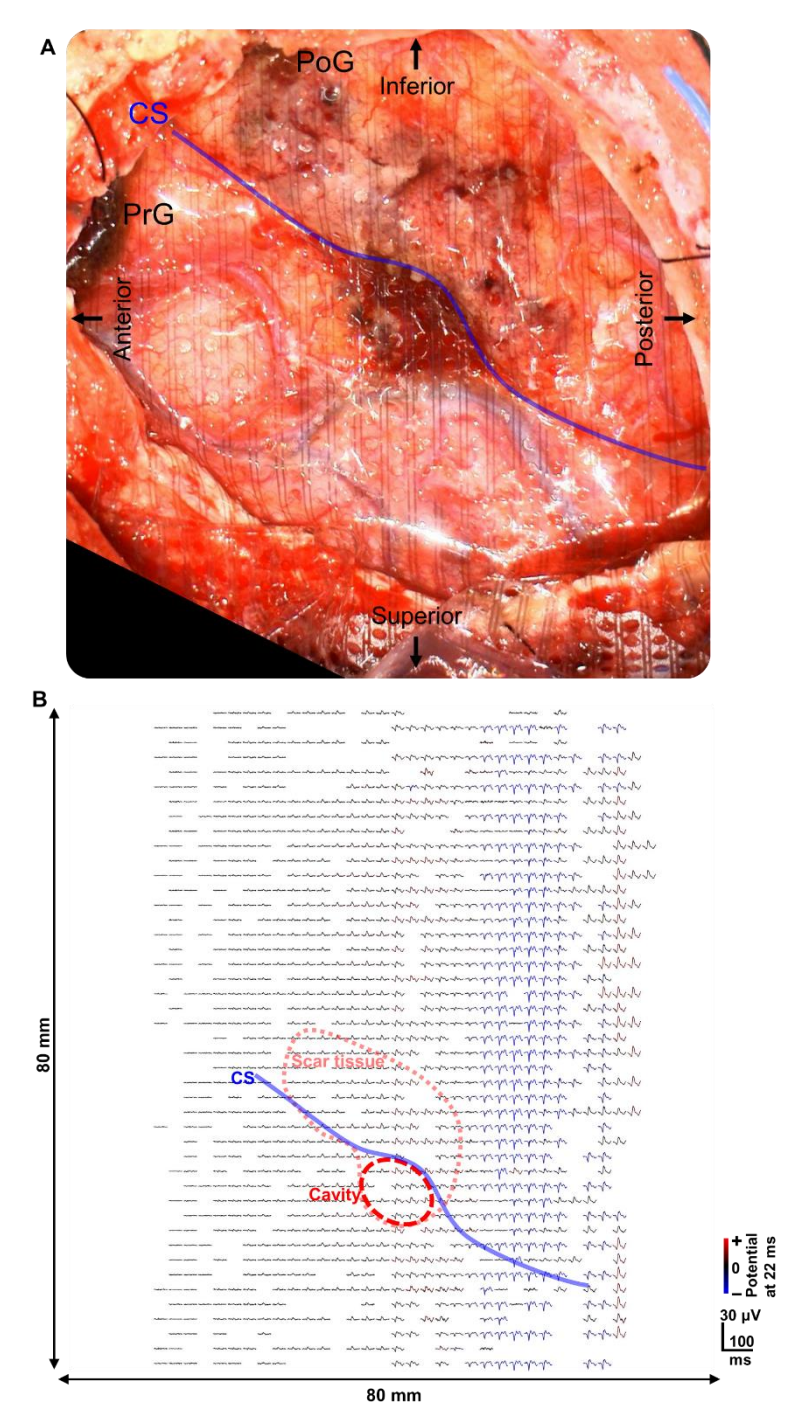


Figure S30. Human brain SSEP recording with 2048 channel PtNRGrid. (A) Electrode placement on return surgery patient with scar tissues and cavity from previous resective surgery. (B) Spatial mapping of SSEP waveforms recorded from 2048 channel PtNRGrid.

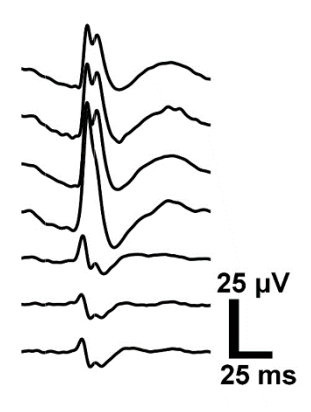


Figure S31. Phase reversal SSEPs recorded by 1024 channels PEDOT:PSS electrodes.

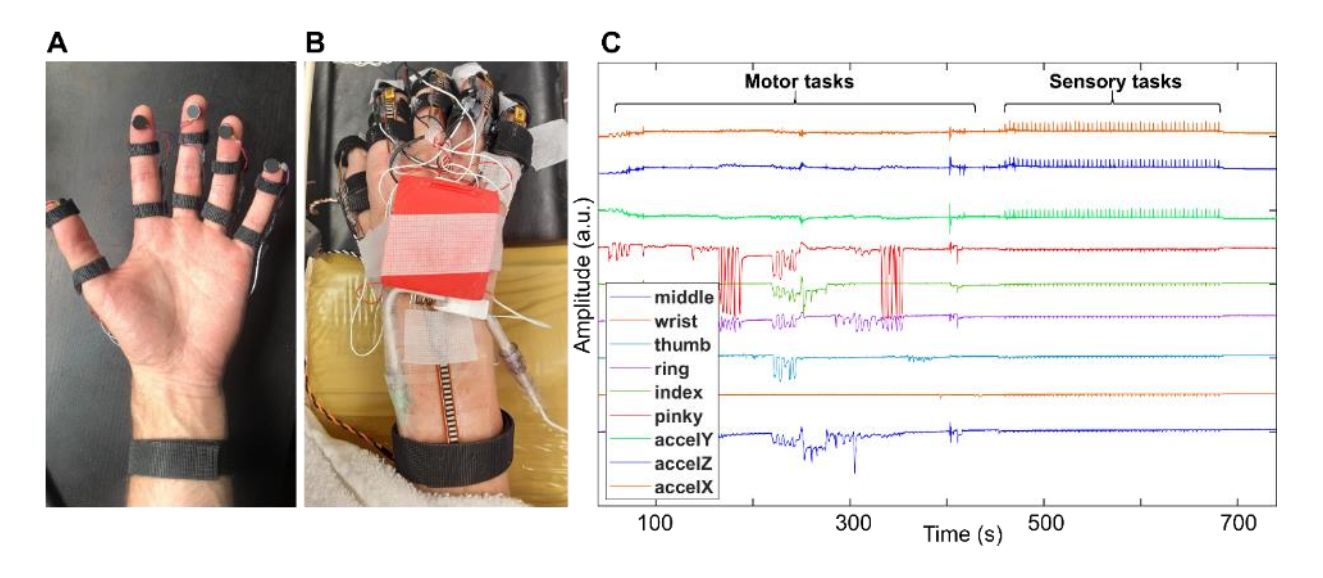


Figure S32. Motor glove that could (A) deliver vibrotactile stimulation on individual fingertips and (B) capture the motion of individual fingers and wrist flexion as well as acceleration of the hand. (C) Motor and sensory task captured with the motor glove system. Vibrotactile stimulus was clearly captured in the accelerometers.

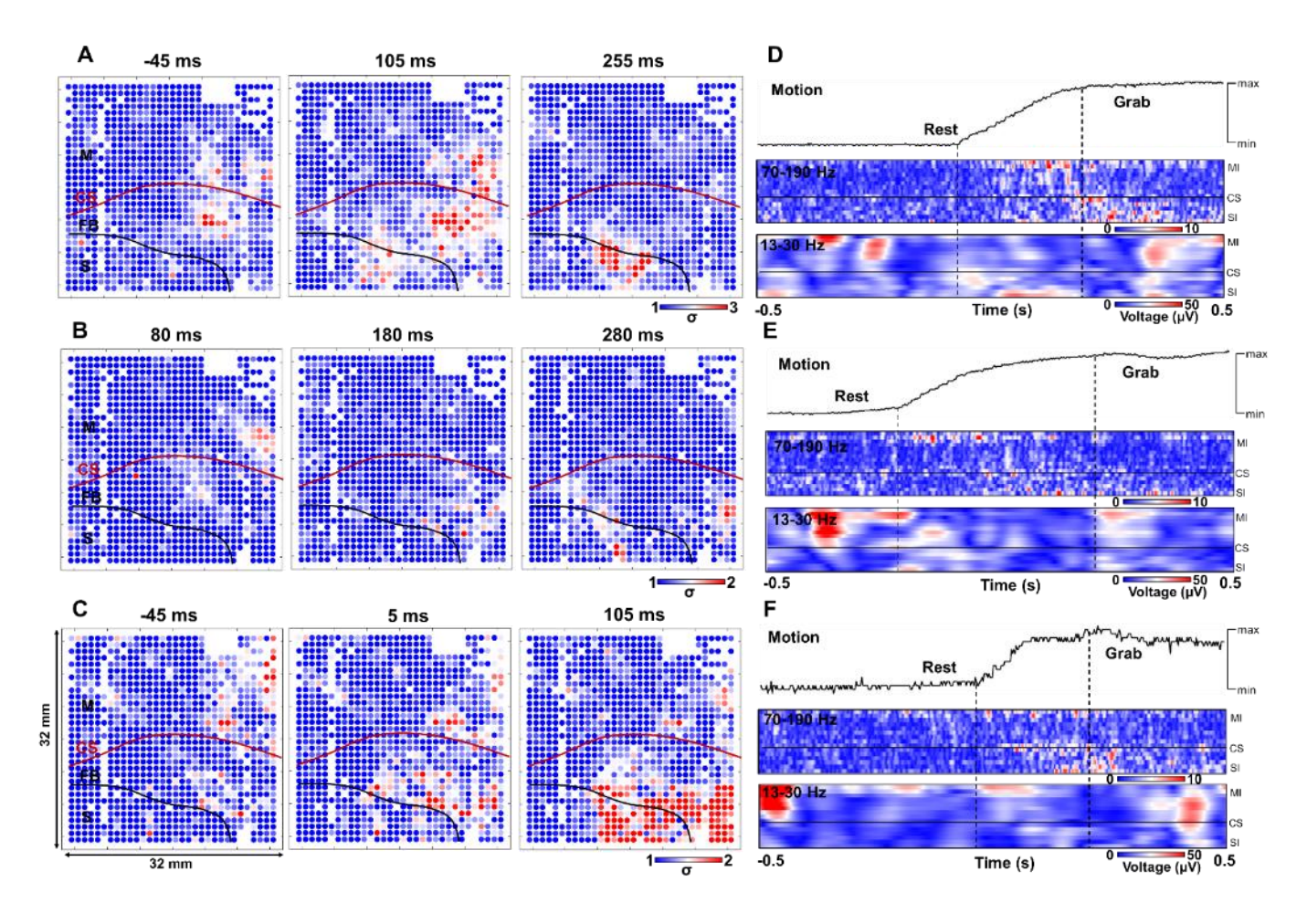


Figure S33. Multiple trials of hand grabbing motion. (A)-(C) Spatial mapping of HGA during the motion. (D)-(F) Captured motion, high gamma and beta amplitudes.

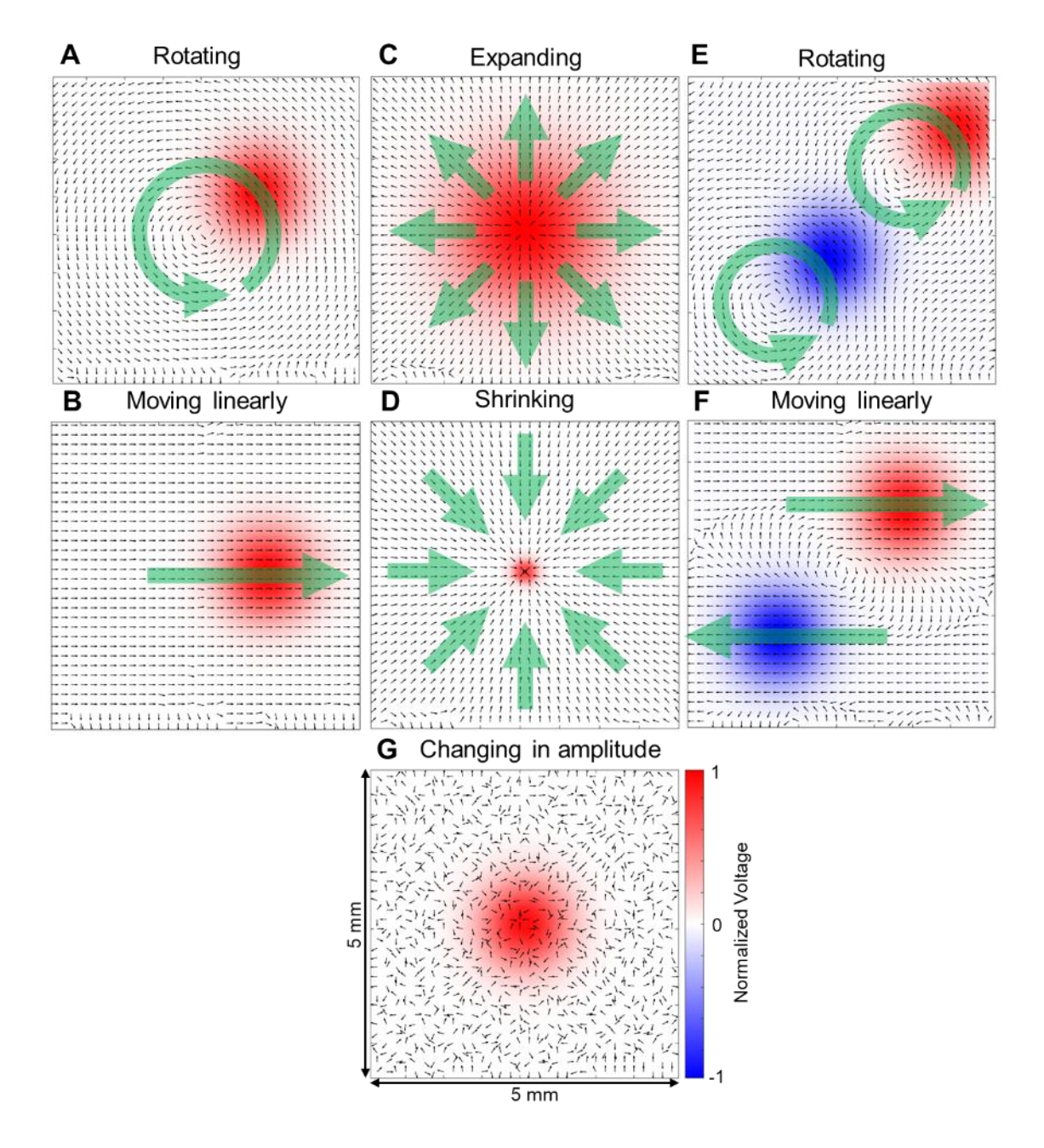


Figure S34. Vector field plots of the propagating beta wave of artificial traveling gaussian wave. Single gaussian wave (A) rotating, (B) linearly moving, (C) expanding, and (D) shrinking. Two gaussian waves (E) rotating and (F) linearly moving. (G) Gaussian wave only changing in amplitude.

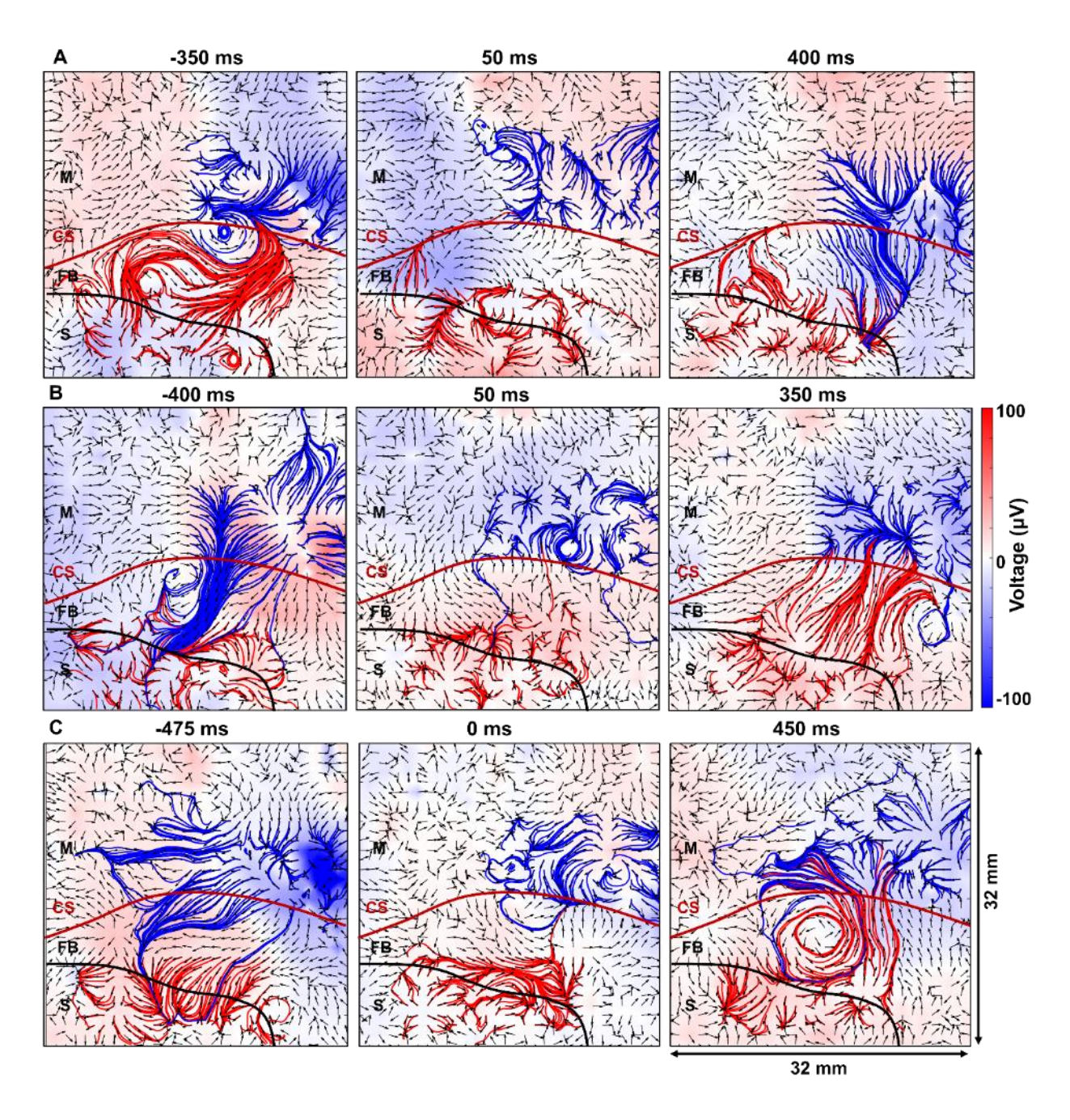


Figure S35. Propagating beta waves for multiple trials of hand grabbing motion before, during, and after grabbing. Different trials shown in (A)-(C) corresponds to the trials in Figs. S33A-C.

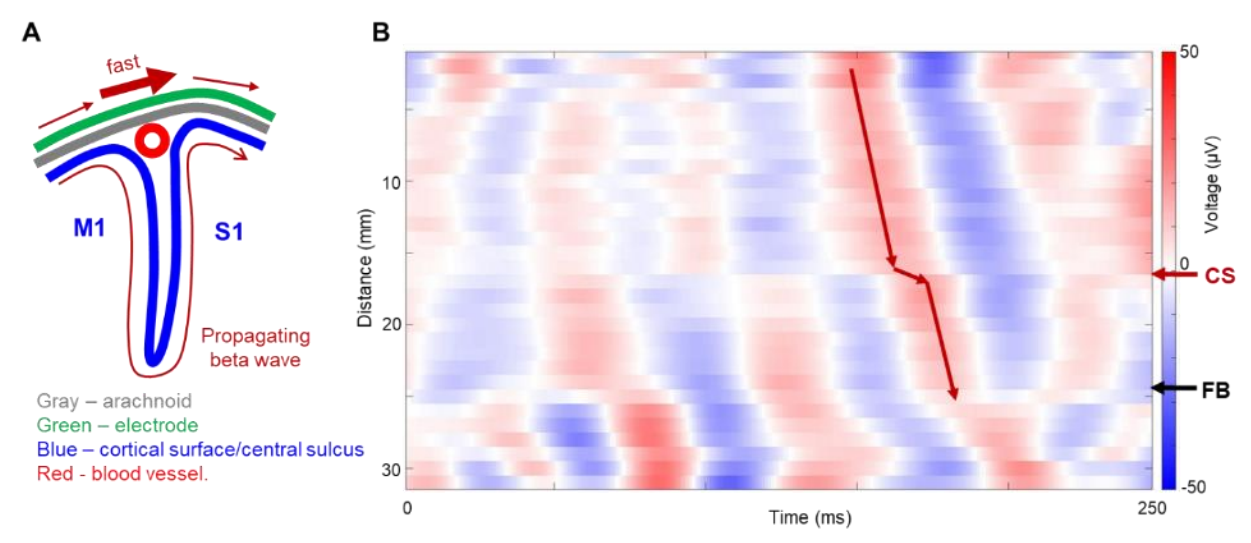


Figure S36. Propagating beta waves measured across the sulcus. (A) Cross-sectional schematics of the measurement configuration. (B) Beta wave potentials along the channels perpendicular to the central sulcus. The beta waves measured from the electrodes across the CS typically showed higher propagating speed, which is an artifact, since the adjacent electrodes placed across the sulcus are actually measuring activity happening on that scale of a few mm to tens of mm distance on an unfolded cortical surface.

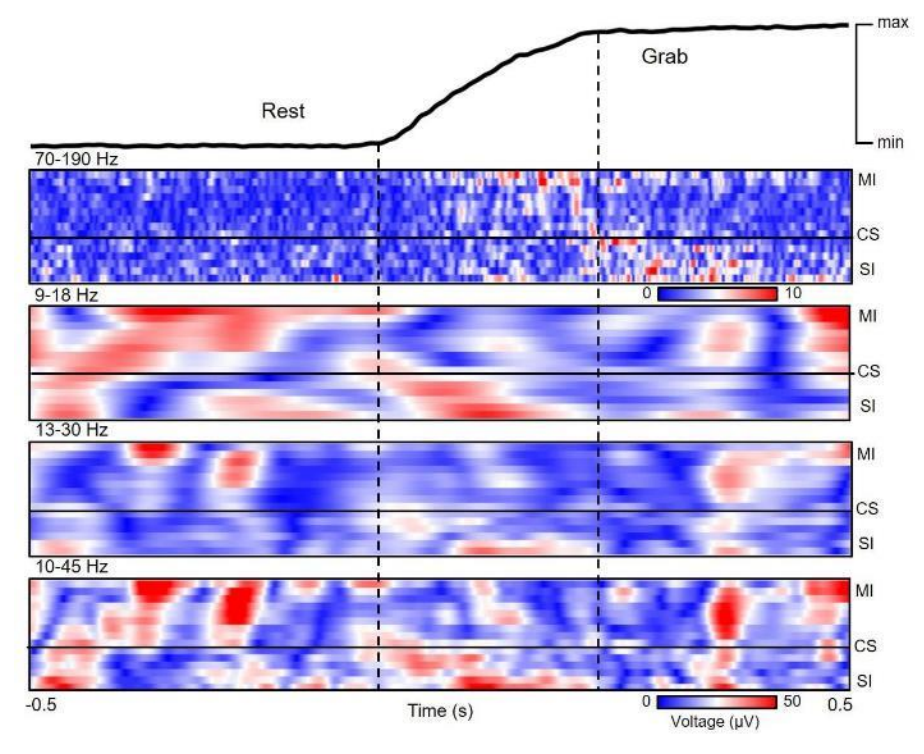


Figure S37. Beta wave amplitudes under different frequency windows of 9-18Hz, 13-30Hz, and 10-45Hz.

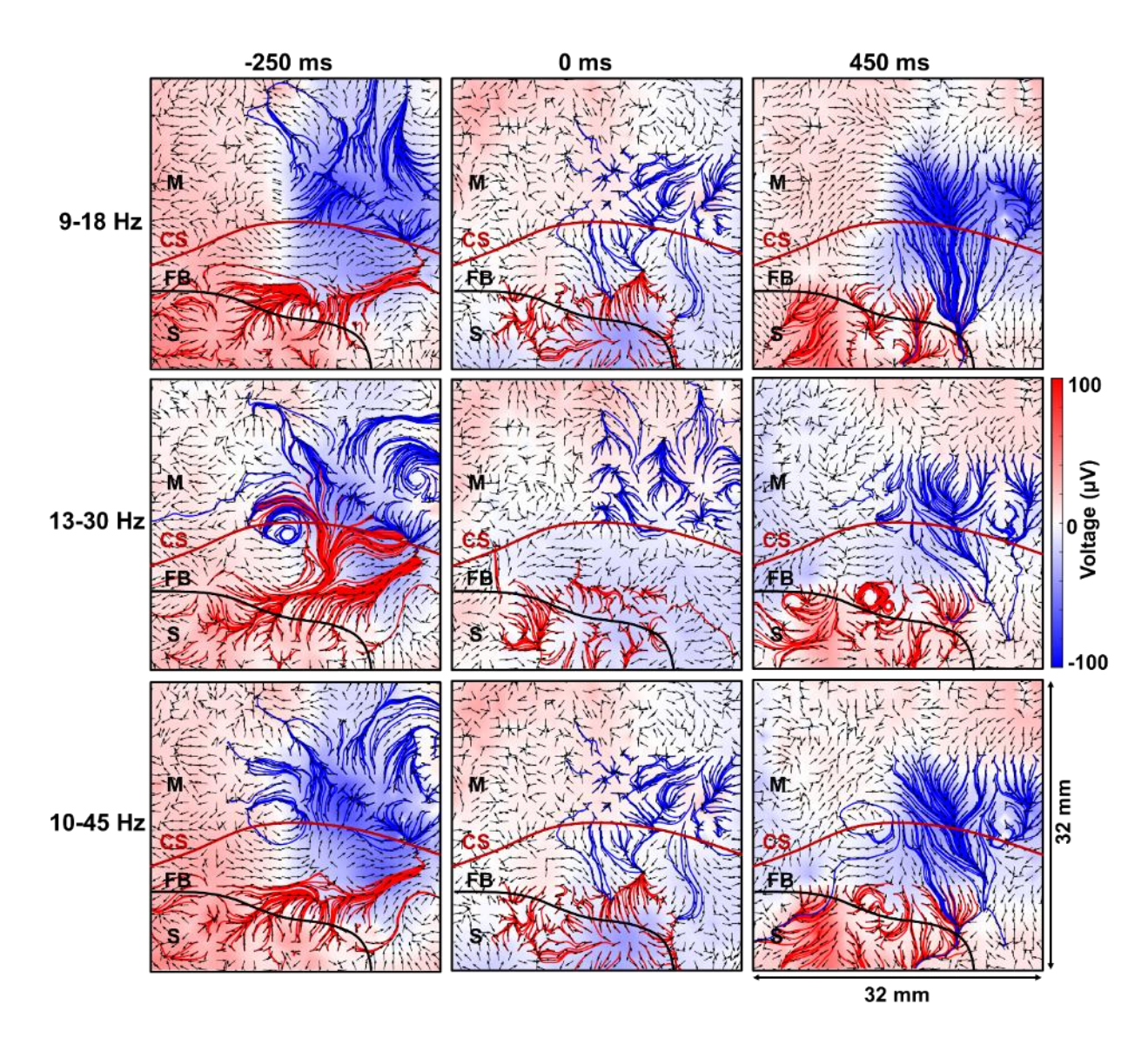


Figure S38. Propagating beta waves for the same trial under different frequency windows of 9-18Hz, 13-30Hz, and 10-45Hz.

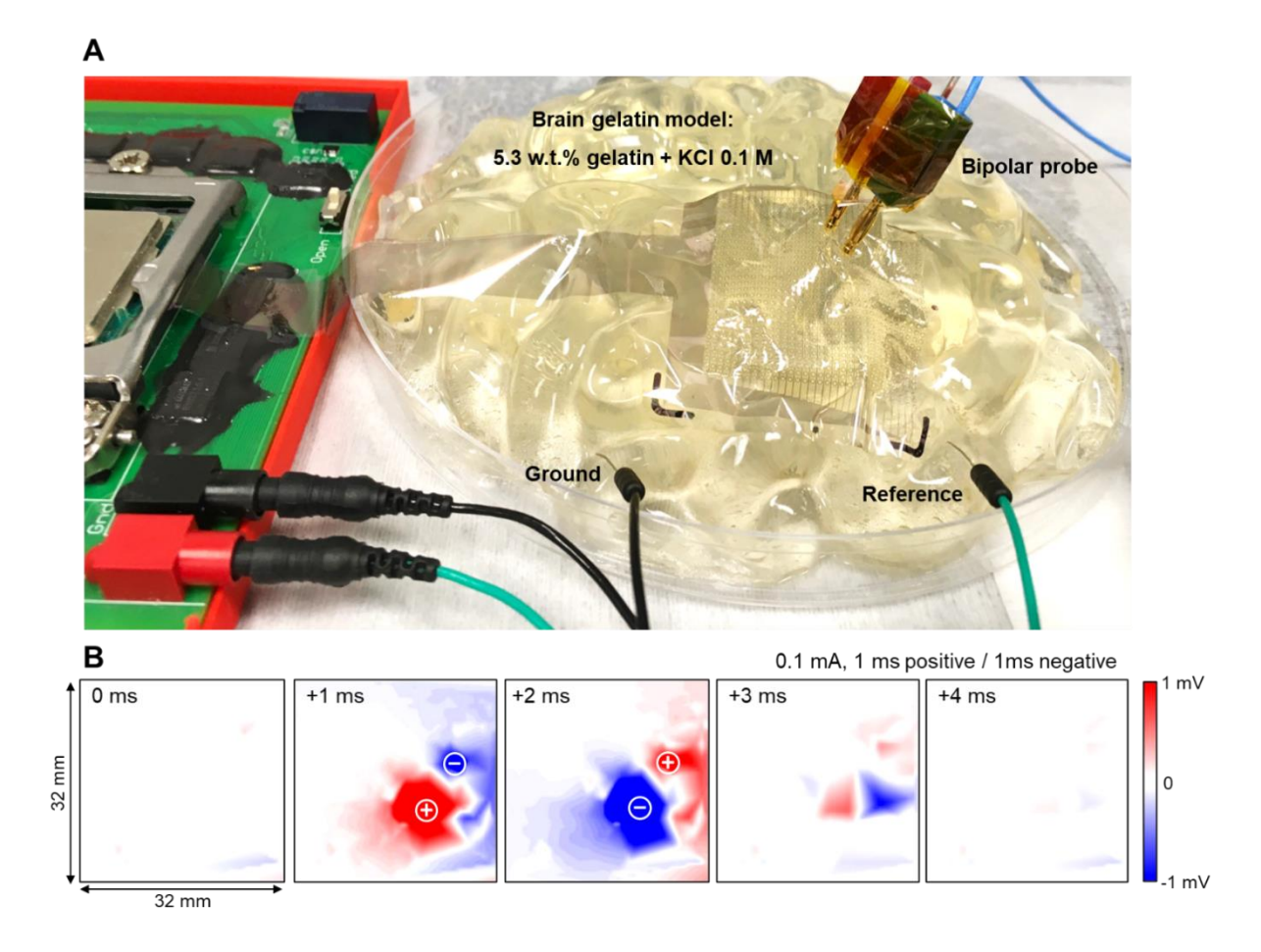


Figure S39. Bench top stimulation test. (A) Bipolar probe is stimulating the gelatin model brain through the perfusion holes on the PtNRGrid. (B) Potential mapping recorded with the PtNRGrid.

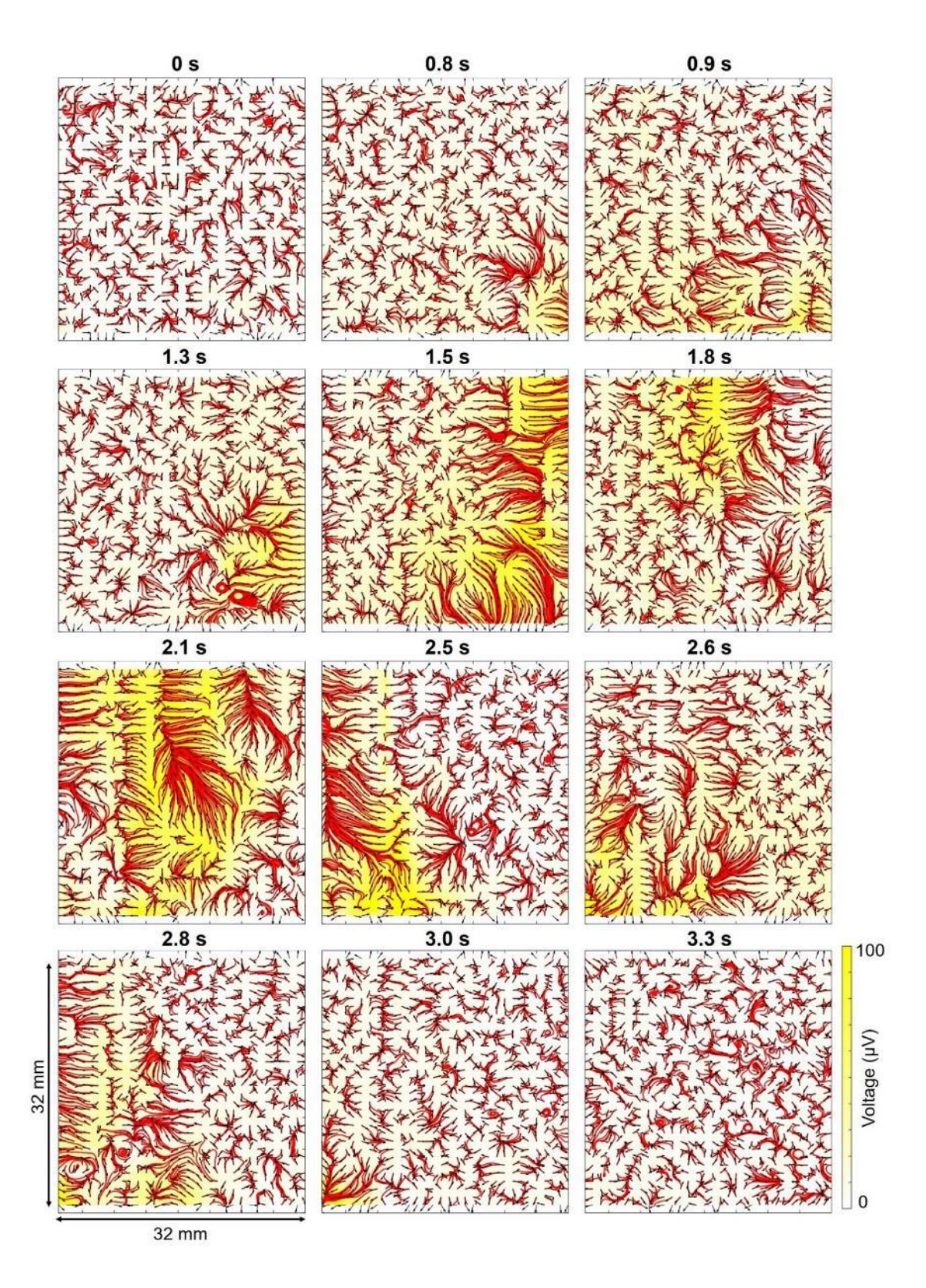
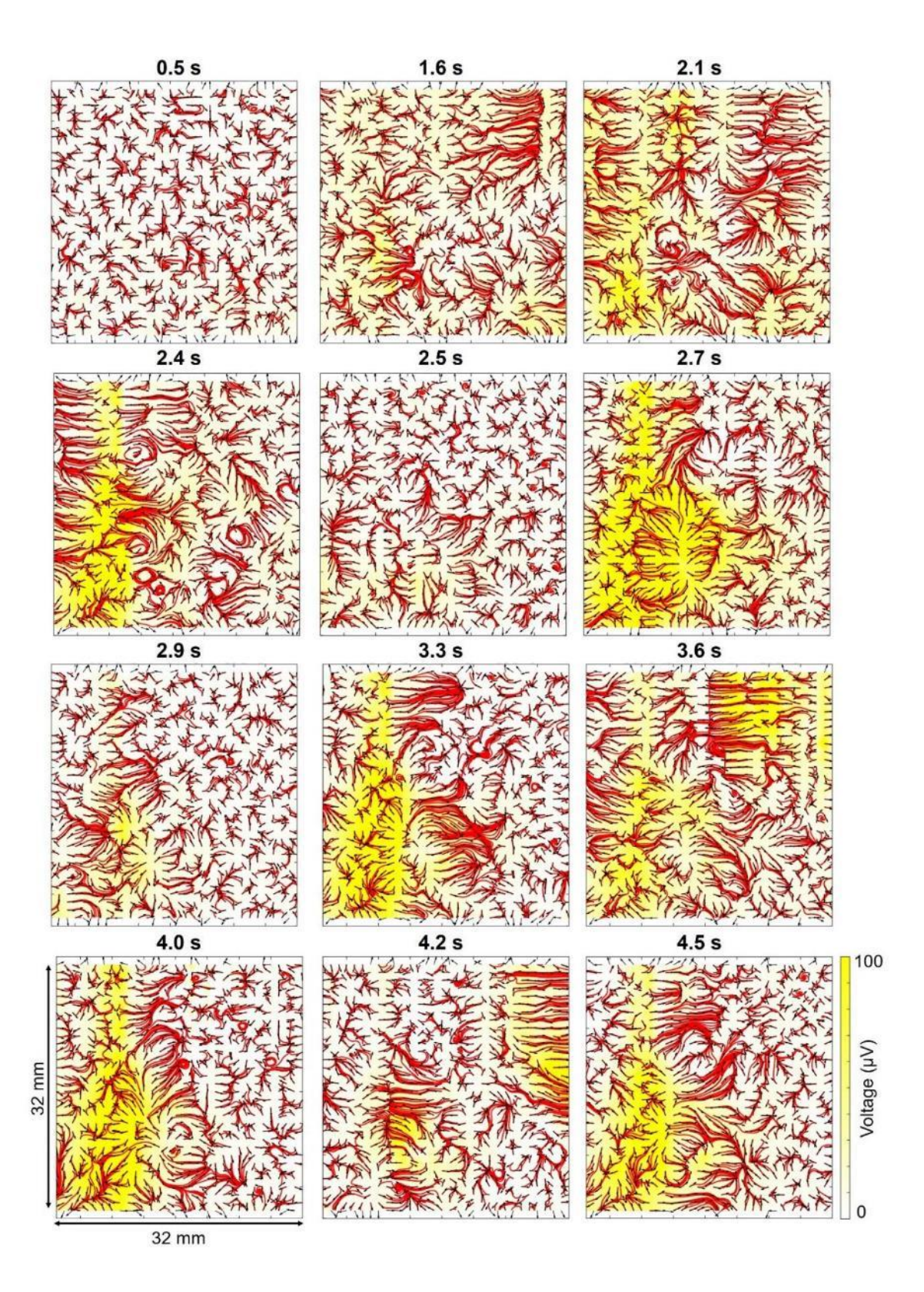


Figure S40. Propagating wave analysis of spontaneous epileptiform activity



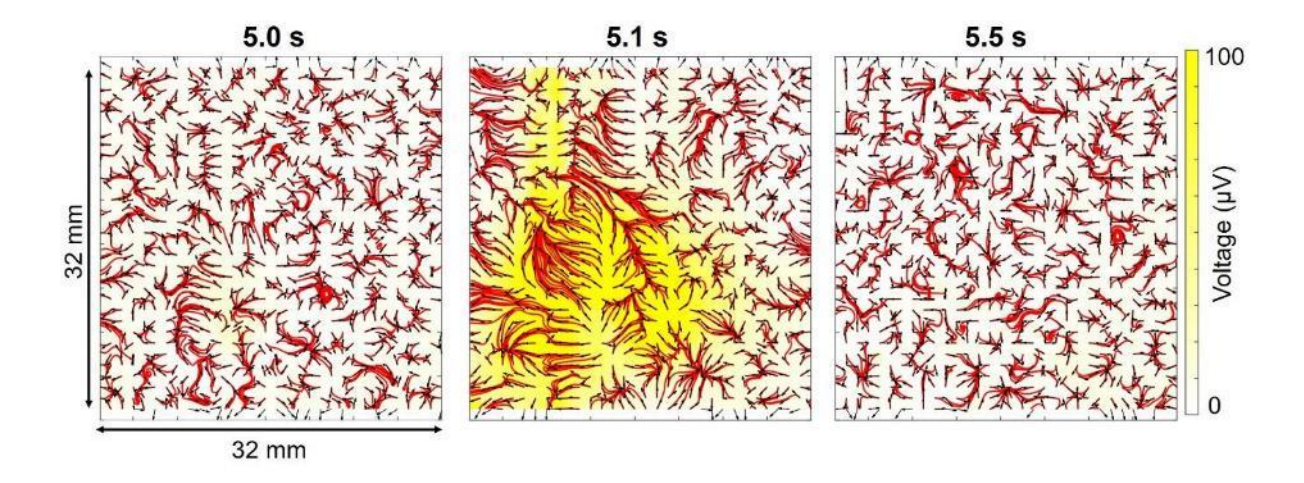


Figure S41. Propagating wave analysis of stim-evoked (4th stimulation) epileptiform activity

Table S1. Table summarizing patient participants with corresponding electrode types (PEDOT, PtNRs), electrode area, sterilization method, case and task details, and the

summary of the recording.

Partici	,	recording.		Sterilization	m 1 - 1	Summary of the	
pant #	Location	Case Info	Electrode	method	Task Info	recording	
1	UCSD - Hillcrest	Implantation setup	PEDOT 32mm×32mm	Heat (pre-vac)	Baseline recording	Validated the recording noise level	
2	OHSU	Awake Craniotomy - Precentral gyrus	PEDOT 3mm×18mm	Heat (pre-vac)	Motor tasks	Hand-motion related LFP were detected	
		Awake Craniotomy - STG	PEDOT 32mm×32mm	Heat (gravity)	Auditory task	Difference between	
3	OHSU	Awake Craniotomy - STG	PEDOT 3mm×18mm	Heat (gravity)	Auditory task	sense/non-sense data were detected	
4	OHSU	Awake Craniotomy, recurring tumor (third resection near motor cortex)	PEDOT 32mm×32mm	Heat (gravity)	Hand motion capture task	Hand-motion related LFP were detected	
5	UCSD - Jacobs Hospital	Anesthetized Craniotomy	PEDOT 32mm×32mm	Heat (gravity)	Phase reversal	Phase reversal in SSEPs (Figure S41)	
6	OHSU	Awake Craniotomy - Right hemisphere motor strip	PEDOT 32mm×32mm	Heat (gravity)	Hand motion capture task	Captured hand- motion related LFP	
			s were made / PEI	OOT electrodes -	> PtNRGrids	1	
7	OHSU	Right craniotomy (epileptic tissue removal)	PtNRs 32mm×32mm	Heat (gravity)	Hand motion and vibrotactile tasks	Electrode impedance increased after the heat sterilization (tap water issue) – Noisy recording	
8	OHSU	Left Craniotomy	PtNRs 32mm×32mm	Heat (gravity)	Hand motion and vibrotactile tasks		
9	OHSU	Awake Craniotomy, M1/S1	PtNRs 32mm×32mm	Heat (gravity)	Hand motion and vibrotactile tasks		
		Sterili	zation method wa	s changed to V-	PRO		
		Awake Craniotomy, Posterior edge of craniotomy, pSTG	PtNRs 32mm×32mm	V-PRO	Phase reversal	CS mapping of facial region	
10	OHSU	Awake Craniotomy, Posterior edge of craniotomy	PtNRs 32mm×50μm (1024-ch dual column linear grid)	V-PRO	Phase reversal	Linear CS boundary (agreed with above result)	
11	OHSU	Awake Craniotomy, recurring tumor, M1/S1	PtNRs 46mm×44mm (2048-ch)	V-PRO	Hand motion and vibrotactile tasks	Brain tissues seriously affected by the large tumor. SSEPs detected (Figure 3)	
12	OHSU	Anesthetized Craniotomy, Temporal Lobe	PtNRs 32mm×32mm	V-PRO	Epileptogenic activity monitoring, Cortex stimulation	Spontaneous and Stim-evoked epileptic discharge observed (Figure 5)	
13	OHSU	Awake Craniotomy, 2 positions on temporal lobe	PtNRs 32mm×32mm	V-PRO	Epileptogenic activity monitoring, Cortex stimulation	Spontaneous epileptic discharge observed	
14	OHSU	Awake Craniotomy	PtNRs 32mm×32mm	V-PRO	-	Interrupted the research due to bleeding	
15	OHSU	Awake Craniotomy, hand knob, M1/S1	PtNRs 32mm×32mm	V-PRO	Phase reversal, Hand motion and vibrotactile tasks	CS mapping (Figure 3), Motor/sensory mapping (Figure 4)	
16	OHSU	Awake Craniotomy, facial region, M1/S1	PtNRs 32mm×32mm	V-PRO	Phase reversal, Facial motor task	SSEPs not detected from	

		Awake Craniotomy, pSTG	PtNRs 32mm×32mm	V-PRO	Auditory task	neuromonitoring (elder patient) / Very low amplitude SSEP recorded from PtNRGrid	
17	OHSU	Awake Craniotomy, Left prefrontal lobe	PtNRs 32mm×32mm	V-PRO	Phase reversal, Hand motion and vibrotactile tasks	Clear SSEP & CS mapping. Implantation location was a little off from the fingers	
18	OHSU	Awake Craniotomy, Left temporal lobe	PtNRs 3mm×18mm	V-PRO	Auditory task	Clear auditory HGA response	
19	OHSU	Awake Craniotomy, Left prefrontal lobe	PtNRs 32mm×32mm	V-PRO	Phase reversal, Hand motion and vibrotactile tasks	Clear SSEP & CS mapping. Implantation	
20	OHSU	Awake Craniotomy, M1/S1	PtNRs 32mm×32mm	V-PRO	Phase reversal, Hand motion and vibrotactile tasks	location was a little off from the fingers	

Table S2. Comparison of PtNRGrid with other recent ECoG grid technologies published recently while this manuscript was under review.

		T. Kaiju <i>et al.</i> , J. Neural Eng. 18 (2021) 036025 <i>(63)</i>	CH. Chiang <i>et al.</i> , J. Neural Eng. 18 (2021) 045009 <i>(64)</i>	This work: PtNRGrid Y. Tchoe <i>et al</i> .
Number of recording channels	Human brain	-	244	1024, 2048
	Non-human primate brain	1152 (128 × 9 electrodes)	244	-
	Rodent brain	-	61	1024
Benchtop device demonstration of 1024 array (recordings presented were for 244-ch in NHP and 61-ch in rodents)		-	1024 (256 × 4 electrodes)	-
Electrode thickness for conformity to brain curvature		20 ~ 60 μm	60 μm	6.6 µm
Max recording density		1,149 cm ⁻²	596 cm ⁻²	4,444 cm ⁻²
Flexible material		Parylene C	Liquid crystal polymer	Parylene C
Electrochemical interface material		Pt black	PtIr	PtNR
Material deposition method		Electroplating	Electroplating	Sputtering & de-alloying
1kHz impedance magnitude		$26 \pm 7 \mathrm{k}\Omega$ (50 x 50 $\mu\mathrm{m}^2$)	$4.6 \pm 1.8 \text{ k}\Omega$ (200 µm diameter)	$10 \pm 2 \text{ k}\Omega$ (30 μm diameter)

- PtNRGrid achieved the first multithousand channel human brain recording. The human brain recordings demonstrated in C.-H. Chiang *et al.* was done with 244 channel electrodes. T. Kaiju *et al.*'s work was performed on non-human primates.
- The 1152 channel electrode demonstrated in T. Kaiju *et al.* is made by gluing nine 128 channel electrodes together in one place.
- C.-H. Chiang et al. showed a benchtop device demonstration of a 1024 channel electrode array by gluing four 256 channel electrodes without presenting recording data.

- The electrodes stacked on top of each other (T. Kaiju *et al.*) may not be accepted for human use because the gaps between the layers may be hard to properly sterilize.
- Electrode thickness of T. Kaiju *et al.* and C.-H. Chiang *et al.* were 20~60 μm and 60 μm, respectively, whereas PtNRGrid was only 6.6 μm in total thickness. The thickness of the electrode is a key factor in achieving high conformality to the brain curvatures, improved recording quality and sharp delineation of cortical boundaries for neural correlates.
- Recording density of PtNRGrids was as high as 4,444 cm⁻² which is substantially higher than the other two technologies: T. Kaiju *et al.* 1,149 cm⁻², C.-H. Chiang *et al.* 596 cm⁻²
- PtIr or Pt black are usually electroplated serially on top of planar contacts, one channel at a time. On the other hand, our PtNR are manufactured via a scalable process that uses cosputtering and de-alloying to make thousands of PtNR contacts at once. The difference in this part of the fabrication process makes a substantial difference in the manufacturing time as well as the uniformity in the contact quality. Electroplating of hundreds of channels can take as much as a few hours using a manual process, whereas the typical PtNR process on 7-inch glass forms 4096 contacts at once by a few minutes of co-sputtering followed by de-alloying. Since all PtNR contacts are formed at the same time, the quality of the PtNRs is extremely uniform across thousands of channels. Additionally, the 1 kHz impedance magnitude of the PtNRs was superior to the Pt black; 30 µm diameter PtNRs had even lower 1 kHz impedance magnitude than the larger Pt black contact.

- **Movie S1.** Video of the spatial mapping of HGA during the hand grabbing motion. Slowed 11 times the actual speed.
- **Movie S2.** Video of the propagating beta wave prior to hand grabbing motion. Arrows indicate the vector fields of the propagating direction and the background color represents the beta wave potentials. Slowed 110 times the actual speed.
- **Movie S3.** Video of the propagating beta wave after completing the hand grabbing motion. Arrows indicate the vector fields of the propagating direction and the background color represents the beta wave potentials. Slowed 110 times the actual speed.
- **Movie S4.** Propagating beta and high gamma activities overlayed on the brain model. The vector field and streamlines on the PtNRGrid represent the propagating beta waves, and green scattered dots represent the high gamma activity. Slowed 51 times the actual speed.
- **Movie S5.** Videos of spontaneous epileptiform activity from epileptogenic tissue. Scatter map shows the 10-59 Hz brain wave amplitude. Slowed 4 times the actual speed.
- **Movie S6.** Spontaneous epileptiform discharges overlayed on the patient's brain model. Scattered dots and contours on the PtNRGrid represent the 10-59 Hz brain wave amplitude. Slowed 17 times the actual speed._
- **Movie S7.** Videos of stimulation-evoked (4th stim) epileptiform activities from epileptogenic tissue. Scatter map shows the 10-59 Hz brain wave amplitude. Slowed 4 times the actual speed.
- **Movie S8.** Stimulation-evoked epileptiform discharges overlaid on the patient's brain model. Scattered dots and contours on the PtNRGrid represent the 10-59 Hz brain wave amplitude. Slowed 20 times the actual speed.